Channel Modeling and Machine Learning for Nonlinear Fiber Optics

Citation for published version (APA):
Oliari Couto Dias, V. (2022). *Channel Modeling and Machine Learning for Nonlinear Fiber Optics*. [Phd Thesis 1 (Research TU/e / Graduation TU/e), Electrical Engineering]. Technische Universiteit Eindhoven.

Document status and date:
Published: 19/01/2022

Document Version:
Publisher's PDF, also known as Version of Record (includes final page, issue and volume numbers)

Please check the document version of this publication:

- A submitted manuscript is the version of the article upon submission and before peer-review. There can be important differences between the submitted version and the official published version of record. People interested in the research are advised to contact the author for the final version of the publication, or visit the DOI to the publisher's website.
- The final author version and the galley proof are versions of the publication after peer review.
- The final published version features the final layout of the paper including the volume, issue and page numbers.

Link to publication

General rights
Copyright and moral rights for the publications made accessible in the public portal are retained by the authors and/or other copyright owners and it is a condition of accessing publications that users recognise and abide by the legal requirements associated with these rights.

- Users may download and print one copy of any publication from the public portal for the purpose of private study or research.
- You may not further distribute the material or use it for any profit-making activity or commercial gain
- You may freely distribute the URL identifying the publication in the public portal.

If the publication is distributed under the terms of Article 25fa of the Dutch Copyright Act, indicated by the "Taverne" license above, please follow below link for the End User Agreement:

www.tue.nl/taverne

Take down policy
If you believe that this document breaches copyright please contact us at:

openaccess@tue.nl

providing details and we will investigate your claim.

Download date: 04. Oct. 2023

Channel Modeling and Machine Learning for Nonlinear Fiber Optics

Vinícius Oliari Couto Dias

A catalogue record is available from the TU/e Library.
ISBN: 978-90-386-5426-3
NUR: 959

Cover design by Vinícius Oliari
Printed by Ipskamp Printing

The research presented in this dissertation was conducted in the Information and Communication Theory Lab (ICT Lab) of the Signal Processing Systems (SPS) group at the Department of Electrical Engineering, Eindhoven University of Technology (TU/e).

This work was supported by the Netherlands Organisation for Scientific Research (NWO) via the VIDI Grant ICONIC (project number 15685).

Channel Modeling and Machine Learning for Nonlinear Fiber Optics

THESIS

ter verkrijging van de graad van doctor aan de Technische
Universiteit Eindhoven, op gezag van de rector magnificus
prof.dr.ir. F.P.T. Baaijens, voor een commissie aangewezen door
het College voor Promoties, in het openbaar te verdedigen op
vrijdag 19 Januari 2022 om 16:00 uur

door

Vinícius Oliari Couto Dias

geboren te Vila Velha, Brazilië

Dit proefschrift is goedgekeurd door de promotoren en de samenstelling van de promotiecommissie is als volgt:

voorzitter:	prof.dr.ir. Peter G.M. Baltus
1e promotor:	dr. Alex Alvarado
2e promotor:	prof.dr. Erik Agrell (Chalmers University of Technology)
Copromotor:	dr. Gabriele Liga
Promotiecommissieleden:	dr. Marco Secondini (Scuola Superiore Sant'Anna)
	prof.dr.ir. Frans M.F. Willems
	prof.dr. Robert Killey (University College of London)
Adviseur:	dr. Domaniç Lavery (Infinera)

Het onderzoek of ontwerp dat in dit proefschrift wordt beschreven is uitgevoerd in overeenstemming met de TU/e Gedragscode Wetenschapsbeoefening.

Summary

Signal propagation in an optical fiber suffers from fiber effects that distort the transmitted signal. These effects are modeled by the nonlinear Schrödinger equation (NLSE) [1, Ch. 2]. One of the simplest variants of the NLSE accounts for three main physical effects: attenuation, group velocity dispersion (GVD), and Kerr nonlinearities [1, Ch. 2]. Attenuation and GVD can be efficiently compensated with amplifiers and linear filters [2], respectively. Digital compensation techniques that also account for nonlinearities also exist, however, they suffer from high computational complexity [3]. A possible method for alleviating this complexity is to design receivers based on simplified analytical representations of the NLSE solution [4]. Some receivers [5] have been developed based on regular perturbation (RP) on the Kerr coefficient [6, 7], which is an approximated solution of the NLSE. The RP method is a technique used to simplify differential equations by assuming that one term of the equation has lower impact on the final solution than the others. In the RP on the Kerr coefficient, such term is the nonlinear one. Therefore, the approximation given by that model is inaccurate in the highly-nonlinear regime, as shown in [6, 7].

To reduce the complexity and optimize elements of an optical system, machine learning (ML) can be used. ML-optimized receivers, such as learned digital backpropagation (LDBP) [8], have proven in simulations to achieve close or higher performance than its standard counterpart, digital backpropagation (DBP) [8, 9]. LDBP performance in deployed fibers or experiments is still being investigated in the literature [10, 11]. ML can also be used to improve the design of certain transceiver subsystems. Examples of this are the optimization of geometrical shaping (GS) [12, 13] and probabilistic shaping (PS) [14]. The ideal designs of GS and PS when the signal is propagated in the NLSE are still unknown in the literature.

In this thesis, we address two problems: (i) finding an analytical approximated solution of the NLSE in the highly-nonlinear regime; and (ii) investigating the performance of ML-optimized optical systems. The main contributions are four:

1. we use the NLSE as a starting point to obtain a new approximate closed-form analytical

solution based on RP. The resulting model is called RP on the GVD parameter and has high accuracy in the low-dispersive highly-nonlinear regime [15, 16].

2. we improve the accuracy of the RP on the GVD parameter model by introducing a new analytical model that is a perturbation on the same parameter. In this new approach, we replace RP by a method called frequency logarithm perturbation [17, 18].
3. we investigate the experimental performance of an ML receiver for optical communications based on the DBP method. The resulting LDBP is shown to achieve the same performance as DBP but with significantly less complexity [19].
4. we use ML to optimize an end-to-end optical system and find a high-performance PS and GS designs. In addition, the optimization is performed in a multi-channel transmission for each channel individually [20, 21]. We were able to optimize for the first time a 10 bits/4D symbol constellation.

List of Publications

Journal Articles

1. ***Paper B:*** **V. Oliari**, E. Agrell, and A. Alvarado, “Regular perturbation on the group-velocity dispersion parameter for nonlinear fibre-optical communications,” *Nature Communications*, vol. 11, no. 933, pp. 1–11, Feb. 2020.
2. ***Paper D:*** **V. Oliari**, E. Agrell, G. Liga, and A. Alvarado, “Frequency logarithmic perturbation on the group-velocity dispersion parameter with applications to passive optical networks,” *J. Lightwave Technol.*, vol. 39, no. 16, pp. 5287–5299, Aug. 2021, Invited Paper, Highly Scored.
3. ***Paper E:*** **V. Oliari**, S. Goossens, C. Häger, G. Liga, R. M. Bütler, M. van den Hout, S. van der Heide, H. D. Pfister, C. Okonkwo, and A. Alvarado, “Revisiting efficient multi-step nonlinearity compensation with machine learning: an experimental demonstration,” *J. Lightwave Technol.*, vol. 38, no. 12, pp. 3114–3124, May 2020.
4. ***Paper F:*** **V. Oliari**, B. Karanov, S. Goossens, G. Liga, O. Vassilieva, I. Kim, P. Palacharla, C. Okonkwo, A. Alvarado, “High-cardinality hybrid shaping for 4D modulation formats in optical communications optimized via end-to-end learning,” in *arXiv:2112.10471*, 2021.

Conference Articles

1. ***Paper A:*** **V. Oliari**, E. Agrell, and A. Alvarado, “Regular perturbation for the weak-dispersion regime,” in *21st International Conference on Transparent Optical Networks (ICTON)*, Angers, France, July 2019.
2. ***Paper C:*** **V. Oliari**, E. Agrell, and A. Alvarado, “Logarithmic perturbation models in the weak-dispersion regime with applications to passive optical networks,” in *Proc. European Conf. Optical Communication (ECOC)*, Brussels, Belgium, Dec. 2020.

Not Included in this Thesis

1. B. Karanov, **V. Oliari**, M. Chagnon, G. Liga, A. Alvarado, V. Aref, D. Lavery, P. Bayvel, and L. Schmalen, “End-to-end learning in optical fiber communications: Experimental demonstration and future trends,” in *Proc. European Conf. Optical Communications (ECOC)*, 2020.
2. H. Rabbani, G. Liga, **V. Oliari**, L. Beygi, E. Agrell, M. Karlsson, A. Alvarado, “An improved model of nonlinear fiber propagation in the presence of Kerr nonlinearity and stimulated Raman scattering,” in *arXiv:1909.08714v3*, 2019.

Table of Contents

List of Abbreviations

Symbol	**Description**
AIR	Achievable Information Rate
AM	Analytical Model
AOM	Acoustic-Optic Modulator
AWGN	Additive White Gaussian Noise
BER	Bit-Error Rate
BSC	Binary Symmetric Channels
CD	Chromatic Dispersion
CDC	Chromatic Dispersion Compensation
CMA	Constant Modulus Algorithm
DAC	Digital-to-Analog Converter
DBP	Digital Backpropagation
DP-IQM	Dual-Polarization IQ-Modulator
DSP	Digital Signal Processing
ECD	Electronic Chromatic Dispersion
ECL	External Cavity Laser
EDFA	Erbium-Doped Fiber Amplifier
ERP	Enhanced Regular Perturbation
FD	Frequency-Domain
FEC	Forward-Error-Correction
FFT	Fast-Fourier Transform
FIR	Finite Impulse Response
FLP	Frequency Logarithmic Perturbation
FRLP	Frequency Resolved Logarithmic Perturbation
GMI	Generalized Mutual Information
GS	Geometric Shaping

GVD	Group-Velocity Dispersion
HB	Histogram-Based
HD	Hard-Decision
LDBP	Learned Digital Backpropagation
LO	Local Oscilator
LP	Logarithmic Perturbation
LSPS	Loop-Synchronised Polarization Scrambler
MAP	Maximum A-Posteriori
MF	Matched Filter
MI	Mutual Information
MIMO	Multiple-Input Multiple-Output
MMA	Multiple Modulus Algorithm
MSE	Mean-Squared Error
NN	Neural Network
NLPN	Nonlinear Phase Noise Model
NLSE	Nonlinear Schrödinger Equation
NSD	Normalized Squared Deviation
NZDSF	Nonzero Dispersion Shifted Fiber
OH	Overhead
OHV	One-Hot Vector
OTF	Optical Tunable Filter
QAM	Quadrature Amplitude Modulation
QPSK	Quadrature Amplitude Shift Keying
PDF	Probability Density Function
PM	Polarization-Multiplexed
PMD	Polarization-Mode Dispersion
PON	Passive Optical Network
PS	Probabilistic Shaping
RP	Regular Perturbation
RQ	Research Question
RRC	Root-Raised Cosine
RS	Reed-Solomon
SGD	Stochastic Gradient Descent
SNR	Signal-to-Noise Ratio
SSFM	Split Step Fourier Method
SSMF	Standard Single-Mode Fiber
StPS	Steps Per Span
TOD	Third-Order Dispersion
WSS	Wavelength Selective Switch

Part I

Overview

CHAPTER 1

Introduction

1.1 Motivation

The way society has used the internet over the past three decades has significantly changed. From sending text or image messages, the internet is now used to stream high-resolution videos and even to perform remote real-time surgeries [22]. This change results in an increase of end-user data rates from the order of kilobits per second (kbps) to the order of gigabits per second (Gbps). This increase was only possible with the advent of optical fibers.

Optical fibers are the backbone of global communication, carrying approximately 99% of today's internet traffic. The large available bandwidth and low power loss allow optical fibers to transmit terabits of information per second over thousands of kilometers. Many of these cables are located in the bottom of oceans and connect all continents. Currently, there are over 400 subsea cables in operation [23]. Although each of these cables transmit an immense amount of data, the current growth of internet traffic might reach the rate limits of optical fiber transmission, an effect known as the "capacity crunch" [24].

One of the main factors that limit optical fiber transmission are the fiber effects that emerge during the signal propagation. These effects can be represented by the nonlinear Schrödinger equation (NLSE) [1, Ch. 2] (see Sec. 3.2). The NLSE determines how the input signal evolves during fiber propagation. There are three main physical effects that are usually used to model transmission: attenuation, CD, and Kerr nonlinearities [1, Ch. 2]. The attenuation is a linear effect that reduces the signal power after transmission over a certain distance. This effect can be undone by the use of optical amplifiers within the transmission link. CD is also a linear effect and is modeled as an all-pass filter [1, Ch. 3]. This effect can also be corrected by using an all-pass filter with the opposite transfer function and even efficiently compensated by FIR filters [2]. However, in the presence of nonlinearities, CD mixes with nonlinearities giving rise to a distortion that is nonlinear on the transmitted signal and whose correction can be challenging. This effect is one of the major limitations in the fiber transmission rates [25]. To overcome the limits on fiber transmission, a deeper understanding on how fiber effects affect the propagated signal is needed.

1.1.1 Modeling Nonlinear Effects

The NLSE is capable of representing the previously described fiber effects via a differential equation. Although the representation via a differential equation might be sufficient for building numerical simulation methods, an analytical model is preferred for modeling distortions in the propagated signal. With an analytical expression, one could estimate the system performance via closed formulas (as done in [26]) or design low-complexity receivers (as done in [5]). The NLSE has no explicit analytical solution for an arbitrary transmitted signal, therefore approximations are needed to solve the equation.

The most employed approach to extract analytical models from the NLSE is perturbation theory. Perturbation theory consists in assuming that the contribution of one of the terms in an equation can be considered small enough to be neglected in a first instance. This term is subsequently added to the final solution by solving a simpler equation than the original one. There are many types of perturbation techniques that can be applied in an equation, with the most common in the optical community being the regular perturbation (RP) [6] and the logarithmic perturbation (LP) [7] methods. In the NLSE context, the effect that is usually considered small is the Kerr nonlinearities. By applying a perturbation on the nonlinear Kerr coefficient, one obtains the RP on the Kerr nonlinear coefficient model [6], which is accurate in operation regimes that are typical for most optical communication systems [27]. This model usually considers a first-order perturbation approach [7]. Increasing the order of the perturbation results in a more accurate model at the cost of increased analytical complexity.

By considering a small Kerr effect, RP on the Kerr nonlinear coefficient will present limitations in the signal modeling for the highly nonlinear regime, i.e. where transmit powers are sufficiently high to make the Kerr effect the dominant one in pulse propagation. This regime is of great interest when trying to increase the capacity of fiber transmission. To obtain models that are accurate in the presence of high nonlinear effects, a new approach is needed when obtaining approximated solutions for the NLSE.

1.1.2 Mitigating Nonlinear Effects

Efficiently correcting or mitigating the nonlinear effects is still an active area of research. Some techniques, such as DBP [28], can undo most of the fiber impairments. The principle behind DBP is to divide the fiber into small segments and revert the fiber propagation by digitally undoing each effect separately on those segments. DBP demands high computational complexity, which is prohibitive in most practical communication systems.

Many alternatives have been proposed in the literature to reduce DBP complexity. Some of those approaches are: using fewer steps per span and an enhanced DBP algorithm [29]; using perturbation models [5]; and using ML to optimize short FIR filters that replace the linear operations of DBP [8]. The latter approach is referred to as LDBP. LDBP is a promising technique since it has potential to correct effects that are even not modeled by the NLSE, such as transceiver impairments or more complex fiber effects. Some works have already proven its efficiency with experimental results [10, 30].

1.1.3 Embracing Nonlinear Effects

Instead of trying to mitigate the nonlinear effects at the receiver, another approach to increase information rates is to adapt the transmitted signal to the nonlinear channel. One way to achieve this adaptation is by changing the geometry of the transmitted constellation and/or changing the a priori probabilities of each constellation point.

By changing the constellation geometry, it is possible to generate signals that are more nonlinearly tolerant, such as constant modulus constellations [31, 32]. Changing the a priori probabilities has also shown to be efficient to increase transmission rates in the optical channel, even when these probabilities are optimized for the linear regime [33]. Testing all the possible constellation geometries and probabilities is unfeasible due to computational complexity. Therefore, only a finite set of the possible constellations and probabilities are considered for a numerical optimization. One optimization approach is to use ML and approximate the nonlinear channel by fiber models [13, 34].

1.2 Thesis Scope and Organization

This thesis is divided into two parts. Part I is an introduction where the theory behind the topics treated in this thesis is presented. This first part is composed by Chapters 3 and 4, which address analytical models for fiber propagation and machine learning theory, respectively. Part II contains 6 papers. Papers A, B, C, and D are related to analytical models for the weak dispersion highly-nonlinear regime. To the best of our knowledge, this was the first time these models were proposed in the literature, resulting in one of the main contributions of this thesis. Papers E and F are about machine learning techniques applied to optical fiber communications. In these 6 papers, we try to answer the following research questions (RQs) related to optical channel modeling, nonlinearity compensation, and GS/PS for the nonlinear channel.

RQ-1 How to obtain an analytical fiber model that is accurate in the very high nonlinear regime without increasing the perturbation order of RP on the Kerr coefficient?

Paper A: “Regular perturbation for the weak-dispersion regime” - ICTON 2019
Paper B: “Regular perturbation on the group-velocity dispersion parameter for nonlinear fibre-optical communications” - Nature Communications

We develop a new model for the highly-nonlinear regime by applying RP on the group-velocity dispersion (GVD) parameter instead of on the Kerr coefficient. By following this approach, the nonlinear Kerr effect is no longer considered a minor effect and signals at very high input power can be accurately modeled. However, this new model considers the chromatic dispersion (CD) a minor effect and can only be accurate when the accumulated dispersion is low. The accuracy of the model is compared with RP on the Kerr coefficient when varying system parameters such as fiber length, GVD parameter, Kerr coefficient, input power, and modulation format.

RQ-2 How to improve the accuracy of RP on the GVD parameter to tolerate more accumulated dispersion and higher input powers?

Paper C: “Logarithmic perturbation models in the weak-dispersion regime with applications to passive optical networks” - ECOC 2020
Paper D: “Frequency logarithmic perturbation on the group-velocity dispersion parameter with applications to passive optical networks” - Journal of Lightwave

Technology

The LP method can be used to try to achieve a model with higher accuracy than the models obtained via RP. This is the case for the RP on the Kerr coefficient: by applying LP on the Kerr coefficient, one obtains a more accurate model than the RP one. The same approach, however, is not as efficient for the GVD parameter. Therefore, we propose a frequency LP (FLP) approach for the GVD parameter which yields a model with significantly higher accuracy than RP on the GVD parameter. The regime where FLP on the GVD parameter is accurate is similar to the one of passive optical networks (PONs). The accuracy of the proposed model is evaluated in continuous time in [17, 18]. In [18], an additional evaluation is made in discrete time, where the model is used to obtain decision regions for the highly-nonlinear regime.

RQ-3 How does LDBP perform in experiments?

Paper E: "Revisiting efficient multi-step nonlinearity compensation with machine learning: an experimental demonstration" - Journal of Lightwave Technology

In [19] we test the performance of LDBP in a transmission experiment where a single channel is launched into a multi-span optical link. Experimental impairments such as transceiver noise, phase-noise, and IQ imbalance are present in the transmission. Due to these and other impairments, the performance of both DBP and LDBP saturates quickly after using a few number of steps per span and both methods present similar performance. Nevertheless, the performance of DBP and LDBP is higher than linear receivers with only CDC, for example. This improved performance shows that DBP and LDBP are able to compensate for nonlinear effects in the link. The number of filter taps needed for the linear step of LDBP is also evaluated, where we show that LDBP can achieve the same performance as DBP with a low number of filter taps.

RQ-4 Which are the best 4D symbol constellations and a priori probabilities when transmitting a signal in the nonlinear fiber?

Paper F: "High-cardinality hybrid shaping for 4D modulation formats in optical communications optimized via end-to-end learning" - in arXiv:2112.10471

We built an autoencoder system where all the system structures are differentiable. With this framework, we were able to jointly optimize the symbol constellation, a priori probabilities, input power, and receiver. The system was optimized for a multi-span multi-channel link. Although we cannot guarantee that we obtained the optimal system structures, we were able to outperform polarization-multiplexed (PM) quadrature amplitude modulation (QAM) constellations (PM-16QAM, PM-32QAM, and PM-64QAM) with a 4D 10 bits/symbol optimized constellation.

CHAPTER 2

Metrics

In this chapter, we define the metrics used in this thesis to evaluate the performance of optical systems. Some of these metrics will be presented in the context of ML, where they are used to optimize system components such as constellation geometry and receiver structure.

2.1 Normalized Square Deviation

The normalized square deviation (NSD) is a metric used to compare two waveforms, where one of them is taken as the reference waveform. This metric consists in taking the energy of the error between the two waveforms and dividing it by the energy of the reference waveform.

In this thesis, we consider functions of both time t and distance z, written as $A(t,z)$. If we assume that A is our reference waveform and A_M is a second given waveform, then the error ξ between A_M and A is

$$\xi(t,z) = A_M(t,z) - A(t,z). \tag{2.1}$$

Based on (2.1), we define the NSD as [6]

$$\text{NSD} \triangleq \frac{\int_{-\infty}^{\infty} |\xi(t,z)|^2 \mathrm{d}t}{\int_{-\infty}^{\infty} |A(t,z)|^2 \mathrm{d}t}, \tag{2.2}$$

where we assume A and A_M are finite energy signals. A high NSD value would mean that the waveform A_M differs significantly from A. A low NSD value would mean that A_M is very similar to A. We define that NSDs below 0.1% are considered low and above 0.1% are considered high.

2.2 Signal-to-Noise Ratio

One commonly used metric to evaluate system performance is the signal-to-noise ratio (SNR). The SNR consists in calculating the power of the transmitted signal, P_s, and dividing it by the power of the noise added by the system, P_n, as

$$\text{SNR} = \frac{P_s}{P_n}. \tag{2.3}$$

The SNR from (2.3) can be computed in discrete time for linearly-modulated systems, via the transmitted and received symbols in a given transmission system. If we transmit N_s symbols $x_k \in S \subset \mathbb{C}$, $1 \leq k \leq N_s$, obtained from a constellation set S, a possible calculation of the SNR is

$$\text{SNR} = \frac{\sum_{k=1}^{N_s} |x_k|^2}{\sum_{k=1}^{N_s} |y_k - x_k|^2}, \tag{2.4}$$

where $y_k \in \mathbb{C}$ is the received symbol when transmitting x_k.

Sometimes the received symbols associated to a specific constellation symbol might have a different expected value from that original constellation symbol. This difference could be originated from a rotation or attenuation/amplification of the received symbols with respect to the transmitted ones, for example. In other words, denoting by s_k a symbol from the M possible ones drawn from the constellation S, we could have $E[Y|X = s_k] \neq s_k$, where X and Y are the random variables associated to the transmitted and received symbols, respectively. In these cases, this might be easily corrected by the receiver DSP and (2.4) would underestimate the SNR. To address these cases, the SNR definition can be slightly changed to account only for the variance of the received noise per constellation point. This new SNR definition for a constellation with M symbols is defined as

$$\text{SNR} = \frac{\sum_{m=1}^{M} |\bar{y}_m|^2}{\sum_{m=1}^{M} \frac{1}{N_m} \sum_{k=1}^{N_m} |y_{km} - \bar{y}_m|^2}, \tag{2.5}$$

where $\bar{y}_m = \frac{1}{N_m} \sum_{k=1}^{N_m} y_{km}$ is the average received symbol corresponding to the m-th constellation point, N_m is the number of times the m-th constellation point was transmitted, and y_{km} is the k-th received symbol given a fixed transmitted m-th constellation point. The SNR in (2.5) is used in Paper B to validate analytical models in discrete time.

2.3 Mutual Information

For some applications, such as constellation or symbol probabilities optimization, the SNR is not an effective metric. If we only transmit a single symbol, or if all the symbols are the same, we could still have a reasonable SNR, while the transmitted data rate would be extremely low. For these situations, other metrics that give an indication of the transmission rates in a channel are more suitable. In this chapter, we will present two of them: the mutual information (MI)—in this section—and the generalized mutual information (GMI)—in the next section.

Consider two N-dimensional random variables $\mathbf{X}$ and $\mathbf{Y}$, representing the transmitted and received symbols, respectively. The MI between $\mathbf{X}$ and $\mathbf{Y}$ is defined as [35, Eq. (3)]

$$I(\mathbf{X};\mathbf{Y}) = E_{\mathbf{X},\mathbf{Y}}\left[\log_2 \frac{p_{\mathbf{X},\mathbf{Y}}(\mathbf{X},\mathbf{Y})}{P_{\mathbf{X}}(\mathbf{X})p_{\mathbf{Y}}(\mathbf{Y})}\right], \tag{2.6}$$

where $p_{\mathbf{X},\mathbf{Y}}$, $P_{\mathbf{X}}(\mathbf{X})$, and $p_{\mathbf{Y}}(\mathbf{Y})$ denote the joint probability density function (PDF) of $\mathbf{X}$ and $\mathbf{Y}$, the probability mass function of $\mathbf{X}$, and the PDF of $\mathbf{Y}$, respectively. In this thesis, we are interested in maximizing metrics using ML. Optimizing MI via ML has been done in [21]. However, this paper is not included in the thesis. We keep this MI description in order to introduce the GMI in Sec. 2.4 and to present Paper F, which is an extension of [21]. For the MI estimation in the ML system, we use a Monte Carlo method based on (2.6). For N_s 4D transmitted symbols from $\mathbb{C}^2$, we can write

$$I(\mathbf{X};\mathbf{Y}) = E_{\mathbf{X},\mathbf{Y}}\left[\log_2 \frac{p_{\mathbf{X}|\mathbf{Y}}(\mathbf{X}|\mathbf{Y})}{P_{\mathbf{X}}(\mathbf{X})}\right] \tag{2.7}$$

$$= \sum_{k=1}^{M} \int_{\mathbb{C}^2} p_{\mathbf{X},\mathbf{Y}}(\mathbf{x}_k, \mathbf{y}) \log_2 \left(\frac{p_{\mathbf{X}|\mathbf{Y}}(\mathbf{x}_k|\mathbf{y})}{P_{\mathbf{X}}(\mathbf{x}_k)}\right) \mathbf{dy} \tag{2.8}$$

$$\approx \frac{1}{\sum_{k=1}^{M} D_k} \sum_{k=1}^{M} \sum_{d=1}^{D_k} \log_2 \left(p_{\mathbf{X}|\mathbf{Y}}(\mathbf{x}_k|\mathbf{y}_{d,k})\right) + \mathrm{H}(\mathbf{X}), \tag{2.9}$$

where D_k is the number of received samples from the k-th constellation symbol in the Monte Carlo estimation and $\mathrm{H}(\mathbf{X}) = -\sum_{k=1}^{M} P(\mathbf{x}_k) \log P(\mathbf{x}_k)$ is the entropy of $\mathbf{X}$. The probabilities $p_{\mathbf{X}}(\mathbf{x}_k)$ are known a-priori and therefore $\mathrm{H}(\mathbf{X})$ is also known. The probabilities $p_{\mathbf{X}|\mathbf{Y}}(\mathbf{x}_k|\mathbf{y}_{d,k})$ are estimated by the ML system. This approach is equivalent to what has been done in [36].

2.4 Generalized Mutual Information

Consider a transmission scenario where each symbol has $m = \log_2 M$ bits and $\mathbf{B}$ is the random variable representing the transmitted bits of a symbol. This binary representation of each symbol is referred as its binary labeling. When optimizing the MI, the binary labeling of each symbol is not taken into account. This could lead to a sub-optimal bit-error-rate (BER) for the system. Therefore, we need a new metric that can account for the symbol labeling. One of these metrics is the generalized mutual information (GMI).

Consider the N-dimensional random variable $\mathbf{Y}$ representing the received symbols. The GMI between $\mathbf{B}$ and $\mathbf{Y}$ is [35, Eq. (12)]

$$\mathrm{GMI} = \max_{s\geq 0} E_{\mathbf{B},\mathbf{Y}}\left[\log_2 \frac{q(\mathbf{B},\mathbf{Y})^s}{\sum_{\mathbf{b}\in\{0,1\}^m} p_{\mathbf{B}}(\mathbf{b}) q(\mathbf{b},\mathbf{Y})^s}\right], \tag{2.10}$$

where the metric $q(\mathbf{B},\mathbf{Y})$ can be defined as $p_{\mathbf{Y}|\mathbf{B}}(\mathbf{Y}|\mathbf{B})$.

Similarly to the MI, in this thesis we use an approximation of (2.10) to use in the context of ML. For the GMI estimation, our approach is the same as that used in [13]. Given K transmitted symbols, the GMI is approximated as [13]

$$\mathrm{GMI} \approx \mathrm{H}(\mathbf{X}) + \frac{1}{K} \sum_{k=1}^{K} \sum_{i=1}^{m} \left[b_{i,k} \log(r_{i,k}) + (1 - b_{i,k}) \log(1 - r_{i,k})\right], \tag{2.11}$$

where $b_{i,k}$ is the i-th bit of the k-th transmitted symbol, and $r_{i,k}$ is the probability $p(b_{i,k} = 1|\mathbf{y}_k)$ given the received symbol $\mathbf{y}_k$. The probability $p(b_{i,k} = 1|\mathbf{y}_k)$ is usually unknown. In the ML context, this probability is estimated while maximizing (2.11).

CHAPTER 3

Analytical Models for Nonlinear Fiber Propagation

3.1 Introduction

In this chapter, we will address some of the analytical models present in the literature for optical fiber propagation. The difference between the models is on the type of approximation made on the common basis equation, the NLSE [1]. Depending on the approximation, a model could have a simple closed-form expression. However, due to the approximation simplicity, the solution obtained from the model could deviate significantly from the true solution of the NLSE. Therefore, a tradeoff between accuracy and simplicity for analytical manipulations exists when approximating solutions of the NLSE.

3.2 The Nonlinear Schrödinger Equation

The noiseless propagation of the optical field E at the retarded time frame t and distance z for a single polarization in a single-mode fiber can be represented by the NLSE [1]

$$\frac{\partial E(t,z)}{\partial z} = \underbrace{-\frac{\alpha}{2}E(t,z)}_{\text{attenuation}} \underbrace{-\frac{j\beta_2}{2}\frac{\partial^2 E(t,z)}{\partial t^2}}_{\text{chromatic dispersion}} \underbrace{+j\gamma|E(t,z)|^2E(t,z)}_{\text{Kerr effect}}, \tag{3.1}$$

where α is the attenuation coefficient, β_2 the group-velocity dispersion (GVD) parameter, and γ the nonlinear coefficient. The first term in (3.1) is responsible for the signal attenuation along the fiber. Typical values for α are around 0.2 dB/km for an SSMF, which is extremely low compared to the attenuation of other channels such as coaxial cables, which can achieve attenuation values from 7 to 1700 dB/km depending on the cable type and frequency [37]. For model derivations, it is common to normalize the field E via

$$E(t,z) = A(t,z)e^{-\frac{\alpha}{2}z}, \tag{3.2}$$

which simplifies (3.1) to

$$\frac{\partial A(t,z)}{\partial z} = \underbrace{-\frac{j\beta_2}{2}\frac{\partial^2 A(t,z)}{\partial t^2}}_{\text{linear term}} + \underbrace{j\gamma e^{-\alpha z}|A(t,z)|^2A(t,z)}_{\text{nonlinear term}}, \tag{3.3}$$

where (3.3) is referred to as the normalized NLSE. From now on, every time we mention the name NLSE, we will be referring to (3.3). The right-hand side of (3.3) has two terms: a linear and a nonlinear one.

If we consider dual-polarization transmission, (3.3) is replaced by the normalized Manakov equation [38]

$$\frac{\partial \mathbf{A}(t,z)}{\partial z} = -\frac{j\beta_2}{2}\frac{\partial^2 \mathbf{A}(t,z)}{\partial t^2} + j\frac{8}{9}\gamma e^{-\alpha z}\left\|\mathbf{A}(t,z)\right\|^2\mathbf{A}(t,z), \tag{3.4}$$

where $\mathbf{A}(t,z) = [A_\mathrm{x}(t,z), A_\mathrm{y}(t,z)]$ is the dual-polarization transmitted signal and A_x and A_y are the signal components in the x and y polarizations, respectively. When considering dual-polarization signals, other effects not modeled in (3.4), such as birefringence, could be present in the transmission.

In the remaining of this chapter, we consider only the single-polarization NLSE in (3.3). The Manakov equation in (3.4) will only be considered in Chapter 4.

3.2.1 Chromatic Dispersion Effect

The linear term in (3.3) is analogous to the second term in (3.1) and represents the CD. To better understand CD, one can solve the simplified NLSE (setting $\gamma = 0$) given only by

$$\frac{\partial A(t,z)}{\partial z} = -\frac{j\beta_2}{2}\frac{\partial^2 A(t,z)}{\partial t^2}. \tag{3.5}$$

The solution of (3.5) in the frequency domain can be expressed as

$$\tilde{A}_\mathrm{CD}(\omega,z) = \tilde{A}(\omega,0)e^{-\frac{j\beta_2}{2}\omega^2 z}, \tag{3.6}$$

where ω is the angular frequency and $\tilde{A}$ is the Fourier transform[1] of A. As shown in (3.6), this solution is an all-pass filter. The solution in (3.6) can also be expressed in the time domain as

$$A_\mathrm{CD}(t,z) = \left(A(\cdot,0) * h(\cdot,z)\right)(t) = \mathcal{D}_z\{A(\cdot,0)\}(t). \tag{3.7}$$

In (3.7), $*$ represents convolution, h is given by

$$h(t,z) = \frac{1}{\sqrt{j2\pi\beta_2 z}}e^{-\frac{j}{2\beta_2 z}t^2}, \tag{3.8}$$

and $\mathcal{D}_z$ is the dispersion operator defined as

$$\mathcal{D}_z\{f\}(t) \triangleq \left(f * h(\cdot,z)\right)(t), \tag{3.9}$$

where f is a function of t.

As shown in (3.6), the CD effect only affects the phase of the input signal $\tilde{A}(\cdot,0)$. The amplitude of $\tilde{A}(\cdot,0)$ is kept intact since (3.6) implies

$$\left|\tilde{A}_\mathrm{CD}(\omega,z)\right| = \left|\tilde{A}(\omega,0)e^{-\frac{j\beta_2}{2}\omega^2 z}\right| = \left|\tilde{A}(\omega,0)\right|. \tag{3.10}$$

Therefore, since $\tilde{A}(\cdot,0)$ represents the spectrum of the input pulse, there is no spectral broadening or narrowing induced by the CD effect only. On the other hand, CD distorts the amplitude of the input pulse $A(\cdot,0)$ in time domain. To visualize the time-domain amplitude

---

[1] We define the Fourier transform of a function $A(\cdot,z)$ as $\tilde{A}(\omega,z) \triangleq \int_{-\infty}^{\infty} A(t,z)\mathrm{e}^{+j\omega t}\mathrm{d}t$, which depends on the angular frequency ω and is evaluated at distance z. The inverse Fourier transform of $\tilde{A}(\cdot,z)$ is $A(t,z) = [1/(2\pi)]\int_{-\infty}^{\infty}\tilde{A}(\omega,z)\mathrm{e}^{-j\omega t}\mathrm{d}\omega$.

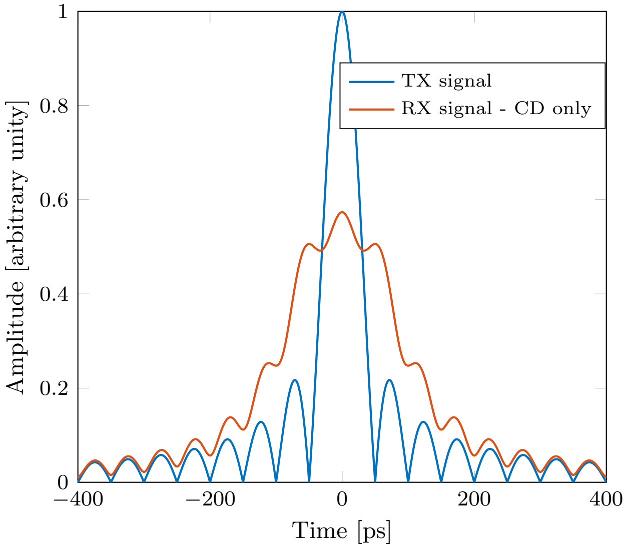

Figure 3.1: Amplitude of a sinc signal before and after transmission in 80 km of a CD-only fiber (3.6) with $\beta_2 = -21.667$ ps^2/km. CD distorts the amplitude in the time domain of the transmitted signal, while keeping its amplitude in the frequency domain unchanged (see (3.10)).

change, Fig. 3.1 shows the propagation of a sinc pulse in 80 km of a CD-only fiber with $\beta_2 = -21.667$ ps^2/km (i.e., CD is the only effect taken into account). The sinc pulse used in the simulation is given by $\sin(2\pi f_0 t)/(2\pi f_0 t)$, where $f_0 = 10$ GHz. As shown in Fig. 3.1, the amplitude of the signal is significantly changed by CD, which can disrupt signal recovery. To reduce the impact of CD in the signal recovery, usually CD compensation (CDC) is employed. CDC consists on applying the inverse CD operator, given by $\mathcal{D}_{-z}$, to the received signal $A(\cdot, z)$.

3.2.2 Kerr Effect

The nonlinear term in (3.3) is similar to the third term in (3.1), where the latter represents the Kerr effect. The only difference is that, in the nonlinear term of (3.3), the Kerr effect is scaled by a factor $e^{-\alpha z}$. To better understand Kerr nonlinearity, we will follow the same approach as for CD. By neglecting the linear term in (3.3), one obtains

$$\frac{\partial A(t,z)}{\partial z} = j\gamma e^{-\alpha z} |A(t,z)|^2 A(t,z), \tag{3.11}$$

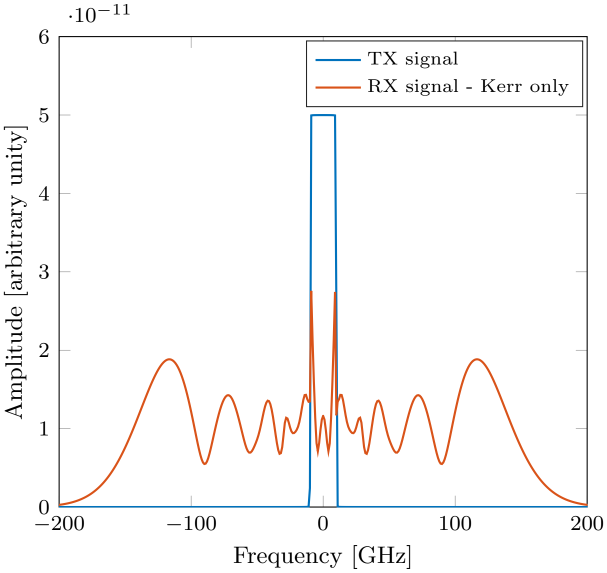

Figure 3.2: Amplitude of the spectrum of a sinc signal before and after transmission in 80 km fiber with only the nonlinear effect in (3.3), with $\alpha = 0.2$ dB/km and $\gamma = 1.2$ 1/W/km. The nonlinear effect changes the amplitude in the frequency domain of the transmitted signal, while keeping its amplitude in the time domain unchanged (see (3.13)).

whose solution is

$$A(t, z) = A(t, 0)e^{j\gamma|A(t,0)|^2 G(z)}, \tag{3.12}$$

where $G(z) = (1 - \exp(-\alpha z))/\alpha$ is the effective length.

As suggested by (3.11), the Kerr effect is strongly dependent on the amplitude of the signal $|A(t, z)|^2$. Since this term represents the squared signal amplitude, signal attenuation would decrease the influence of the Kerr effect as the signal propagates in the fiber. By analyzing the signal amplitude only, one can note that

$$|A(t, z)| = \left| A(t, 0)e^{j\gamma|A(t,0)|^2 G(z)} \right| = |A(t, 0)|\,. \tag{3.13}$$

(3.13) shows that the amplitude of the transmitted signal $A(\cdot, 0)$ does not change in the time domain when only the nonlinear term is considered in (3.3). Only the amplitude of the spectrum of the transmitted signal is affected by the nonlinear term. The change in the spectral amplitude is shown in Fig. 3.2, where the same sinc pulse as used in Sec. 3.2.1 is now subjected to the nonlinear effect only. As illustrated in Fig. 3.2, the spectrum of the transmitted signal is broadened, which could affect neighbor channels in WDM transmissions.

In the case where there is no CD, one can recover the transmitted signal $A(\cdot, 0)$ simply by undoing the nonlinear phase rotation on $A(\cdot, z)$. When CD is considered, compensating for nonlinear effects becomes challenging, since both effects interact with each other, as it will be seen in Fig. 3.5.

3.3 Split-step Fourier Method

In the previous section, we analyzed each effect of the NLSE separately. In this section, we will present the split-step Fourier method (SSFM), which is a numerical method to approximate the received signal when both CD and nonlinearities are considered together.

The SSFM consists in dividing a fiber span into N small spacial steps, each of them with length z_k, $1 \leq k \leq N$. On each of these spacial steps, the CD effect and the nonlinear effect are applied separately. Since the nonlinear effect depends on the amplitude of the input signal (as seen in (3.12)), amplitude attenuation should be taken into account when adding nonlinearities on each step. Therefore, we define a nonlinear operator as

$$\mathcal{N}_{z_n}\{A(\cdot, z_{n-1})\} \triangleq A(t, z_{n-1}) e^{j\gamma\Gamma_n |A(t, z_{n-1})|^2 G(z_n)}, \tag{3.14}$$

$$\Gamma_n = e^{-\alpha \sum_{k=1}^{n-1} z_k}, \tag{3.15}$$

where the factor Γ_n is responsible for decreasing the amplitude of $|A(t, z_{n-1})|^2$, thus emulating the signal attenuation. Using the operators $\mathcal{N}_z$ and $\mathcal{D}_z$ in (3.9) and (3.14), respectively, the output of the SSFM given an input signal $A(\cdot, 0)$ is

$$A(t, z) = \mathcal{N}_{z_N}\{\mathcal{D}_{z_N}\{\mathcal{N}_{z_{N-1}}\{\mathcal{D}_{z_{N-1}}\{\cdots\{\mathcal{N}_{z_1}\{\mathcal{D}_{z_1}\{A(t, 0)\}\}\}\cdots\}\}\}\}, \tag{3.16}$$

where $z = \sum_{k=1}^{N} z_k$. The procedure described by (3.16) is called the asymmetric SSFM and is illustrated in Fig. 3.3. When the lengths z_n are constant, i.e., $z_m = z_n$ for all $1 \leq m, n \leq N$, we say that the SSFM has uniform step sizes. The higher the number of steps N, the more accurate is the SSFM [39].

To reduce the number of steps necessary to achieve a certain accuracy, one could change the steps' distribution. The steps z_n can assume many different distributions depending on the application. One common distribution is the logarithmic distribution, given by [39]

$$z_n = -\frac{1}{c\alpha} \ln\left(\frac{1 - n\delta}{1 - (n-1)\delta}\right), \tag{3.17}$$

where $\delta = (1 - \exp(-c\alpha z))/N$, c is a correction factor to adjust the logarithmic distribution, and $z = \sum_{k=1}^{N} z_k$. Another approach to improve the accuracy of the SSFM is to change to the symmetric SSFM [1, Ch. 2]. The symmetric SSFM consists on applying the nonlinear operator in the middle of each dispersion step, i.e.,

$$A(t, z) = \mathcal{D}_{\frac{z_N}{2}} \Big\{\mathcal{N}_{z_N} \Big\{\mathcal{D}_{\frac{z_N + z_{N-1}}{2}} \Big\{\mathcal{N}_{z_{N-1}} \Big\{\cdots \Big\{\mathcal{N}_{z_1} \Big\{\mathcal{D}_{\frac{z_1}{2}} \{A(t, 0)\}\Big\} \cdots \Big\}. \tag{3.18}$$

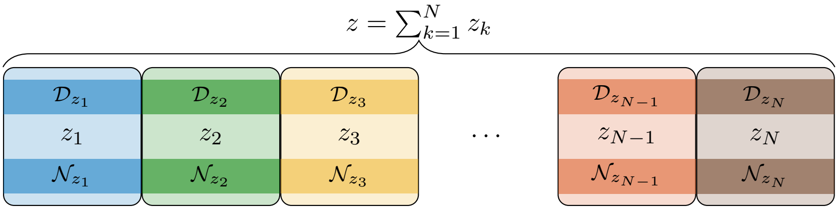

Figure 3.3: Asymmetric implementation of the SSFM. The fiber is divided into N spacial steps. For the n-th spacial step, we apply $\mathcal{N}_{z_n}\{\mathcal{D}_{z_n}\{\cdot\}\}$ to the output of the $(n-1)$-th spacial step.

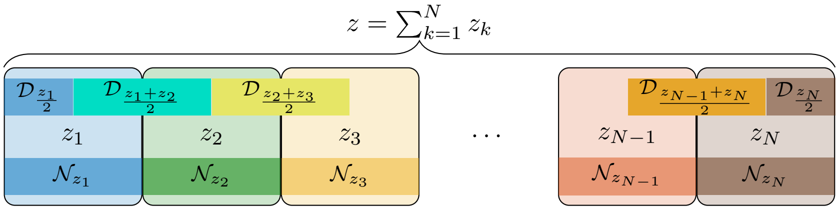

Figure 3.4: Symmetric implementation of the SSFM. The nonlinear operator is applied in the middle of each dispersion step.

An illustration of the symmetric SSFM steps is given in Fig. 3.4.

With the SSFM, one can obtain the received signal after propagation in a fiber considering both CD and Kerr nonlinearity simultaneously. The result for the propagation of the sinc pulse used in the previous sections is presented in Fig. 3.5. As depicted in Fig. 3.5, when both effects are considered, the amplitude in both the time and frequency domain can change significantly from the amplitude obtained when considering the effects independently. Therefore, the interaction of CD and Kerr effects can be non-negligible, and a better understanding on how this interaction occurs is essential.

3.4 Perturbation Models

In Sec. 3.2.1 and 3.2.2, we obtained approximated analytical solutions for the NLSE by neglecting one of the two fiber effects present in (3.3). In this section, we present analytical approximated solutions in closed- or integral-forms considering both effects. These solutions can sometimes provide a better insight into how the fiber effects change the input signal than the SSFM expressions in (3.16) or (3.18).

The approximated solutions in this section are obtained via perturbation theory. Roughly speaking, the perturbation method consists on expressing an unknown function into a power

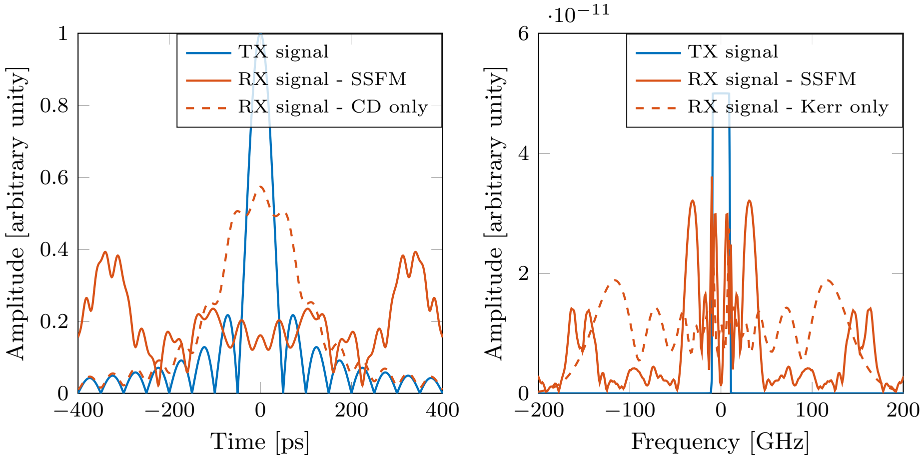

Figure 3.5: Amplitude in time and frequency domain of a sinc pulse before and after transmission in a 80 km fiber $\beta_2 = -21.667$ ps^2/km, $\gamma = 1.2$ 1/W/km, and $\alpha = 0.2$ dB/km. The amplitudes of the received signal differ significantly from the ones obtained when only CD or Kerr effect were considered.

series of functions that are easier to obtain. There are many ways in which this series could be constructed. Two of them are hereby presented: the RP and the LP. The power series is also related to a coefficient, usually present in the initial equation of the unknown function. The chosen coefficient will determine which term in the initial equation should be considered a minor effect. These coefficients could be γ or β_2 in the NLSE case, originating models where the nonlinearities or the dispersion are a minor effect, respectively. We measure the accuracy of each model using the NSD described in Sec. 2.1, where the reference waveform is taken as the output of the SSFM.

3.4.1 Regular Perturbation on γ

The RP on γ was first derived in [6, 7]. To approximate the solution of (3.3), the RP on γ represents the signal by a power series of γ, which can be written as

$$A(t,z) = \sum_{k=0}^{\infty} \gamma^k A_k^{(\gamma)}(t,z). \tag{3.19}$$

To obtain the functions $A_k^{(\gamma)}$, (3.19) is substituted into (3.3) and the terms multiplied by the k-th power of γ are equated. An approximate solution for (3.3) can be obtained by considering only the functions $A_0^{(\gamma)}$ and $A_1^{(\gamma)}$. This approximation is the first-order RP on γ [6, Eqs. (7), (9)], [7, Eq. (12)]

$$A(t,z) \approx A_{\mathrm{RP}}^{(\gamma)}(t,z) = A_0^{(\gamma)}(t,z) + \gamma A_1^{(\gamma)}(t,z), \tag{3.20}$$

where

$$A_0^{(\gamma)}(t,z) = \mathcal{D}_z\{A(\cdot,0)\}(t), \tag{3.21}$$

$$A_1^{(\gamma)}(t,z) = j\int_0^z \mathrm{e}^{-\alpha u}\mathcal{D}_{z-u}\left\{|A_0(\cdot,u)|^2 A_0(\cdot,u)\right\}(t)\mathrm{d}u. \tag{3.22}$$

In (3.20), the first term $A_0^{(\gamma)}$ is the zeroth order. $A_0^{(\gamma)}$ is the same as in (3.7) and accounts for the CD effect only. The second term $A_1^{(\gamma)}$ is the first-order perturbation term and accounts for the combined nonlinear and CD effects. The derivation of the first-order RP on γ can be found in Sec. A.1.

RP on γ is one of the perturbation models with most applications for optical fiber communications. This model has been used to derive low-complexity receivers [5] and also to predict system performance [40, 41]. The latter application is exemplified by the Gaussian-noise (GN) and enhanced GN (EGN) models. The GN/EGN models are a tool to obtain the variance of the nonlinear noise. The nonlinear noise is the signal component that cannot be corrected by CDC and is not related to the amplified spontaneous emission (ASE) noise. With the variance of the nonlinear noise, one can estimate the effective SNR for optical fiber transmission as

$$\mathrm{SNR}_{\mathrm{eff}} = \frac{\sigma_S^2}{\sigma_{\mathrm{ASE}}^2 + \sigma_{\mathrm{NL}}^2}, \tag{3.23}$$

where σ_S^2 is the variance of the signal and σ_{ASE}^2 and σ_{NL}^2 are the variance of the ASE and nonlinear noises, respectively. In (3.23), signal-noise nonlinear interactions are neglected. The use of RP on γ to derive σ_{NL}^2 made it possible to notice that σ_{NL}^2 is approximately proportional to the cube of the signal power P_S, i.e., σ_{NL}^2 can be expressed as ηP_S^3, where η is the nonlinear interference coefficient, which depends on the system parameters.

3.4.2 Enhanced Regular Perturbation on γ

Since the term $A_1^{(\gamma)}$ in (3.22) is proportional to the cube of the signal amplitude, RP on γ starts to diverge from the true solution of the NLSE when the input power increases. A possible way to reduce this problem is to switch to the enhanced RP (ERP) on γ model [6]. The ERP on γ model can be obtained by first performing in (3.3) the change of variables [6]

$$A(t,z) = A_P(t,z)e^{j\gamma P_0 G(z)}, \tag{3.24}$$

where P_0 is here defined as the average power of the signal $A(t,0)$, given by

$$P_0 = \lim_{T\to\infty} \frac{1}{2T} \int_{-T}^{T} |A(t,0)|^2 \mathrm{d}t. \tag{3.25}$$

After some algebra, substituting (3.24) in (3.3) results in

$$\frac{\partial A_P(t,z)}{\partial z} = -\frac{j\beta_2}{2} \frac{\partial^2 A_P(t,z)}{\partial t^2} - j\gamma e^{-\alpha z} P_0 A_P(t,z) + j\gamma e^{-\alpha z} |A_P(t,z)|^2 A_P(t,z). \tag{3.26}$$

Applying the RP method to (3.26), i.e., expressing A_P as a power series of γ, the first-order RP is

$$A_P(t,z) \approx (1 - j\gamma P_0 G(z)) A_0^{(\gamma)}(t,z) + \gamma A_1^{(\gamma)}(t,z), \tag{3.27}$$

which combined with (3.24) forms the ERP on γ model

$$A(t,z) \approx A_{\text{ERP}}^{(\gamma)}(t,z) = \left[(1 - j\gamma P_0 G(z)) A_0^{(\gamma)}(t,z) + \gamma A_1^{(\gamma)}(t,z)\right] e^{j\gamma P_0 G(z)}. \tag{3.28}$$

The accuracy of ERP on γ versus other perturbation models is analyzed in Paper D. For the same input power, ERP on γ is closer to the true solution of the NLSE than RP on γ. However, ERP on γ still deviates from that true solution when the input power increases.

3.4.3 Logarithmic Perturbation on γ

Another approach to increase the accuracy of RP on γ is to perform the LP on γ. LP on γ consists on representing the propagated signal as

$$A(t,z) = A_0^{(\gamma)}(t,z) \exp\left(\sum_{k=1}^{\infty} \gamma^k \psi_k^{(\gamma)}(t,z)\right), \tag{3.29}$$

where the functions $\psi_k^{(\gamma)}$ can be obtained from the RP on γ terms [7]. To show that $\psi_k^{(\gamma)}$ can be obtained via the RP terms, we expand (3.29) in a Taylor series and equate it to (3.19), resulting in

$$\sum_{n=0}^{\infty} \gamma^n A_n^{(\gamma)}(t,z) = A_0^{(\gamma)}(t,z) \sum_{m=0}^{\infty} \frac{1}{m!} \left(\sum_{k=1}^{\infty} \gamma^k \psi_k^{(\gamma)}(t,z)\right)^m. \tag{3.30}$$

The functions $\psi_k^{(\gamma)}$ are now obtained by equating the terms on the right with the ones on the left that are multiplied by the same power of γ. The first-order LP on γ (i.e., truncating (3.29) at $k=1$) is

$$A(t,z) \approx A_{\text{LP}}^{(\gamma)}(t,z) = A_0^{(\gamma)}(t,z) \exp\left(\gamma \frac{A_1^{(\gamma)}(t,z)}{A_0^{(\gamma)}(t,z)}\right). \tag{3.31}$$

3.4.4 Regular Perturbation on β_2

The previous perturbation models were all obtained by applying perturbation theory to the γ coefficient. This resulted in models that consider a low nonlinear effect[2] and that can tolerate high accumulated dispersion, but losing accuracy while the input power increases. To obtain models for the opposite regime, i.e., accurate for weak-dispersion highly-nonlinear regimes, the perturbation methods can be applied on the β_2 parameter.

Similar to RP on γ, one can also express the solution A of (3.3) as a power series of β_2

$$A(t,z) = \sum_{k=0}^{\infty} \beta_2^k A_k^{(\beta_2)}(t,z). \tag{3.32}$$

The terms $A_k^{(\beta_2)}$ can also be found by substituting (3.32) in (3.3) and equating the terms with the same power of β_2. By truncating (3.32), one obtains the first-order RP on β_2

$$A(t,z) \approx A_{\text{RP}}^{(\beta_2)}(t,z) = A_0^{(\beta_2)}(t,z) + \beta_2 A_1^{(\beta_2)}(t,z), \tag{3.33}$$

where

$$A_0^{(\beta_2)}(t,z) = A(t,0)\mathrm{e}^{j\gamma|A(t,0)|^2 G(z)}, \tag{3.34}$$

and

$$A_1^{(\beta_2)}(t,z) = B(t,z)\mathrm{e}^{j\gamma|A(t,0)|^2 G(z)}, \tag{3.35}$$

with B given by

$$\begin{aligned} B(t,z) = &- M(t)z + G_1(z)R(t) + G_2(z)P(t) \\ &- 2j\gamma A(t,0)\Re\{A^*(t,0)V(t,z)\}, \end{aligned} \tag{3.36}$$

$$\begin{aligned} V(t,z) = &\, G(z)\left[M(t)z - G_1(z)R(t) - G_2(z)P(t)\right] \\ &- G_1(z)M(t) + G_2(z)R(t) + G_3(z)P(t), \end{aligned} \tag{3.37}$$

---

[2] For a precise quantification on the models' accuracy versus linear and nonlinear effects, please see Papers B and D.

$$M(t) = \frac{j}{2}\frac{\partial^2 A(t,0)}{\partial t^2}, \tag{3.38}$$

$$R(t) = \frac{\gamma}{2}A(t,0)\frac{\partial^2 |A(t,0)|^2}{\partial t^2} + \gamma\frac{\partial A(t,0)}{\partial t}\frac{\partial |A(t,0)|^2}{\partial t}, \tag{3.39}$$

$$P(t) = \frac{j\gamma^2}{2}A(t,0)\left(\frac{\partial |A(t,0)|^2}{\partial t}\right)^2, \tag{3.40}$$

$$G_1(z) = \frac{\alpha z + \mathrm{e}^{-\alpha z} - 1}{\alpha^2}, \tag{3.41}$$

$$G_2(z) = \frac{2\alpha z + 4\mathrm{e}^{-\alpha z} - \mathrm{e}^{-2\alpha z} - 3}{2\alpha^3}, \tag{3.42}$$

$$G_3(z) = \frac{6\alpha z + 18\mathrm{e}^{-\alpha z} - 9\mathrm{e}^{-2\alpha z} + 2\mathrm{e}^{-3\alpha z} - 11}{6\alpha^4}. \tag{3.43}$$

The derivations of the above equations can be found in the Appendix.

The mathematical expressions for $A_0^{(\beta_2)}$ and $A_1^{(\beta_2)}$ show two main advantages of the RP on β_2 model over RP on γ. The first one is that the complexity of the model is independent of z since G, G_1, G_2, and G_3 are closed-form expressions, while in RP on γ increasing z results in a larger integration domain for (3.22). The second advantage is that the model only depends on derivatives, while (3.22) needs an integral. In addition, only two derivatives are needed, namely $\partial A(\cdot,0)/\partial t$ and $\partial^2 A(\cdot,0)/\partial t^2$, since

$$\frac{\partial |A(t,0)|^2}{\partial t} = 2\Re\left\{A^*(t,0)\frac{\partial A(t,0)}{\partial t}\right\} \tag{3.44}$$

and

$$\frac{\partial^2 |A(t,0)|^2}{\partial t^2} = 2\Re\left\{A^*(t,0)\frac{\partial^2 A(t,0)}{\partial t^2}\right\} + 2\left|\frac{\partial A(t,0)}{\partial t}\right|^2. \tag{3.45}$$

This fact might also result in reduced computational complexity for RP on β_2. Another interesting fact from RP on β_2 is that the term $-M(\cdot)z$ from $B(\cdot,z)$ represents the inverse Fourier transform of the first Taylor expansion term of the function in (3.6).

3.4.5 Frequency Logarithmic Perturbation on β_2

To increase the accuracy of RP on β_2, the frequency LP (FLP) method can be applied. This method consists on applying LP in the frequency domain. FLP on β_2 is represented in the frequency domain as

$$\tilde{A}(\omega,z) = \tilde{A}_0^{(\beta_2)}(\omega,z)\exp\left(\sum_{k=1}^{\infty}\beta_2^k\tilde{\zeta}_k^{(\beta_2)}(\omega,z)\right), \tag{3.46}$$

where the functions $\tilde{\zeta}_k$ are obtained from the functions $\tilde{A}_k^{(\beta_2)}$ similarly to (3.30). By truncating (3.46) at $k = 1$, one obtains the first-order FLP on β_2

$$\tilde{A}(\omega, z) \approx \tilde{A}_{\text{FLP}}^{(\beta_2)}(\omega, z) = \tilde{A}_0^{(\beta_2)}(\omega, z) \exp\left(\beta_2 \frac{\tilde{A}_1^{(\beta_2)}(\omega, z)}{\tilde{A}_0^{(\beta_2)}(\omega, z)}\right). \tag{3.47}$$

The expression in (3.47) is similar to (3.31), where the former is in the frequency domain while the latter is in the time domain.

Analogously to LP on γ, one can use the LP method for the β_2 perturbation. However, in the β_2 case, the LP method should be applied in the frequency domain instead of the time domain for a better accuracy, which represents the FLP method. The opposite is also true for the γ perturbation. The reason behind that fact might lie in the NLSE solutions for Kerr or CD only. As shown in (3.12), the Kerr-only solution is the input signal multiplied by an exponential in the time domain. Since the LP method relies on representing the signal as the exponential in the time domain of a power series of functions (see (3.29)), (3.12) might indicate that LP on γ is more accurate than FLP on γ. On the other hand, the CD-only solution (3.6) is given by the input signal multiplied by an exponential in the frequency domain. Since the FLP method is also obtained by an exponential in the frequency domain, (3.6) might indicate that FLP on β_2 is more accurate than LP on β_2. A further analysis on the accuracy of LP on γ, FLP on γ, LP on β_2, and FLP on β_2 can be found in Paper D.

CHAPTER 4

Machine Learning Applied to Nonlinear Fiber Optics

As mentioned in the previous chapter, fiber-optical propagation is governed by the NLSE. The NLSE can be numerically modeled by the SSFM or analytically modeled, for example, by the analytical models discussed in the previous chapter. Now, we would like to use these modeling tools to increase the transmitted data rate in an optical fiber system. These tools could be used to design receivers or other system components, such as symbol constellations and symbol probabilities, for example. Although these components are aided by the NLSE based models, there is no guarantee that these components are optimally designed.

To try to approach "close to optimum" receivers or constellations, machine learning techniques can be used. In Paper E, a receiver was designed using machine learning and a variation of the SSFM. This receiver used experimental data, which demands additional DSP operations to the received signal. Therefore, in this chapter, we also explain some of the DSP used to recover the received signal in the presence of experimental impairments.

4.1 Basics of Machine Learning

Neural networks (NNs) are structures capable of mimicking functions that many times are unknown a priori. This capability gives NNs the title of universal function approximation [42]. This approximation is built by using training examples of input and output data for the NN. These example data are responsible for the information on the underlying function that should be mimicked. The right choice of training examples is fundamental for the NN performance [43]. In the NNs here studied, we have a system with a certain number of parameters that can change their value in order to minimize a function called "loss". In the next sections, we present the way these parameters are organized and how they change their values according to a certain loss function. A more detailed explanation can be found on [44].

4.1.1 Nodes and Activation Functions

The basic structure of an NN are the layers, which are a set of nodes. There are three types of layers: input layers, hidden layers, and output layers. Each of these layers could have their own dimensions, i.e., number of nodes. To simplify the explanation, an NN with one input layer, one hidden layer and one output layer will be used as example, as shown in Fig. 4.1(a). Consider an input vector $\mathbf{x} = [x_1, x_2, \cdots, x_N]$. The input layer will take the entries of $\mathbf{x}$ and pass to every node of the hidden layer, represented by the green circles in Fig. 4.1(a). When passing the i-th entry to the k-th node in the hidden layer, the entry x_i is multiplied by a weight $w_{i,k}$. For each node in the hidden layer, the sum $\sum_i x_i w_{i,k}$ is computed and a bias factor b_k is added. The result is then used as the argument of the activation function φ_k, which results in the output

$$o_k = \varphi_k\left(\sum_i x_i w_{i,k} + b_k\right), \tag{4.1}$$

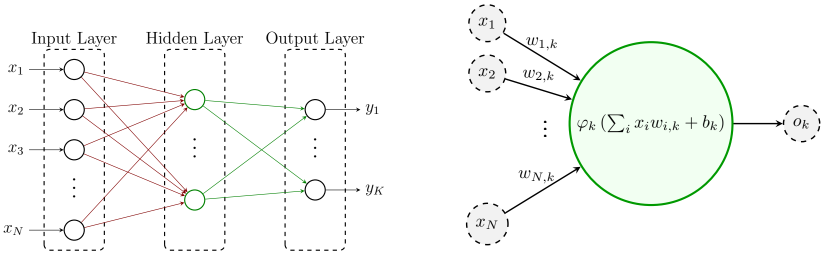

(a) NN structure.

(b) NN hidden node.

Figure 4.1: Schematic of an NN. (a) Representation of an NN structure with three layers. (b) Operations performed inside a hidden node.

as illustrated in Fig. 4.1b. This process is now repeated for the hidden layer and the output layer, where each hidden node output o_k is fed into all the output nodes, with their respective weights, biases, and activation functions. The result of the output layer will be the vector $\mathbf{y} = [y_1, y_2, \cdots, y_K]$, which is fully determined as a function of the NN weights and input $\mathbf{x}$.

The weight and bias in the NN define a linear operation between the input and the output of the nodes. To allow the NN to perform nonlinear operations, the activation function is used. Some of the possible activation functions are the ReLU [45]

$$\varphi_{\text{ReLU}}(x) = \begin{cases} 0, & \text{if } x \leq 0, \\ x, & \text{if } x > 0, \end{cases} \tag{4.2}$$

the sigmoid [45]

$$\varphi_{\text{sigmoid}}(x) = \frac{1}{1 + e^{-x}}, \tag{4.3}$$

and the linear activation function [45]

$$\varphi_{\text{lin}}(x) = x. \tag{4.4}$$

The activation functions should be differentiable (at least almost everywhere) since we will need to compute the gradient of these functions, as will be described in Sec. 4.1.4. For example, ReLU functions are differentiable everywhere but at 0. Although the expression in (4.2) is simple, NNs that use ReLU activation functions are capable of approximate arbitrary convex functions [46].

4.1.2 Loss Function

In a machine learning problem, we usually want to minimize (or maximize) a certain metric. This metric is represented by a function called the loss function, which we will denote by L.

The image of L is the real numbers, since we will need to calculate the gradient of this loss with respect to the NN parameters. In each problem, we might have a different loss function that has to be minimized over the NN parameters. In the problems described in this thesis, we have an input vector $\mathbf{x}$ and an output vector $\mathbf{y}$ from which we compute the loss $L(\mathbf{x}, \mathbf{y})$.

Some examples of loss functions in which $\mathbf{x}$ and $\mathbf{y}$ have the same dimension K are the mean squared error [47]

$$L(\mathbf{x}, \mathbf{y}) = \frac{1}{K} \|\mathbf{x} - \mathbf{y}\|^2 , \tag{4.5}$$

the binary cross-entropy [47]

$$L(\mathbf{x}, \mathbf{y}) = \frac{1}{K} \left(\mathbf{x}^\intercal \log(\mathbf{y}) + (1 - \mathbf{x})^\intercal \log(1 - \mathbf{y})\right) , \tag{4.6}$$

and the MI and GMI between $\mathbf{x}$ and $\mathbf{y}$ described in Chapter 2.

4.1.3 Batches and Epochs

The training procedure consists of updating the weights $w_{i,k}$ and biases b_k of hidden and output layers to minimize the loss function. The loss is calculated each time a set of input vectors is fed into the NN, as will be explained later in this section. In addition, the NN weights and biases are updated. These steps determine an iteration of the training procedure.

The whole dataset used for training can be considered as a set $\mathcal{X}$ of vector of samples $\mathbf{x}_n$. From the set $\mathcal{X}$, one can build subsets $\mathbf{x}^{(k)}$ consisting of m elements from $\mathcal{X}$ drawn from a uniform distribution. The subsets $\mathbf{x}^{(k)}$ are called minibatches, where m is the minibatch size. At each training iteration, a set $\mathcal{B}$ of minibatches is used to compute the loss and update the weights. After all the elements of $\mathcal{X}$ are used for training, we say that an epoch has passed. In the next epoch, new minibatches are extracted from $\mathcal{X}$ to continue the optimization.

4.1.4 Stochastic Gradient Descent

One possible procedure to update the weights and biases of an NN is the stochastic gradient descent (SGD) [44, Ch. 5]. The SGD is applied in each optimization step and we denote the set of parameters, weights, and biases in the whole NN for that step as $\boldsymbol{\theta}$. In the first step, the weights and biases can be randomly initiated according to a given distribution or set to pre-defined values [48]. Given a set of minibatches $\mathcal{B} = [\mathbf{x}^{(1)}, \mathbf{x}^{(2)}, \cdots, \mathbf{x}^{(B)}]$, the gradient is calculated as

$$\mathbf{g}(\boldsymbol{\theta}) = \frac{1}{B} \nabla_{\boldsymbol{\theta}} \sum_{k=1}^{B} L(\mathbf{x}^{(k)}, \mathbf{y}^{(k)}; \boldsymbol{\theta}), \tag{4.7}$$

where $\nabla_{\boldsymbol{\theta}}$ is the gradient operation with respect to $\boldsymbol{\theta}$, $\mathbf{y}^{(k)}$ is the NN system output given the input minibatch $\mathbf{x}^{(k)}$, and $\mathbf{g}(\boldsymbol{\theta})$ has the same dimension as $\boldsymbol{\theta}$. Once the gradient is obtained, the set of parameters is updated to

$$\boldsymbol{\theta}_{\text{new}} = \boldsymbol{\theta} - l\mathbf{g}(\boldsymbol{\theta}), \tag{4.8}$$

where l is a scalar called learning rate.

To calculate the gradient of the loss with respect to a certain parameter, the backpropagation algorithm is usually used [44, Ch. 6]. With this algorithm, the gradient is "backpropagated" through the NN, until it reaches the desired parameter. This backpropagation is based on the chain rule for differentiation. For example, consider a parameter θ, an intermediary variable r such that $r = g(\theta)$ for a certain function g, and the loss function $L(r)$. With the backpropagation algorithm, the gradient of the loss with respect to θ is calculated by

$$\nabla_\theta = \frac{\partial L}{\partial r}\frac{\partial r}{\partial \theta}, \tag{4.9}$$

which, in practice, is performed by first calculating the gradient of L with respect to r and only then the gradient of r with respect to θ.

4.1.5 Adam Optimizer

The learning rate introduced in the end of Sec. 4.1.4 can change over the training epochs. A common approach is to start with a large learning rate and decrease it as the training evolves. The idea behind this procedure is to avoid local minima and speed up the training in the beginning, while performing a fine-tuning in the end of the training. The changes in the learning rate over the epochs can be heuristically determined or can follow an algorithm. The learning rate and the gradient could also follow expressions more elaborated than (4.8).

In the works described in this thesis, we used the Adam optimizer [49] instead of SGD. The Adam algorithm is momentum-based and updates the parameters $\boldsymbol{\theta}$ in a different manner than in (4.8). The detailed description of the Adam optimizer can be found in [49] and its algorithm is shown in Algorithm 4.1.

4.1.6 One-Hot Vectors

In many problems where we need to classify data according to a finite number of categories, it is common to use one-hot vectors (OHVs). OHVs consist of a binary representation of the class to which a certain data belongs where only one entry of the vector is 1 and the others 0. For example, consider a problem where we need to classify if an object is blue, green, or yellow. By creating the following map

$$v_1 = [1 \;\; 0 \;\; 0] \rightarrow \text{blue}, \tag{4.10}$$
$$v_2 = [0 \;\; 1 \;\; 0] \rightarrow \text{green}, \tag{4.11}$$
$$v_3 = [0 \;\; 0 \;\; 1] \rightarrow \text{yellow}, \tag{4.12}$$

one can represent the color of a certain object with only the binary vectors v_1, v_2, and v_3.

Algorithm 4.1: Adam optimization algorithm [49]

```
Data: $\alpha$: Stepsize
Data: $\beta_1, \beta_2 \in [0, 1)$: Exponential decay rates for momentum estimates
Data: $\mathbf{g}$: Gradient calculation
Data: $\boldsymbol{\theta}_0$: Initial set of parameters.
Result: $\boldsymbol{\theta}_E$: Final set of optimized parameters after $E$ epochs
$\mathbf{m}_0 \leftarrow 0$
$\mathbf{v}_0 \leftarrow 0$
$t \leftarrow 0$
for $t \leftarrow 1$ to $E$ do
    $t \leftarrow t + 1$
    $\mathbf{g}_t \leftarrow \mathbf{g}(\boldsymbol{\theta}_{t-1})$
    $\mathbf{m}_t \leftarrow \beta_1 \mathbf{m}_{t-1} + (1 - \beta_1)\mathbf{g}_t$
    $\mathbf{v}_t \leftarrow \beta_2 \mathbf{v}_{t-1} + (1 - \beta_2)\mathbf{g}_t^2$
    $\hat{\mathbf{m}}_t \leftarrow \mathbf{m}_t / (1 - \beta_1^t)$
    $\hat{\mathbf{v}}_t \leftarrow \mathbf{v}_t / (1 - \beta_2^t)$
    $\boldsymbol{\theta}_t \leftarrow \boldsymbol{\theta}_{t-1} - \alpha \hat{\mathbf{m}}_t / (\sqrt{\hat{\mathbf{v}}_t} + \epsilon)$
end
```

4.2 Experimentally Learned Digital Backpropagation

In this section, we describe the main concepts used in Paper E, which are related to the experimental demonstration of LDBP. We start by describing the principle behind LDBP in Sec. 4.2.1. In Sec. 4.2.2, we describe an algorithm used in Paper E that corrects $\mathbb{C}^2$ rotations that are applied to the signal during propagation. This algorithm also has learnable coefficients, which are learned inside the algorithm and not using SGD (or its variations) within the NN. The propagated signal has two polarizations and is governed by (3.4). Other effects not modeled in (3.4) are also present during the experimental propagation, such as the aforementioned $\mathbb{C}^2$ rotations.

4.2.1 Backpropagating the Received Signal

LDBP is based on the DBP method, which consists of digitally propagating the received signal back in the fiber. This procedure follows the same concept as the SSFM described in Sec. 3.3. However, we invert the sign of the fiber parameters in DBP. In the LDBP approach, the sign of γ and α is also inverted. The main difference between those two methods is that in LDBP we replace the linear operator $\mathcal{D}_z$ by finite impulse response (FIR) filters, which will be the base structure of an NN. The input of the NN are the received signal samples $\mathbf{A}[n]$, while the output are the estimated transmitted symbols.

Consider received signal samples $\mathbf{A}[n] = [A_{\mathrm{x}}[n], A_{\mathrm{y}}[n]]$, where $\mathbf{A}$ is an $N_s \times 2$ complex matrix. The k-th step of LDBP can be represented as

$$\mathbf{A}_{k+1} = (\mathbf{A}_k[n] * h[n]) \cdot e^{j\frac{8}{9}\gamma' \|\mathbf{A}_k[n]*h[n]\|^2 G(z)}, \tag{4.13}$$

where $h = [h_{-M}, h_{-(M-1)}, \cdots, h_0, \cdots, h_{M-1}, h_M]^\intercal$ is an FIR filter of length $2M+1$, $\gamma' = -\gamma$, and the squared norm $\|\mathbf{A}[n]\|^2 = |A_\text{x}[n]|^2 + |A_\text{y}[n]|^2$ is taken element-wise. The elements h_i of $h[n]$ are the learnable parameters of the NN. The γ' parameter can also be learned. The elements of $h[n]$ are equivalent to the weights of an NN, while the exponential multiplication in (4.13) represents the nonlinear activation function. The length of the filter is important to determine the overall complexity of LDBP, together with the number of LDBP steps. In Paper E, we vary both the size of the FIR filter and the number of steps to verify how these parameters impact the method performance.

After performing all the LDBP steps, the signal is matched-filtered and sampled. A phase rotation is also applied after sampling to undo the residual phase offset from the channel propagation. These operations result in the estimated transmitted symbols. The estimated symbols, together with the transmitted ones, will be the arguments of the loss function. In the work of Paper E, the chosen loss function was the SNR, as calculated in (2.4). After calculating the loss, the Adam method in Sec. 4.1.5 is applied and the FIR filters updated.

4.2.2 Multiple Modulus Algorithm

During fiber propagation, the signal $\mathbf{A} = [A_\text{x}, A_\text{y}]$ can be rotated in $\mathbb{C}^2$ due to birefringence. These rotations occur along the fiber and estimating their distance evolution might be challenging. However, the accumulated rotation can be undone at the receiver by known DSP algorithms. The algorithm used in Paper E was the multiple modulus algorithm (MMA) [50], which can be applied to constellations whose symbols might have different amplitudes from each other.

In the MMA, a bank of four FIR filters is trained to undo the rotation in the sampled input signal $\mathbf{A}[n]$. We will denote these FIR filters by $h_\text{x,x}, h_\text{x,y}, h_\text{y,x}$ and $h_\text{y,y}$, each of them with size N_taps. These filters are usually initialized as

$$h_\text{x,x} = [0, 0, \cdots, 1, \cdots, 0, 0]^\intercal, \tag{4.14}$$
$$h_\text{x,y} = [0, 0, \cdots, 0, \cdots, 0, 0]^\intercal, \tag{4.15}$$
$$h_\text{y,x} = [0, 0, \cdots, 0, \cdots, 0, 0]^\intercal, \tag{4.16}$$
$$h_\text{y,y} = [0, 0, \cdots, 1, \cdots, 0, 0]^\intercal. \tag{4.17}$$

For the filters' training, usually only a contiguous subset of $\mathbf{A}[n]$ is used, here denoted by $\mathbf{A}'[n]$. From the reduced input signal $\mathbf{A}'[n]$, we extract all the T possible connected subsets of size N_taps where the center sample is aligned with the symbol sampling. These subsets are denoted by $\mathbf{A}'_k$, $1 \leq k \leq T$. The MMA is therefore performed over T iterations, which each start by obtaining

$$\hat{a}_\mathrm{x} = \left\langle h_\mathrm{x,x}, A'_{k,\mathrm{x}} \right\rangle + \left\langle h_\mathrm{x,y}, A'_{k,\mathrm{y}} \right\rangle \tag{4.18}$$

$$\hat{a}_\mathrm{y} = \left\langle h_\mathrm{y,x}, A'_{k,\mathrm{x}} \right\rangle + \left\langle h_\mathrm{y,y}, A'_{k,\mathrm{y}} \right\rangle \tag{4.19}$$

where $\hat{a}_\mathrm{x}$ and $\hat{a}_\mathrm{y}$ are the estimated symbols for the two polarizations given the transmitted a_x and a_y symbols, respectively, and $A'_{k,x}$ and $A'_{k,y}$ are the x and y polarization components of $\mathbf{A}'_k$. Each $h_\mathrm{c,z}$, $c, z \in \{\mathrm{x}, \mathrm{y}\}$, has size $N_\mathrm{taps} \times 1$ and $\mathbf{A}'_k = [\mathbf{A}'_{k,\mathrm{x}}, \mathbf{A}'_{k,\mathrm{y}}]$ has size $N_\mathrm{taps} \times 2$, with each $\mathbf{A}_{k,\mathrm{x}}$ and $\mathbf{A}_{k,\mathrm{y}}$ having size $N_\mathrm{taps} \times 1$. The error associated with the current filters is calculated by

$$\epsilon_\mathrm{x} = 2(|\hat{a}_\mathrm{x}|^2 - |a_\mathrm{x}|^2)\hat{a}_\mathrm{x} \tag{4.20}$$

$$\epsilon_\mathrm{y} = 2(|\hat{a}_\mathrm{y}|^2 - |a_\mathrm{y}|^2)\hat{a}_\mathrm{y} \tag{4.21}$$

when using an aided estimation for the error. The magnitude of the error (4.20) and (4.21) increases when the amplitude of the estimated symbols also increases. Therefore, lowering the magnitude of the error in those equations is equivalent to minimizing the difference between the modulus of the estimated and transmitted symbols. When there is no information on the transmitted symbols a_x and a_y, the algorithm uses the closest symbol amplitude to $\hat{a}_\mathrm{x}$ and $\hat{a}_\mathrm{y}$ given the possible amplitudes in the transmitted symbol set. Using the errors ϵ_x and ϵ_y, the filters are updated by

$$h_\mathrm{x,x} = h_\mathrm{x,x} - \mu\epsilon_\mathrm{x}(A'_{k,x})^* \tag{4.22}$$

$$h_\mathrm{x,y} = h_\mathrm{x,y} - \mu\epsilon_\mathrm{x}(A'_{k,y})^* \tag{4.23}$$

$$h_\mathrm{y,x} = h_\mathrm{y,x} - \mu\epsilon_\mathrm{y}(A'_{k,x})^* \tag{4.24}$$

$$h_\mathrm{y,y} = h_\mathrm{y,y} - \mu\epsilon_\mathrm{y}(A'_{k,y})^*, \tag{4.25}$$

where μ is the MMA learning rate. After running the algorithm for all $\mathbf{A}'_k$, $1 \leq k \leq T$, the filters are applied to the whole signal $\mathbf{A}[n]$. We consider that the time interval corresponding to the duration of $\mathbf{A}[n]$ is small enough such that the rotation induced by the fiber is approximately constant during that interval.

4.3 Shaping Using an Autoencoder

In the LDBP method, the FIR filters at the receiver were optimized by an NN. The NN used as input only the received signal, and the gradient in the Adam method only had to propagate in the receiver structure. However, if we want to optimize the geometry or probabilities of the transmitted constellation, for example, the gradient would need to backpropagate over the channel all the way back to the transmitter. In this case, a structure where all the elements until the transmitter are differentiable is needed. In addition, this structure would also need to generate new inputs, since the input symbols would be modified on every iteration by the learning process. This structure is categorized as an autoencoder [44, Ch. 14]. The results for the autoencoder described in this section can be found in Paper F, Chapter 10.

4.3.1 Autoencoder System for Fiber Propagation

The autoencoder system for fiber propagation can be seen in Fig. 4.2. In Fig. 4.2, the red blocks comprise NN learnable parameters. The system is capable of performing multi-channel transmission, where each channel has its own constellation, probabilities, launch power, and receiver structure. The symbol probabilities, constellation, and bit probability estimation blocks are all built using fully connected layers. Each channel has its own set of layers for each of these blocks. The launch power of each channel is represented by a scalar. The loss function chosen for this structure was the GMI described in Sec. 2.11, which is calculated for each channel separately.

The symbol probability, labeled constellation, and bit probability estimation blocks have the following properties:

- **Symbol probabilities**
  - Input: OHVs of dimension M;
  - Output: Logarithm of the symbol probability for the given symbol represented by the input OHV;
  - Number of hidden layers: 3;
  - Number of nodes in hidden layers: 128 or 256 (depending on M);
  - Hidden layer activation function: ReLU;
  - Output layer activation function: Linear, as in (4.4).
- **Labeled constellation**
  - Input: OHVs of dimension M;
  - Output: Transmitted symbol of 2 or 4 real dimensions;
  - Number of hidden layers: 2;
  - Number of nodes in hidden layers: 128 or 256 (depending on M);
  - Hidden layer activation function: ReLU;
  - Output layer activation function: Linear, as in (4.4).
- **Symbol probability estimation**
  - Input: Received symbol of real dimension 2 or 4;
  - Output: $m = \log_2(M)$ set of disconnected NNs outputting one of the probabilities $p(b_k = 1|\mathbf{y})$ for each bit b_k in the transmitted symbol;

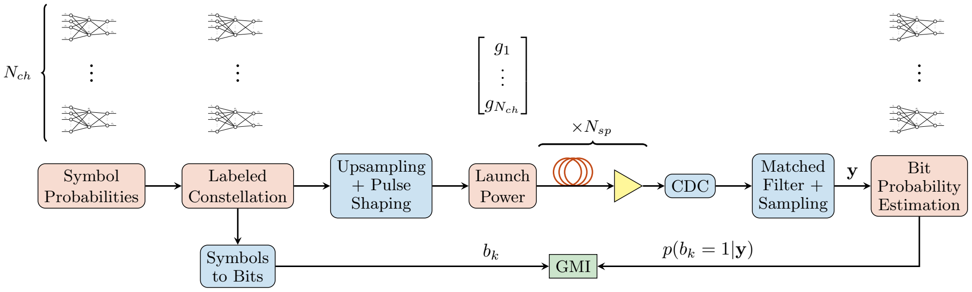

Figure 4.2: Autoencoder system used to learn the geometry and a priory probability of the transmitted symbols. The red blocks are learned by the system. The channel is modeled by the SSFM.

- Number of hidden layers: 3;
- Number of nodes in hidden layers: 128 or 256 (depending on M);
- Hidden layer activation function: ReLU;
- Output layer activation function: sigmoid.

By using the system in Fig. 4.2, all the learnable blocks can be optimized simultaneously. This approach is preferred over optimizing each block individually since the last approach might not result in the best overall result when the blocks are combined. The optimisation is performed jointly over all channels, with separate NNs for each channel in the transmitter and receiver.

4.3.2 Gumbel-Softmax Trick

One of the main challenges in implementing the system in Fig. 4.2 is to backpropagate the gradient to the symbol probabilities in the first block. The difficulty is due to the non-differentiability of the distribution sampling. For example, given a symbol distribution where each symbol from a set of M possible symbols has probability p_i, one could sample from this distribution by performing the Gumbel-Max trick [51, 52]

$$s = \mathrm{OH}\left(\arg\max_i\{g_i + \log p_i\}\right), \tag{4.26}$$

where the function $\mathrm{OH}(i)$ outputs a OHV whose i-th position is 1, and $g_i \in \mathcal{G}$ with $\mathcal{G} = \{g_1, \cdots, g_M\}$ is a set of independent and identically distributed samples drawn from $\mathrm{Gumbel}(0, 1)$ [53]. The problem with (4.26) comes from the fact that the arg max operator is not differentiable. Therefore, the gradient cannot be backpropagated to the symbol probabilities p_i.

A solution to this problem was introduced by [54], called the Gumbel-Softmax trick. Instead of using the OH and arg max operators, the sampling vector $s = [s_1, \cdots, s_M]$ is now given by

$$s_i = \frac{\exp((\log(p_i) + g_i)/\tau)}{\sum_{k=1}^{M} \exp((\log(p_k) + g_k)/\tau)}, \tag{4.27}$$

where τ is a constant called temperature. The vector s is no longer an OHV. However, as the temperature approaches zero, the distribution of s approaches an OHV with probabilities identical to p_i [54].

To apply the Gumbel-Softmax trick in the system of Fig. 4.2, one additional step was performed. After obtaining the vector s, we apply

$$s' = \mathrm{OH}(\arg\max_i \{s_i\}) \tag{4.28}$$

to obtain an OHV, since we should only choose one symbol at a time. This last procedure is known as the straight-through Gumbel-Softmax estimator [54]. Since (4.28) is not differentiable, the backpropagated gradient bypasses this last step. The gradient is able to backpropagate until the probabilities p_i since it is applied to the differentiable expression in (4.27).

Part II

Included Papers

CHAPTER 5

Paper A: Regular perturbation for the weak-dispersion regime

V. Oliari, E. Agrell and A. Alvarado, "Regular perturbation for the weak-dispersion regime," 21st International Conference on Transparent Optical Networks (ICTON), Angers, France, July, 2019.
DOI: 10.1109/ICTON.2019.8840474, *Copyright © 2019, IEEE.*

Abstract

We present a novel analytical model for the lossless fiber in the weak-dispersion regime. The model is compared to three other models via simulations using the split-step Fourier method. These simulations explore the validity of the models with respect to parameters that affect the signal after the fiber propagation. In one of the systems under consideration, the proposed model is accurate until 8.7 dBm while the others are accurate only until 2.4 dBm. The impact of the modulation format is analyzed for three of the models. Our results show differences up to 1.82 dB in the maximum power in which the proposed model remains accurate when changing from quadrature phase shifting keying to 8-ary quadrature amplitude modulation.

5.1 Introduction

The transmission of a signal in an optical fiber is characterized by linear and nonlinear effects [1, Ch. 2]. The linear effects are related to attenuation and chromatic dispersion [1, Ch. 3]. The nonlinear effect can be modeled by the Kerr effect [1, Ch. 4]. The attenuation can be neglected when considering ideal Raman amplification, which maintains the signal power constant during propagation [55]. In that case, the only linear effect remaining is the chromatic dispersion, which can be easily compensated at the receiver by a linear filter, referred to as electronic dispersion compensation (EDC) [56].

An EDC receiver has a better performance for low input powers [56], since in this case the channel is predominantly linear. However, when the input power is high, the Kerr effect becomes significant. In this scenario, to significantly improve the transmission rates, the receiver should also consider the nonlinear effect [57]. To build such a receiver, one may use a mathematical model for the optical channel. These models are generally obtained from the nonlinear Schrödinger equation (NLSE) [1, Ch. 2]. So far in the literature, the solutions of the NLSE are obtained by approximations, which can be numerical or analytical. One of the most accurate approximations is obtained numerically by the split-step Fourier method (SSFM) [58]. In the SSFM, the fiber is represented by a set of small segments, called steps, in which the linear and nonlinear effects can be applied separately. The same method can be applied with the inverse parameters at the receiver and/or transmitter, a process called digital back-propagation (DBP) [28, 59]. DBP can partially compensate the nonlinear and linear effects by choosing a sufficient number of steps. Increasing the number of steps also increases the receiver's computational complexity. To design low-complexity receivers, analytical models are highly desirable.

Analytical models usually consider that either the nonlinear or the linear effect is predominant. In models obtained by degenerated solutions of the NLSE, one of the effects is completely neglected. For example, in the dispersion-only model, the nonlinearity is ignored by setting the nonlinear coefficient γ to zero in the NLSE [1, Ch. 3]. In the nonlinear phase noise (NLPN) model, the chromatic dispersion is ignored by setting the group-velocity dispersion (GVD) parameter β_2 to zero [1, Ch. 4], [60]. Analytical models that consider both effects can be obtained by regular perturbation (RP) theory. A well-known model that uses this theory is the RP on the nonlinear coefficient γ [6,7]. RP on γ considers a low nonlinear effect. This model is appropriate for many known communication systems, and has been used for performance prediction and design of receivers [5,40]. When parameters such as power and γ increase, the model loses its accuracy [6]. In that regime, a new model is necessary. Such a model is not available in the literature yet and will be addressed on this paper.

In this paper, we present a novel model based on RP on the GVD parameter β_2 for a lossless NLSE. In contrast to the RP on γ, the proposed model considers a low dispersion effect and can represent fiber transmission in the highly nonlinear regime. We compare this model with the dispersion-only, NLPN, and RP on γ models and analyze their accuracy for different input powers and modulation formats. The proposed model shows excellent performance for input powers greater than -1 dBm when compared to the other three models. The limits of the model with respect to the bandwidth and fiber length are also analyzed.

5.2 Optical Channel Models

In this section, we present four models for the optical channel. The two first models are degenerated solutions of the NLSE. The third is an RP on the nonlinear coefficient γ and the fourth is our proposed model, an RP on the GVD parameter β_2.

The NLSE for the lossless and noiseless propagation at the retarded frame t and distance z is [1, Ch. 2]

$$\frac{\partial A(t,z)}{\partial z} = -\frac{j\beta_2}{2}\frac{\partial^2 A(t,z)}{\partial t^2} + j\gamma |A(t,z)|^2 A(t,z), \tag{5.1}$$

where γ is the nonlinear Kerr coefficient and β_2 is the GVD parameter. We obtain the solution A of (5.1) numerically using the SSFM. To compare this solution with the signal A_M obtained from a model, the normalized square deviation (NSD) metric is used. The NSD is defined as [6, eq. 27]

$$\text{NSD} \triangleq \frac{\int_{-\infty}^{\infty} |A_M(t,z) - A(t,z)|^2 \text{d}t}{\int_{-\infty}^{\infty} |A(t,z)|^2 \text{d}t}. \tag{5.2}$$

A model will be considered accurate if it has an NSD lower than $0.1\ \%$. The power in which a model has that value of NSD is defined as $P_{0.1\%}$ in this paper.

5.2.1 Dispersion-only Model

If we set $\gamma = 0$, (5.1) becomes

$$\frac{\partial A_M(t,z)}{\partial z} = -\frac{j\beta_2}{2}\frac{\partial^2 A_M(t,z)}{\partial t^2}, \tag{5.3}$$

which admits a solution, given in the Fourier domain by [1, Ch. 3]

$$\tilde{A}_M(\omega, z) = \tilde{A}(\omega, 0)e^{\frac{j\beta_2}{2}\omega^2 z}. \tag{5.4}$$

We call the solution of (5.4) the dispersion-only model. This model is an all-pass filter, and causes pulse-width variation [1, Ch. 3], [61, Sec. 3.1.1].

5.2.2 Nonlinear Phase Noise Model

By setting $\beta_2 = 0$, the NLSE in (5.1) turns into

$$\frac{\partial A_M(t, z)}{\partial z} = j\gamma |A_M(t, z)|^2 A_M(t, z), \tag{5.5}$$

which also admits an analytical solution [1, Ch. 4]

$$A_M(t, z) = A(t, 0)e^{j\gamma |A(t,0)|^2 z}. \tag{5.6}$$

The solution (5.6) is called the NLPN model. In analogy with the dispersion-only model, the NLPN model does not affect the amplitude of the time-domain signal. In the frequency domain, (5.6) causes spectral variation [1, Ch. 4], [61, Sec. 3.1.2].

5.2.3 Regular Perturbation on γ

The first order of a regular perturbation on γ is a model that consider the dispersion effect as the main fiber effect. The model is described in the frequency domain as [6]

$$\tilde{A}_M(\omega, z) = \tilde{A}(\omega, 0)e^{\frac{j\beta_2}{2}\omega^2 z} + j\gamma \int_0^z e^{\frac{j\beta_2}{2}\omega^2 (z-u)} \tilde{S}(\omega, u)\mathrm{d}u, \tag{5.7}$$

where $\tilde{S}$ is the Fourier transform of

$$S(t, z) = |A_0(t, z)|^2 A_0(t, z), \tag{5.8}$$

and $A_0(t, z)$ is the inverse Fourier transform of $\tilde{A}(w, 0)e^{\frac{j\beta_2}{2}w^2 z}$ in (5.4). The first term in the right-hand side of (5.7) accounts only for the dispersion effect. The second term considers the nonlinear and the dispersion effects together. This can be seen by the similarity between the function S and the last term in (5.1).

5.2.4 Proposed Model: Regular Perturbation on β_2

We present a first-order RP on β_2. In this model, the main effect is nonlinearity. The model is given by

$$A_M(t,z) = A(t,0)e^{+j\gamma|A(t,0)|^2 z} + \beta_2 B(t,z)e^{+j\gamma|A(t,0)|^2 z}, \tag{5.9}$$

where

$$B(t,z) = -\int_0^z F(t,u)\mathrm{d}u - 2j\gamma A(t,0)\Re\left\{A^*(t,0)\int_0^z (z-u)F(t,u)\mathrm{d}u\right\}, \tag{5.10}$$

$$F(t,z) = \frac{j}{2}\frac{\partial^2}{\partial t^2}\left\{A(t,0)e^{+j\gamma|A(t,0)|^2 z}\right\}e^{-j\gamma|A(t,0)|^2 z}. \tag{5.11}$$

The first term in the right-hand side of (5.9) accounts for the nonlinear effect only. The second term also accounts for the mix of dispersion and nonlinear effects. The relationship between this last term and the dispersion is observed in the second-order derivative in (5.11). In this paper, we motivate the model by numerical simulations, deferring the theoretic analysis to a future publication due to space constrains.

5.3 Numerical Analysis

5.3.1 System Parameters

In the system under consideration, we transmit symbols using M-ary quadrature amplitude modulation (M-QAM). The value of M is varied to analyze the impact of the modulation format on the models. For $M = 4$, the 4-QAM modulation is called quadrature phase-shift keying (QPSK). The symbols modulate the amplitude of root-raised cosine (RRC) pulses with a roll-off factor of 0.1. The resulting signal is transmitted over a nonzero dispersion-shifted fiber (NZDSF) with parameters given in Table 5.1.

Table 5.1: Fiber parameters

Parameter	Value
Wavelength λ [nm]	1550
Symbol Rate [Gbaud]	10
Fiber Length [km]	60
β_2 [ps^2/km]	-5.42
γ [1/W/km]	1.46

In an NZDSF, the value of $|\beta_2|$ is lower than in a standard single-mode fiber (with typically $\beta_2 = -21.67$ ps^2/km). This fact provides a regime where the accumulated dispersion is low for the respective fiber length and symbol rate. Changing these two last parameters significantly affect the model accuracy. This will be investigated in the next section.

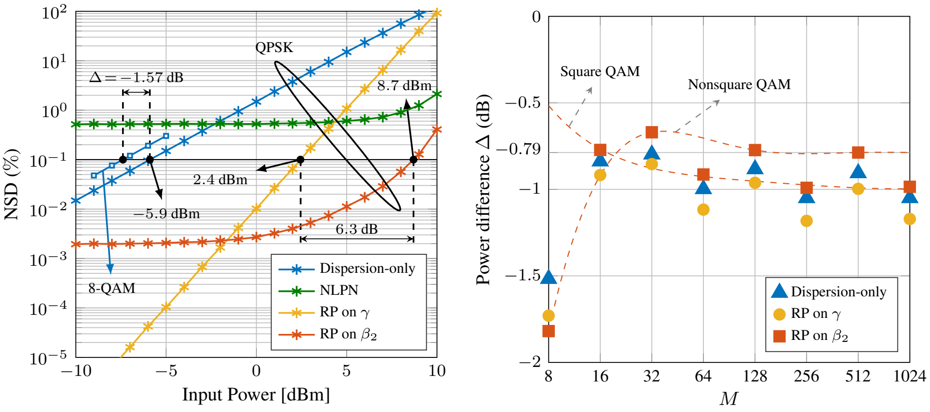

(a) QPSK.

(b) $P_{0.1\ \%}$ difference with respect to QPSK.

Figure 5.1: Simulation results for the system given by the parameters in Table 5.1. (a) NSD versus input power for the four different model with QPSK modulation. (b) Difference Δ between $P_{0.1\ \%}$ for M-QAM modulation ($M \geq 8$) and QPSK.

5.3.2 Simulation Results

Fig. 5.1(a) shows the NSD in (5.2) versus input power for the four models with QPSK modulation. As depicted in Fig. 5.1(a), the dispersion-only and NLPN models have a worse performance than the RP on β_2 in the entire simulated range of powers. While for RP on β_2 $P_{0.1\%} \approx 8.7$ dBm, the second highest $P_{0.1\%}$ is approximately 2.4 dBm, for RP on γ. This difference shows that the RP on β_2 is accurate until powers more than 6.3 dB greater than the other models. The higher $P_{0.1\%}$ of RP on β_2 shows more tolerance to power changes, even though RP on γ is more accurate for powers below -2 dBm. Fig. 5.1(a) also illustrates the dispersion-only model with rectangular 8-QAM modulation in a reduced range of powers. The change in the modulation format introduces a difference Δ between $P_{0.1\%}$ for 8-QAM and QPSK of -1.57 dB.

The difference Δ is generalized in Fig. 5.1(b) for other modulation formats, always with respect to QPSK. Fig. 5.1(b) illustrates the difference Δ between M-QAM modulation formats and QPSK for the dispersion-only, RP on γ and RP on β_2 models. The NLPN is not considered in this figure since it does not cross the 0.1 % threshold (see Fig. 5.1(a)). As shown in Fig. 5.1(b), the three models have a negative Δ for $M \geq 8$. For $M \geq 16$, RP on γ has a lower Δ than the other models. The lowest Δ for the three models occurs at $M = 8$, which is the most nonsquare M-QAM. For that modulation format, RP on β_2 presents a $P_{0.1\%}$ 1.82 dB lower than for QPSK. Nevertheless, the other nonsquare modulation formats (odd $\log_2 M$) converge to a higher Δ than the square ones (even $\log_2 M$). This behavior is depicted with

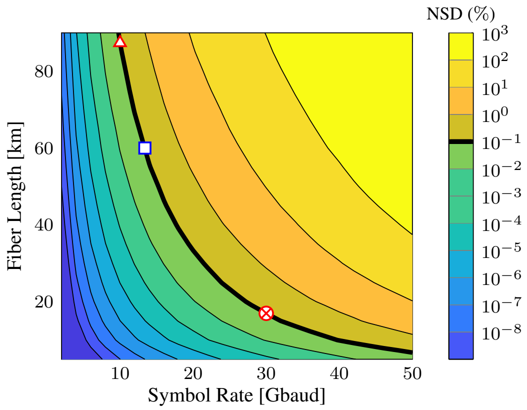

Figure 5.2: NSD for RP on β_2 at different symbol rates and fiber lengths. We considered a QPSK signal with 5 dBm input power.

dashed lines for RP on β_2, with $\Delta = -0.79$ dB and $\Delta = -1.00$ dB, respectively.

Fig. 5.2 shows the NSD for RP on β_2 at different combinations of symbol rate and fiber length, considering QPSK. As illustrated in Fig. 5.2, increasing the fiber length and/or the symbol rate deteriorates the performance of the model. This behavior can be justified using (5.4). The dispersion effect increases with the distance and square of the signal bandwidth, and the later increases linearly with the symbol rate. Therefore, the approximation made by RP on β_2 becomes worse, increasing the NSD. Using the same symbol rate of 10 Gbaud used in the previous example, the fiber could be extended to approximately 87.4 km keeping the model accurate (△ in Fig. 5.2). Fixing the fiber length to 60 km, the symbol rate could be increase to only 13.4 Gbaud (□). When targeting higher symbol rates, the reach distance is significantly decreased. For 30 Gbaud, the model is accurate for a maximum fiber length of 17.0 km (⊗).

5.4 Conclusions

We presented in this paper a novel model for the weak-dispersion regime in a lossless fiber, which can be used even with high nonlinearity. The proposed model accurately represents the fiber output until an input power of 8.7 dBm in the system under consideration. The modulation format impacts the performance of the models, especially when comparing QPSK and 8-QAM. The effect of changes in the symbol rate and fiber length was also analysed, which showed a high sensitivity of the model to these two parameters. Deriving a receiver based on the proposed model and finding higher-order perturbations on β_2 are possible extensions of the work.

CHAPTER 6

Paper B: Regular perturbation on the group-velocity dispersion parameter for nonlinear fibre-optical communications

V. Oliari, E. Agrell and A. Alvarado, “Regular perturbation on the group-velocity dispersion parameter for nonlinear fibre-optical communications,” *Nature Communications*, vol. 11, no. 933, Feb., 2020.
DOI: 10.1038/s41467-020-14503-w, *Copyright © 2020, Nature Communications*.

Abstract

Communication using the optical fibre channel can be challenging due to nonlinear effects that arise in the optical propagation. These effects represent physical processes that originate from light propagation in optical fibres. To obtain fundamental understandings of these processes, mathematical models are typically used. These models are based on approximations of the nonlinear Schrödinger equation, the differential equation that governs the propagation in an optical fibre. All available models in the literature are restricted to certain regimes of operation. Here, we present an approximate model for the nonlinear optical fibre channel in the weak-dispersion regime, in a noiseless scenario. The approximation is obtained by applying regular perturbation theory on the group-velocity dispersion parameter of the nonlinear Schrödinger equation. The proposed model is compared with three other models using the normalized square deviation metric and shown to be significantly more accurate for links with high nonlinearities and weak dispersion.

6.1 Introduction

Optical fibre propagation can be modelled by the nonlinear Schrödinger equation (NLSE) [1]. The NLSE is a partial differential equation that has three main effects: attenuation, second order dispersion, and Kerr nonlinearity. When considering the three effects together, the NLSE has no analytical solution for an arbitrary input pulse. The solution is obtained via a numerical method known as split step Fourier method (SSFM) [1, 58]. The SSFM divides the fibre in small segments, known as steps, and increasing the number of steps increases the method's accuracy [39, 58]. For a high number of steps, the method's computational complexity is a limiting factor [29]. To overcome this limitation, analytical models are generally used.

An analytical model that is easily mathematically manipulable is highly desirable as it can be used for improving fibre-optical transmission. Since models are approximations of the NLSE, they can be used to build improved receivers and mitigate fibre effects [5, 62–64], design signal shaping and coding [65, 66], to estimate channel capacity [66–70], and even to predict system performance [40, 41]. An extensive review on optical channel models can be found in [66]. Each model will have a regime of operation based on the approximation used to derive it. The regimes classify models with respect to the group-velocity dispersion parameter β_2 (which in this paper we refer to as the linear coefficient), the Kerr nonlinear coefficient γ, and the input power.

Some of the main regimes of operation and models present in the literature are schematically represented in Fig. 6.1. If both the linear and nonlinear coefficients are zero, the fibre degenerates to an additive Gaussian noise (AWGN) channel (in the presence of noise), and no interesting effects of the fibre propagation appear. One of the simplest regimes that accounts for fibre propagation effects is when the linear coefficient is zero ($\beta_2 = 0$), represented by the green region ② of Fig. 6.1. In this case, the NLSE is modelled by a nonlinear phase shift [1], known as the nonlinear phase noise (NLPN) model [60, 67]. The assumption of a zero linear coefficient results in a memoryless channel. This assumption was used in the literature,

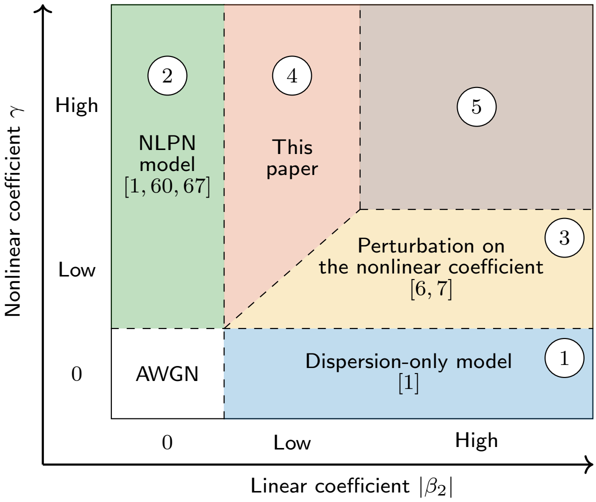

Figure 6.1: Validity region for different models for the nonlinear Schrödinger equation. Each region is characterized by a combination of $|\beta_2|$ and γ values. The models are derived by using approximations based on the magnitude of these two parameters.

for example, when chromatic dispersion is completely compensated [71]. The same premise was considered when analysing the highly nonlinear regime, i.e., when the nonlinearities are predominant and may be an important effect to take into account [68, 72]. As will be seen in the Results section, even in that regime the dispersion can deteriorate the performance of the model.

Another simple model arises when the nonlinear coefficient is zero ($\gamma = 0$), represented by the blue region ① of Fig. 6.1. In this case, the NLSE again admits an exact solution given by the so-called dispersion-only model [1]. This model considers the fibre propagation as an all-pass filter, whose phase response grows with the square of the frequency. Since the model considers zero nonlinearities, it is ideal for low power regimes, where the dispersion is the major effect.

For high power regimes, if the nonlinear coefficient is low but nonzero, the dispersion-only model becomes inaccurate, as will be shown in the Results section. In such scenario, regular perturbation (RP) theory on the nonlinear coefficient [6,7,27] becomes a more suitable model, represented by the yellow region ③ in Fig. 6.1. The nonlinearities depend on the signal times the square of the absolute value of the signal, as will be seen in the nonlinear term of equation (6.3). This dependence makes the nonlinearities grow with the cube of the signal power, thus compromising the accuracy of the RP for high powers [6, 7]. As will be shown in the Results section, RP on the nonlinear coefficient is accurate for a wider range of powers than the dispersion-only model. This wider range allows the RP model to model

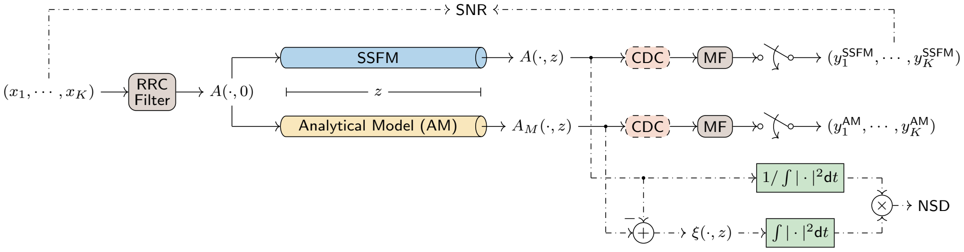

Figure 6.2: Schematic of NSD and SNR calculations. The transmitted symbols $(x_1, \cdots, x_K)$ are filtered by a root-raised-cosine (RRC) filter, originating the input signal $A(\cdot, 0)$. This input signal is processed either by the SSFM or by an analytical model (AM), resulting in the outputs $A(\cdot, z)$ and $A_M(\cdot, z)$, respectively. The NSD is obtained from the SSFM output $A(\cdot, z)$ and a model output $A_M(\cdot, z)$, while the SNR is obtained from the transmitted symbols $(x_1, \cdots, x_K)$ and with the received symbols $(y_1, \cdots, y_K)$ from the SSFM or from an analytical model. To obtain the received symbols, the output waveforms are submitted to an optional chromatic dispersion compensation (CDC) block, followed by a matched filter (MF) and sampling.

many communication systems [27, 64]. The assumption of low nonlinearity is also used for other models, such as logarithmic perturbation [7] and Volterra series [73]. With respect to the Volterra series model, it was proved in [6] that its $(2n + 1)$-th order is equivalent to the n-th order RP on the nonlinear coefficient model.

The mentioned models only cover regions ①, ②, and ③ of Fig. 6.1. Models for the red region ④ and the brown region ⑤ do not exist in the published literature. The latter represents regimes where both the linear and nonlinear coefficient are high, and might not be achievable by perturbation models since, by the RP's definition, one of the coefficients should be low. In region ④, the absolute value of the linear coefficient is low; therefore, performing a regular perturbation is a reasonable approach.

In this paper, we propose a perturbation on the linear coefficient of the NLSE, providing a model for the weak-dispersion regime represented by region ④. The proposed RP on the linear coefficient covers regimes where the nonlinear coefficient is high, and in contrast to the NLPN model, small amounts of dispersion are allowed. The RP on the linear coefficient is a model in closed mathematical form, and depends on the input field and the fibre parameters. A closed-form equation is derived for the continuous-time fibre output with single polarization. The proposed model is compared with the RP on the nonlinear coefficient, the dispersion-only, and the NLPN models. For comparison purposes, the fibre and simulation parameters (such as bandwidth and span length) are varied to identify regimes where each model is accurate. As will be shown in this paper, the RP on the linear coefficient is accurate for a wider range of powers than the RP on the nonlinear coefficient in low accumulated dispersion systems.

6.2 Results

6.2.1 Fibre propagation and metrics

The noiseless propagation of the optical field E at the retarded time frame t and distance z for a single polarization in a single-mode fibre can be represented by the NLSE [1]

$$\frac{\partial E(t,z)}{\partial z} = -\frac{\alpha}{2}E(t,z) - \frac{j\beta_2}{2}\frac{\partial^2 E(t,z)}{\partial t^2} + j\gamma|E(t,z)|^2E(t,z), \tag{6.1}$$

where α is the attenuation coefficient, β_2 the group-velocity dispersion parameter, and γ the nonlinear coefficient. When normalizing the field E via

$$E(t,z) = A(t,z)\mathrm{e}^{-\frac{\alpha}{2}z}, \tag{6.2}$$

equation (6.1) is simplified to

$$\frac{\partial A(t,z)}{\partial z} = \underbrace{-\frac{j\beta_2}{2}\frac{\partial^2 A(t,z)}{\partial t^2}}_{\text{linear term}} + \underbrace{j\gamma\mathrm{e}^{-\alpha z}|A(t,z)|^2A(t,z)}_{\text{nonlinear term}}. \tag{6.3}$$

By writing the NLSE as equation (6.3), the RP method can be more easily applied.

This version of the NLSE disregards dual-polarization effects, such as polarization-mode dispersion, as well as other effects like stimulated Raman scattering. The latter can be reasonably ignored given the low bandwidth scenarios studied in this paper [1]. We chose to analyse the single-polarization equation as a first step towards RP on β_2. Nevertheless, single-polarization transmission is still attractive for low cost optical systems [74].

The first and second terms on the right-hand side of equation (6.3) are linear and nonlinear terms in the NLSE. In this paper, for simplicity, we will refer to them as linear and nonlinear terms, respectively, even though they refer to a normalized version of equation (6.1). When both the linear and nonlinear terms are considered together, there is no analytical solution for equation (6.1) for an arbitrary input pulse $A(\cdot,0)$. However, by setting $\beta_2 = 0$ or $\gamma = 0$, it is possible to obtain simple analytical solutions [1]. These solutions are the basis of the models described below, and each of them has a regime where they can predict well the NLSE solution of equation (6.3).

In this paper, to quantify how well a model approximates the solution of the NLSE in equation (6.3), we will use a metric that relates the error between two waveforms: the normalized square deviation (NSD) (previously used in [6]). The output of the SSFM algorithm will be considered as the solution A of equation (6.3). The NSD calculation between $A(\cdot,z)$ and its approximation made by a certain model $A_M(\cdot,z)$ is illustrated in Fig. 6.2. For a certain propagation distance $z > 0$, the error ξ between the model and the fibre output A is

$$\xi(t,z) = A_M(t,z) - A(t,z). \tag{6.4}$$

Based on equation (6.4), we define the NSD as

$$\mathrm{NSD} \triangleq \frac{\int_{-\infty}^{\infty} |\xi(t,z)|^2 \mathrm{d}t}{\int_{-\infty}^{\infty} |A(t,z)|^2 \mathrm{d}t}. \tag{6.5}$$

The NSD captures the average of the squared absolute error over the time dimension, which corresponds to the error energy. To enable a fair comparison between different input powers, the NSD is normalized by the energy of the fibre output $A(\cdot, z)$. Following [7], we will use a threshold of 0.1% for comparing models. We will say that a model is precise if it gives an NSD below 0.1%.

In addition to the NSD, which characterizes the continuous-time performance, we also observe the discrete-time output, for which the signal-to-noise ratio (SNR) is a suitable metric. As shown in Fig. 6.2, we transmit a sequence of K symbols $(x_1, \cdots, x_K)$, shaped by a root-raised-cosine (RRC) filter. The receiver consists of an optional chromatic dispersion compensation (CDC) block, followed by a matched filter and sampling. Even though no noise is added to the system, the received symbols are not exactly the transmitted ones. This difference is due to limitations on the linear receiver we assume, which cannot undo the fibre propagation effects on the signal. Therefore, the SNR only accounts for signal–signal interactions in this case.

The SNR for a constellation with M symbols is defined as

$$\mathrm{SNR} = \frac{\sum_{m=1}^{M} |\bar{y}_m|^2}{\sum_{m=1}^{M} \frac{1}{N_m} \sum_{k=1}^{N_m} |y_{km} - \bar{y}_m|^2}, \tag{6.6}$$

where $\bar{y}_m = \frac{1}{N_m} \sum_{k=1}^{N_m} y_{km}$ is the average received symbol corresponding to the m-th constellation point, N_m is the number of times the m-th constellation point was transmitted, and y_{km} is the k-th received symbol given a fixed transmitted m-th constellation point. This SNR calculation assumes that we know the corresponding transmitted symbol for a given received symbol, and that the mean values $\bar{y}_m$ would be the signal components with ideal reception.

Notation convention: throughout this paper, we use $A(\cdot, z)$ to represent the evaluation of a two-variable function A that depends on the retarded time frame, evaluated at distance z. In other words, we use this notation to emphasize that $A(\cdot, z)$ is still a function of the retarded time frame. The complex conjugate of A is denoted by A^*. $\Re\{\cdot\}$ and $\Im\{\cdot\}$ give the real and imaginary parts of a complex number, respectively. Operators are denoted by calligraphic letters.

The numerical examples we will present investigate the limits and the operational regimes of each model. To vary the group-velocity dispersion, two types of fibre were considered: standard single-mode fibre (SSFM) and nonzero dispersion-shifted fibre (NZDSF). The SSMF has $\alpha = 0.2$ dB km^{-1}, $\beta_2 = -21.67$ ps^2 km^{-1}, and $\gamma = 1.2$ W^{-1} km^{-1}, while the considered NZDSF has $\alpha = 0.22$ dB km^{-1}, $\beta_2 = -5.42$ ps^2 km^{-1}, and $\gamma = 1.46$ W^{-1} km^{-1}. Except in the symbol rate variation analysis, all the simulations consider a symbol rate of 10 Gbaud. The modulation format is 64-ary quadrature amplitude modulation (64-QAM) unless otherwise stated.

In what follows, we review 3 models available in the literature and then, present the RP on β_2.

Dispersion-only model

When considering $\gamma = 0$, equation (6.3) simplifies to [1]

$$\frac{\partial A_M(t,z)}{\partial z} = -\frac{j\beta_2}{2}\frac{\partial^2 A_M(t,z)}{\partial t^2}, \tag{6.7}$$

which has the exact solution [75]

$$A_M(t,z) = \left(A(\cdot,0) * h(\cdot,z)\right)(t) = \mathcal{D}_z\{A(\cdot,0)\}(t). \tag{6.8}$$

In equation (6.8), $*$ represents convolution, h is given by

$$h(t,z) = \frac{1}{\sqrt{j2\pi\beta_2 z}}\mathrm{e}^{-\frac{j}{2\beta_2 z}t^2}, \tag{6.9}$$

and $\mathcal{D}_z$ is the dispersion operator defined as

$$\mathcal{D}_z\{f\}(t) \triangleq \left(f * h(\cdot,z)\right)(t), \tag{6.10}$$

where f is a function of t. The solution in equation (6.8) is called the dispersion-only model, and is a linear, time-invariant all-pass filter. It corresponds to ① in Fig. 6.1.

Example 6.1. Figure 6.3a shows the NSD vs. input power for the dispersion-only model for the SSMF and an NZDSF. As shown in Fig. 6.3a, the model is an accurate approximation of the fibre output in this system for power lower than +2 dBm for the 10 km fibre. This is as a regime where the nonlinearities are not predominant. As the input power increases, the NSD increases approximately by 2 dB/dBm. This figure also shows that a change in β_2 of approximately 4 times does not considerably change the NSD. By increasing the distance from 10 to 80 km, the NSD grows almost one order of magnitude, which can be justified by the extended interaction between the nonlinearities and the chromatic dispersion, not modelled in this solution.

6.2.2 Nonlinear phase noise model

For $\beta_2 = 0$, equation (6.3) simplifies to [1]

$$\frac{\partial A_M(t,z)}{\partial z} = j\gamma\mathrm{e}^{-\alpha z}|A_M(t,z)|^2 A_M(t,z), \tag{6.11}$$

which has the exact solution

$$A_M(t,z) = A(t,0)\mathrm{e}^{j\gamma|A(t,0)|^2 G(z)}, \tag{6.12}$$

where

$$G(z) = \int_0^z \mathrm{e}^{-\alpha u} \mathrm{d}u = \frac{1 - \mathrm{e}^{-\alpha z}}{\alpha} \tag{6.13}$$

is the effective length. The solution in equation (6.12) is called the nonlinear phase noise (NLPN) model, and is a memoryless, signal-dependent phase shift. This model is ② in Fig. 6.1.

Example 6.2. Figure 6.3b shows the NSD of the NLPN model for the same scenario as Example 6.1. For the NLPN, increasing the value of $|\beta_2|$ (changing from NZDSF to SSMF) can deteriorate the NSD by a factor of almost ten times for the same distance at 0 dBm. This effect can be justified by the increased dispersion contribution to the signal, not modelled by this solution. Furthermore, the accumulated dispersion is also increased when extending the fibre length from 10 to 80 km, which increases the NSD by two orders of magnitude. This last increase can also be seen by the fact that, at long distances, $G(z) \approx 1/\alpha$ and equation (6.12) barely changes with respect to z. However, this result is not consistent with the actual fibre output, which still depends on the distance z in the presence of chromatic dispersion. Although only the 10 km NZDSF presented an NSD below the threshold of 0.1%, the NLPN model has an NSD almost constant for powers lower than 10 dBm.

6.2.3 Regular perturbation on γ

The RP method consists of representing the solution of an equation with an expansion in terms of simplified solutions and a coefficient. In the RP on γ, the general solution can be written as [6, 27]

$$A(t,z) = \sum_{k=0}^{\infty} \gamma^k A_k(t,z), \tag{6.14}$$

where the functions A_k are functions that depend on the initial field $A(\cdot, 0)$. In the first order RP on γ, equation (6.14) is truncated at $k = 1$, and the functions A_0 and A_1 are given in the next theorem. The result of Theorem 6.1 is well known in the literature (see [6, 7, 27]). However, we include its proof in the Appendix for consistency with the notation.

Theorem 6.1. Let A be the solution of the NLSE in equation (6.3) with initial condition $A(\cdot, 0)$. Then, A can be approximated by A_M, the first order RP on the nonlinear coefficient γ of equation (6.3), written as

$$A_M(t,z) = A_0(t,z) + \gamma A_1(t,z), \tag{6.15}$$

where

$$A_0(t,z) = \mathcal{D}_z\{A(\cdot,0)\}(t) \tag{6.16}$$

is the dispersion-only solution in equation (6.8) and

$$A_1(t,z) = j \int_0^z \mathrm{e}^{-\alpha u} \mathcal{D}_{z-u}\left\{|A_0(\cdot,u)|^2 A_0(\cdot,u)\right\}(t)\mathrm{d}u. \tag{6.17}$$

The proof is given in the Appendix.

Example 6.3. In Fig. 6.3c, the NSD results for SSMF and NZDSF fibres are presented. This figure shows that the NSD scales as 4 dB/dBm, which is twice as much as the value found for the dispersion-only model example (see Fig. 6.3a). This behaviour might be explained by the cubic signal power dependence of the nonlinear term and A_1 (see nonlinear term in equation (6.3)). Despite this faster growth of the NSD, the crossing point of the curves with the 0.1% threshold happens at higher powers compared with the dispersion-only case. This shows that the RP on γ model has a wider range of validity than the dispersion-only model. Figure 6.3c also shows that, for the RP on γ model, just like for the dispersion-only case, increasing $|\beta_2|$ slightly improves the NSD. The increase in the fibre length also deteriorates the performance of the RP on γ. As expected, the NSD grows when the power of the input signal is increased. To reduce the approximation error, more terms of the expansion in equation (6.14) can be considered. This comes at the cost of a higher model complexity, as done in [6].

6.2.4 Proposed model: regular perturbation on β_2

We now present the proposed model, which was derived based on the RP method to accurately represent the NLSE in the highly nonlinear regime, illustrated by region ④ in Fig. 6.1.

In analogy with the RP on γ, the RP method can be applied to β_2. The only difference is that now the expansion of A is written in terms of β_2 as

$$A(t,z) = \sum_{k=0}^{\infty} \beta_2^k A_k(t,z). \tag{6.18}$$

The terms A_0 and A_1 for the first order RP on β_2 are given in the next theorem, which is the main contribution of this paper.

Theorem 6.2. Let A be the solution of the NLSE in equation (6.3) with initial condition $A(\cdot,0)$. Then, A can be approximated by A_M, the first order RP on the linear coefficient β_2 of equation (6.3), written as

$$A_M(t,z) = A_0(t,z) + \beta_2 A_1(t,z), \tag{6.19}$$

where

$$A_0(t,z) = A(t,0)\mathrm{e}^{j\gamma|A(t,0)|^2 G(z)}, \tag{6.20}$$

and

$$A_1(t,z) = B(t,z)\mathrm{e}^{j\gamma|A(t,0)|^2 G(z)}, \tag{6.21}$$

with B given by

$$\begin{aligned} B(t,z) = &- M(t)z + G_1(z)R(t) + G_2(z)P(t) \\ &- 2j\gamma A(t,0)\Re\{A^*(t,0)V(t,z)\}, \end{aligned} \tag{6.22}$$

$$\begin{aligned} V(t,z) = &\, G(z)\left[M(t)z - G_1(z)R(t) - G_2(z)P(t)\right] \\ &- G_1(z)M(t) + G_2(z)R(t) + G_3(z)P(t), \end{aligned} \tag{6.23}$$

$$M(t) = \frac{j}{2}\frac{\partial^2 A(t,0)}{\partial t^2}, \tag{6.24}$$

$$R(t) = \frac{\gamma}{2}A(t,0)\frac{\partial^2 |A(t,0)|^2}{\partial t^2} + \gamma\frac{\partial A(t,0)}{\partial t}\frac{\partial |A(t,0)|^2}{\partial t}, \tag{6.25}$$

$$P(t) = \frac{j\gamma^2}{2}A(t,0)\left(\frac{\partial |A(t,0)|^2}{\partial t}\right)^2, \tag{6.26}$$

$$G_1(z) = \frac{\alpha z + \mathrm{e}^{-\alpha z} - 1}{\alpha^2}, \tag{6.27}$$

$$G_2(z) = \frac{2\alpha z + 4\mathrm{e}^{-\alpha z} - \mathrm{e}^{-2\alpha z} - 3}{2\alpha^3}, \tag{6.28}$$

$$G_3(z) = \frac{6\alpha z + 18\mathrm{e}^{-\alpha z} - 9\mathrm{e}^{-2\alpha z} + 2\mathrm{e}^{-3\alpha z} - 11}{6\alpha^4}. \tag{6.29}$$

The proof is postponed to the Appendix.

By comparing equation (6.19) and equation (6.20) with equation (6.12), it is clear that the RP on β_2 corresponds to the NLPN solution perturbed by the dispersion. The perturbation term A_1 in equation (6.21) is in closed form and it depends on the derivatives of the input field $A(\cdot,0)$. Note also that both A_1 and A_0 are multiplied by the same phase rotation, as shown in equation (6.20) and equation (6.21).

The functions A_0 and A_1 depend on elementary functions of z (see equations (6.13), (6.27), (6.28), and (6.29)). This results in the same calculation time for A_M at any distance z, in contrast to the SSFM, for which the number of necessary steps increases with the distance. For this reason, RP on β_2 calculations are significantly faster than SSFM calculations for the parameters simulated in this paper.

Example 6.4. Figure 6.3d presents the NSD for the RP on β_2 for the SSMF and the NZDSF. As shown in Fig. 6.3d, the NSD is approximately constant below a certain input power (0 dBm in this case). In addition, changes in the amount of dispersion severely impact the NSD. For example, at 0 dBm, increasing β_2 (going from NZDSF to SSMF) in the 80 km system, the NSD rises more than 2 orders of magnitude. This model is also very sensitive to the distance. Increasing the fibre length from 10 to 80 km in the SSMF system, the NSD rises more than 3 orders of magnitude for 0 dBm.

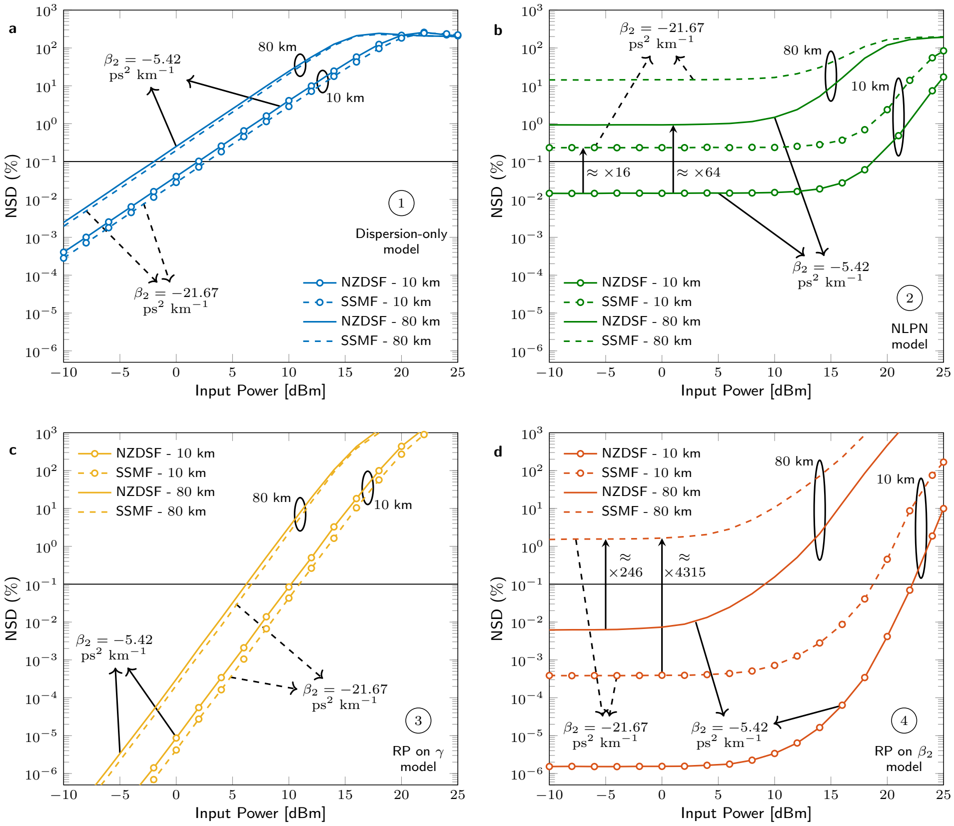

Figure 6.3: NSD for the four described models as a function of the input power. Two fibre lengths (10 and 80 km) and two types of fibre (NZDSF and SSMF). **a** Dispersion-only model given by (6.8). **b** NLPN model given by (6.12). **c** RP on γ model given by (6.15). **d** RP on β_2 model given by (6.19). Each model has a different accuracy, measured in NSD, for a specific set of input powers, β_2 coefficient, and distance. The black horizontal line represents a constant 0.1% NSD, which is used for comparison between models.

As discussed above, the RP on β_2 in equation (6.19) is the sum of the NLPN solution (A_0) and a term accounting for the dispersion ($\beta_2 A_1$). Therefore, some similarities in the NSD curves of these two models are expected (in analogy to the RP on γ and the dispersion-only model, discussed in Example 6.3). By comparing Fig. 6.3d with Fig. 6.3b, the RP on β_2 is an improved version of the NLPN model, just like the RP on γ is an improved version of the dispersion-only model.

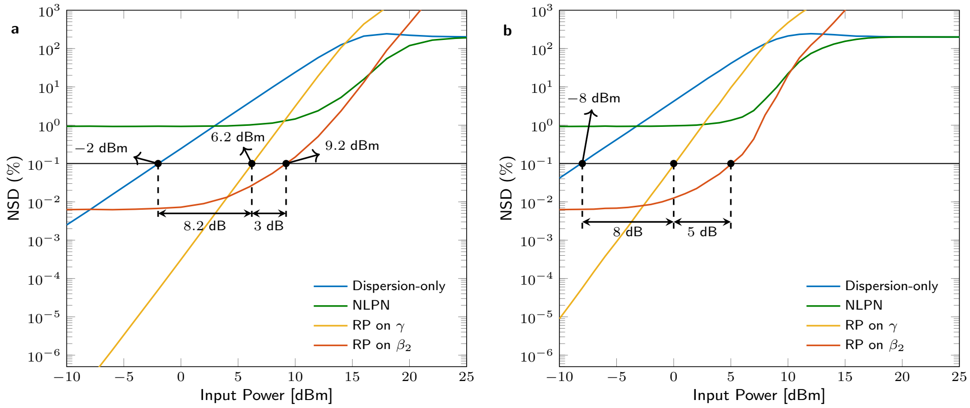

Figure 6.4: NSD for the four models in 80 km of an NZDSF. **a** With attenuation ($\alpha = 0.22$ dB km^{-1}). **b** Without attenuation ($\alpha = 0$ dB km^{-1}). The power gap in dB between the NSD curves is related to different input powers that allow each model to achieve 0.1% NSD. In the system without attenuation (**b**), this gap is increased when comparing RP on γ with RP on β_2.

Example 6.5. Figure 6.4a presents a comparison of the four models for an 80 km NZDSF. As shown in Fig. 6.4a, only the dispersion-only, the RP on γ, and the RP on β_2 models have NSDs below the threshold of 0.1% for some powers. The dispersion-only model crosses the threshold at -2 dBm, while the RP on γ crosses it at 6.2 dBm, presenting a gain of 8.2 dB. The RP on β_2 crosses the threshold at even higher powers (9.2 dBm), with a gain of 3 dB with respect to the RP on γ.

In systems with distributed Raman amplification, the power profile is approximately flat [76] and the attenuation term in (6.1) is often neglected. In this case, a simpler analytical form for $B(t, z)$ when compared to equation (6.22) is achieved. This simplification is given in the next theorem.

Theorem 6.3. With ideal distributed amplification, the functions A_0 and A_1 in equation (6.20) and equation (6.21) can be written as

$$A_0(t, z) = A(t, 0)\mathrm{e}^{j\gamma|A(t,0)|^2 z}, \tag{6.30}$$

$$A_1(t, z) = B(t, z)\mathrm{e}^{j\gamma|A(t,0)|^2 z}, \tag{6.31}$$

where

$$\begin{aligned} B(t, z) = &-M(t)z + \frac{z^2}{2}R(t) + \frac{z^3}{3}P(t) \\ &- 2j\gamma A(t, 0)\Re\left\{A^*(t, 0)\left[\frac{z^2}{2}M(t) - \frac{z^3}{6}R(t) - \frac{z^4}{12}P(t)\right]\right\}. \end{aligned} \tag{6.32}$$

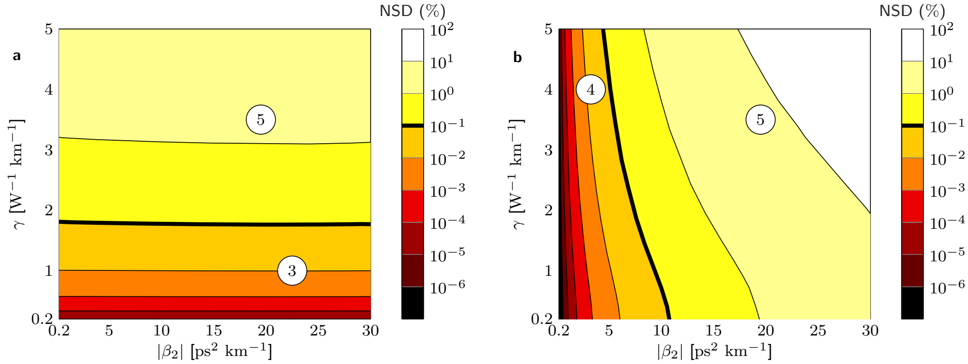

Figure 6.5: NSD for the RP on γ and the RP on β_2 for different values of $|\beta_2|$ and γ. The system consists of an 80 km fibre with fixed input power 5 dBm, symbol rate of 10 Gbaud, $\alpha = 0.2$ dB km^{-1}, and negative β_2. **a** Regular Perturbation on γ. **b** Regular Perturbation on β_2. Region ③ represents low γ and large $|\beta_2|$ values (see Fig. 6.1). Region ④ represents low $|\beta_2|$ and large γ values. Region ⑤ represents large γ and large $|\beta_2|$ values. The thick black line of constant 0.1% NSD is used as a threshold for accuracy comparison. The results indicate, as expected, that RP on γ is accurate for region ③ and RP on β_2 is accurate for region ④. Both models yield low accuracy in region ⑤.

and where $M(t)$, $R(t)$, and $P(t)$ are given by equation (6.24), equation (6.25), and equation (6.26), respectively.

The proof is postponed to the Appendix.

Example 6.6. Figure 6.4b shows the NSD for the four models with the same parameters as in Example 6.5, except that in this case there is no attenuation. For powers below -5 dBm, the NLPN model and the RP on β_2 present almost the same NSD compared with Fig. 6.4a. This behaviour could be justified by the small impact of the nonlinearities for low powers. The NSD values in that regime become close to each other, since the attenuation is mostly connected to the nonlinear effect (as can be seen in equation (6.3)). The curves cross the threshold at lower powers compared to Fig. 6.4a, excluding the NLPN model, which remains above the threshold for all analysed powers. We believe that the lower threshold crossing happens due to the additional interactions between nonlinearities and dispersion present in the lack of attenuation. While the RP on γ crosses the threshold at 0 dBm, the RP on β_2 crosses at 5 dBm, representing a gain of 5 dB (2 dB more compared to the attenuation case).

In the previous examples, the parameters γ and β_2 were fixed, along with the simulation bandwidth and the fibre length. These parameters are further investigated in the next examples, where the four models are compared with each other in systems with attenuation. For the next simulations, most of the parameters given in the previous examples are still consid-

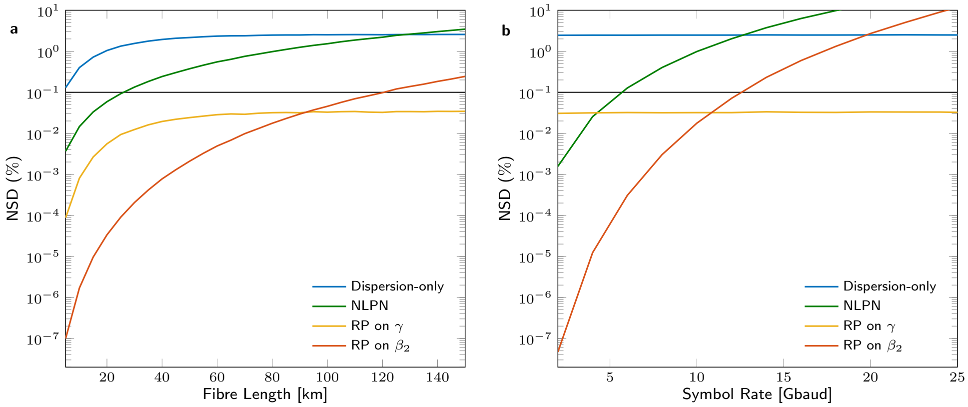

Figure 6.6: NSD versus fibre length and symbol rate for the four models. The system consists of an NZDSF with fixed input power 5 dBm. **a** NSD versus fibre length at a symbol rate of 10 Gbaud. **b** NSD versus symbol rate for a fibre length of 80 km. Changes in fibre length or symbol rate result in a wider range of NSD variation for RP on β_2 than for RP on γ.

ered; however, some of them will be changed. We will discuss fibre length variation, symbol rate variation, and β_2 and γ variation.

6.2.5 Variation of β_2 and γ

To analyse the impact of changes in β_2 and γ, we consider a fibre length of 80 km with fixed input power of 5 dBm, symbol rate of 10 Gbaud, and $\alpha = 0.2$ dB km^{-1}. In this analysis, only the RP on γ and β_2 will be considered. Figure 6.5a shows the NSD for the RP on γ for different values of $|\beta_2|$ (negative β_2) and γ. As depicted in Fig. 6.5a, variations in β_2 practically do not affect the accuracy of the model, while changes in γ have a major impact. In analogy with Fig. 6.1, the lower region of Fig. 6.5a is equivalent to region ③, where the model is accurate (NSD $< 0.1\%$). This region covers values of γ of up to approximately 1.78 W^{-1} km^{-1} for this system. Making the same analysis for RP on β_2 leads to Fig. 6.5b, which shows the NSD for the same range of γ and β_2 values. In this case, the area where the model is accurate is vertical, in analogy to region ④ in Fig. 6.1. The NSD for the RP on β_2 changes mostly with the value of β_2; however, changes in γ can also significantly affect the performance, specially for high $|\beta_2|$ values. The intersection of the areas that are not accurate for any of the models is related to region ⑤ in Fig. 6.1.

6.2.6 Fibre length variation

For the fibre length variation analysis, we consider an NZDSF with fixed input power of 5 dBm and a symbol rate of 10 Gbaud. Figure 6.6a shows the NSD versus fibre length for the four different models. All the four models increase the NSD when increasing the fibre length; however, the dispersion-only and the RP on γ seem to converge to a constant NSD value. This convergence is due to the attenuation on the nonlinear term in equation (6.3): for high distances, the nonlinearities do not considerably affect the signal, and the major effect is the dispersion. Since these two models fully predict the dispersion effect, they do not lose accuracy in that regime. The RP on β_2, for this system, can reach approximately 120 km within the NSD threshold of 0.1%, and for fibre lengths lower than 90 km, the model outperforms the RP on γ.

6.2.7 Symbol rate variation

For the symbol rate variation analysis, we consider 80 km of an NZDSF with fixed input power of 5 dBm. Figure 6.6b depicts the NSD variation with respect to the symbol rate. As shown in Fig. 6.6b, the dispersion-only model and the RP on γ do not change their accuracy when varying the symbol rate. On the other hand, the NLPN model and the RP on β_2 drastically drop the NSD when decreasing the symbol rate. For bandwidths lower than 4 Gbaud, even the NLPN can outperform the RP on γ. This behaviour may be justified by the decreasing influence of the dispersion on the signal, since according to equation (6.7), higher frequencies are more affected by dispersion due to their high second derivative.

6.2.8 Fibre length versus symbol rate

The previous two sections analysed the NSD by varying the fibre length and symbol rate separately. Both of these parameters influence the accumulated dispersion. Therefore, given a fibre length or a symbol rate, we can find the values for the other parameter in which RP on β_2 is accurate [15].

Figure 6.7 depicts the NSD given a fibre length and a symbol rate for an NZDSF with fixed input power 5 dBm. As shown in Fig. 6.7, the model can accurately handle arbitrarily large fibre lengths if the symbol rate is small enough and vice versa. By fixing a fibre length of 80 km, the maximum symbol rate in which RP on β_2 is still accurate is 12.55 Gbaud (see triangular marker in Fig. 6.7). If the distance is reduced to 20 km, the symbol rate can be increased until 27.38 Gbaud (see square marker in Fig. 6.7). These values show that by reducing the fibre length by a factor of 4, the symbol rate can be increased by a factor of approximately 2.18. This difference in scaling factors was already expected considering that the accumulated chromatic dispersion increases linearly with the distance and with the square of the signal bandwidth.

The thick solid line in Fig. 6.7 at an NSD of 0.1% can be seen as a conservative threshold. Choosing other metrics, such as signal-to-noise ratio (SNR), might motivate different

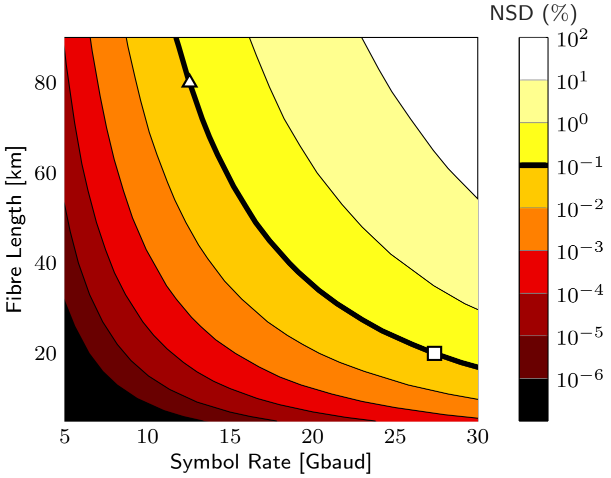

Figure 6.7: NSD for RP on β_2 for different values of fibre length and symbol rate. The system consists of a 80 km NZDSF with fixed input power 5 dBm. The triangular marker on the top of the figure is associated with the distance of 80 km and symbol rate of 12.55 Gbaud. The square marker on the bottom right is associated with the distance of 20 km and symbol rate of 27.38 Gbaud. Both markers lie on the thick black line representing a constant 0.1% NSD.

conclusions. For example, we will show in the discrete-time performance section (ahead), RP on β_2 can have an SNR close to that of the SSFM, even though RP on β_2 yields an NSD in the order of 30% in that scenario.

6.2.9 Modulation format impact

The previous simulations were based on 64-QAM. For different modulation formats, the transmitted signal statistics change. Since signal statistics impact the nonlinear effect, the NSD curves can be different for other modulation formats [15].

Figure 6.8 illustrates the NSD versus input power for three modulation formats on 80 km of an NZDSF with a symbol rate of 10 Gbaud. As shown in Fig 6.8, quadrature phase-shift keying (QPSK) yields lower NSD than the other two modulation formats. We believe this behaviour is justified by the QPSK's high tolerance to nonlinearities, which reduces the error in the first-order RP approximation. The performance of star 8-QAM and 64-QAM are almost the same for the considered input powers. The gap between QPSK and 64-QAM for the 0.1% threshold crossing is 0.8 dB for RP on β_2 and 1.1 dB for RP on γ. The higher gap for RP on γ might indicate that this model is more sensitive to changes in the modulation format than RP on β_2.

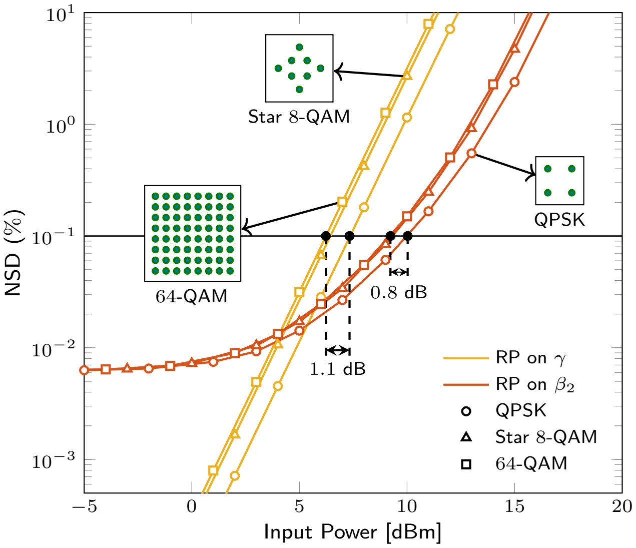

Figure 6.8: Impact of QPSK, star 8-QAM, and 64-QAM modulation formats on the NSD versus input power. The system consists of an 80 km NZDSF with 10 Gbaud symbol rate. The modulation format impact is measured by the power gap in dB between the crossing points of the NSD curves for each modulation format with the horizontal black curve representing a constant 0.1% NSD.

6.2.10 Discrete-time performance

As discussed in the 'Fibre propagation and metrics' section, the analysis of the received symbols might bring insightful conclusions about the models. In order to clearly visualize the fibre effects on the received constellations, the SNR simulations were based on QPSK modulation over a 20 km NZDSF. At the receiver, we considered two cases: with and without CDC, followed by matched filtering and sampling (see Fig. 6.2). We emphasize that these operations at the receiver are applied to the continuous-time output of the models and SSFM, and we are not using discrete-time analytical models.

Figure 6.9a shows the SNR for SSFM, RP on γ, and RP on β_2 at 10 Gbaud for both receivers. As depicted in Figure 6.9a, for input powers lower than 6 dBm, the SNR for the receiver with CDC is higher than the one without CDC. The latter converges to approximately 35.9 dB. This convergence could be explained by the uncompensated dispersion effect, which does not depend on the signal power (a linear effect). For input powers greater than 8 dBm, the systems with and without CDC are equivalent in SNR performance. This behaviour might be explained by the predominance of the nonlinear effect at these input powers. For input powers greater than 11 dBm, the SNR is higher for RP on γ than for SSFM and RP on β_2. In

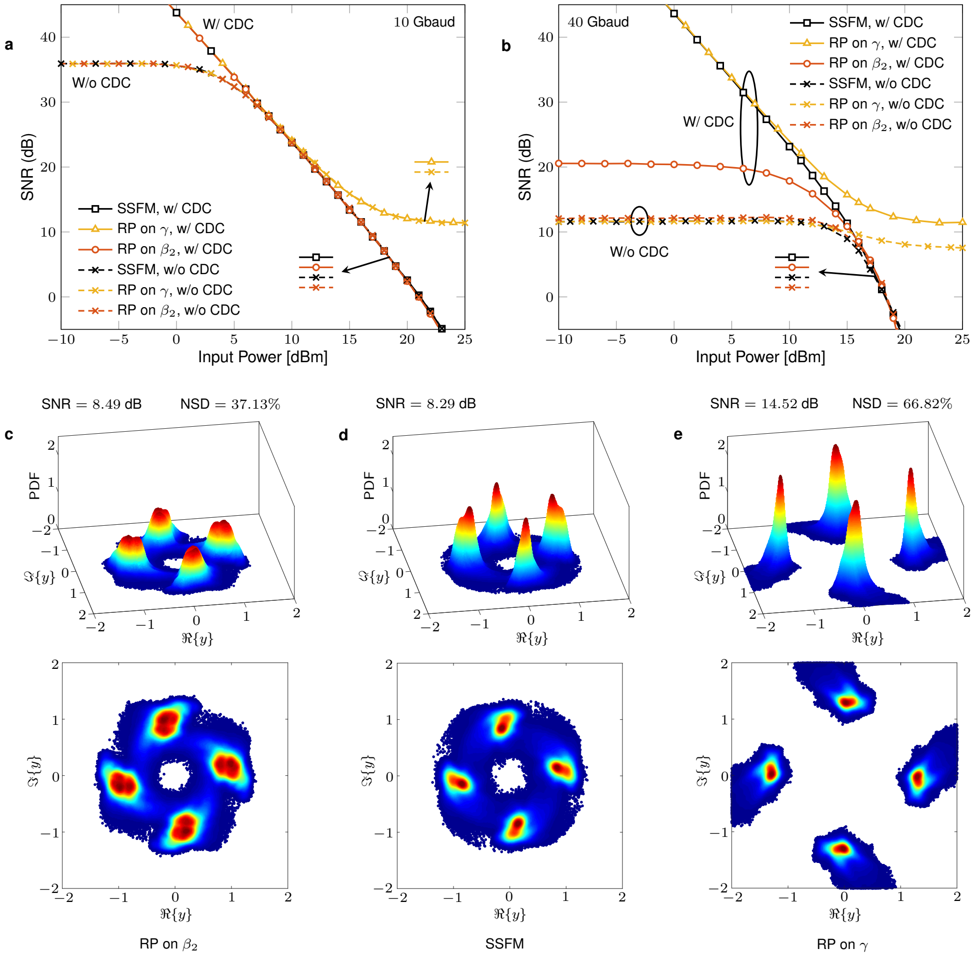

Figure 6.9: SNR versus input power for the symbol rates 10 and 40 Gbaud, and received constellations for SSFM, RP on γ, and RP on β_2, with their respective PDFs. On the SNR results, receivers with (w/) and without (w/o) CDC were considered for a QPSK modulation over a 20 km NZDSF. The constellations were obtained for 40 Gbaud with CDC at 16 dBm. **a** SNR results for the three models at a symbol rate of 10 Gbaud. **b** SNR results for the three models at 40 Gbaud. **c** Received RP on β_2 constellation and respective PDF. **d** Received SSFM constellation and respective PDF. **e** Received RP on γ constellation and respective PDF. The arrows pointing to the markers in **a** and **b** represent which curves are overlapped in those parts of the figure. In **c**, **d**, and **e**, the respective SNR values are shown on top of each of them. For **c** and **e**, the NSD values are also displayed.

this power regime, RP on β_2 can be seen as a more accurate model for SNR calculations.

Figure 6.9b illustrates the SNR for SSFM, RP on γ, and RP on β_2 at 40 Gbaud for both receivers. At this symbol rate and input powers lower than 15 dBm, RP on β_2 with CDC does not follow the SNR of SSFM and RP on γ. This difference might be related to the precarious estimation of the dispersion effect by the RP on β_2 for this higher bandwidth scenario (see Fig. 6.7). With a poor estimation of the chromatic dispersion, the CDC will not compensate the exact dispersion effect predicted by the RP on β_2 model. For the system without CDC, the performance of RP on β_2 is close to the SSFM performance for all displayed input powers. The SNR for RP on γ for systems with and without CDC diverges again from the SSFM performance at input powers higher than 11 and 16 dBm, respectively. Meanwhile, at input powers higher than 16 dBm, the performance of RP on β_2 for the CDC system approaches the SSFM performance.

For an input power of 16 dBm in the 40 Gbaud system with CDC, the received constellations for RP on β_2, SSFM, and RP on γ are shown in Figures 6.9c, 6.9d, and 6.9e, respectively, with their corresponding probability density functions (PDFs). As illustrated in these figures, the constellation for RP on β_2 approximately preserves the circular shape of the SSFM's constellation, which is not observed in the constellation for RP on γ. This preservation could be explained by the better prediction of nonlinear effects at this high input power by the RP on β_2. The received symbols for RP on γ are mostly outside the unitary square given by $|y| \leq 1$, which shows a high gain of energy when using this model. In addition, the PDF for RP on γ shows that its symbols are highly concentrated towards a single point, which was expected by its high SNR. Even though the SNR for RP on β_2 is close to the SNR of SSFM (8.49 and 8.29 dB, respectively), the received constellation shapes are slightly different. For example, as observed in the constellation PDFs, the RP on β_2 received symbols are more spread than the SSFM symbols. This contrast means that the SNR alone might not indicate precisely the accuracy of the model. On the other hand, a high NSD for RP on β_2 (37.13%) may not indicate that the received signal in discrete time is severely different from the reference given by the SSFM, showing that our proposed model is accurate in scenarios where nonlinearities are the dominant effect.

6.3 Discussion

This paper presented a new closed form analytical approximation for the solution of the NLSE: the regular perturbation on β_2. The derived approximation is a suitable model for low symbol rates, low fibre lengths, and/or high input powers. The regular perturbation on β_2 was compared with three other models with respect to variations in the bandwidth, fibre length, input power, and fibre parameters.

The main comparison was with the regular perturbation on γ, a well-known model in the literature that is accurate in the regime of high dispersion and low nonlinearities. In a nonzero dispersion-shifted fibre of 80 km with attenuation, the regular perturbation on β_2 can be used as an accurate model until input powers of 9 dBm, while the regular perturbation on γ is accurate only to input powers lower than 6 dBm. In addition, the regular perturbation on β_2 is accurate for high γ values where the regular perturbation on γ is not. Thus, the new proposed model is convenient for the opposite regime, where the nonlinearities are predominant, and the dispersion plays a minor effect.

As all simplified models, the proposed model has a limited range of validity. At the moment, the main applicability of the model is for applications that rely on low bandwidths (below 11 GHz) and short distances (below 80 km). This includes, for example, passive optical networks [77]. Another short-distance low-bandwidth application is hybrid fibre coax systems [78]. The model is in its present form not intended for long-haul or wavelength-division-multiplexed systems.

Another drawback of the proposed model is that it neglects the noise. This effect has been considered in the literature for the regular perturbation on γ in [27], where noise was added in the zeroth order linear equation, followed by a Karhunen–Loève expansion to account for nonlinear signal–noise interactions. The same approach for the regular perturbation on β_2 would lead to cumbersome equations, since the zeroth order equation is nonlinear in this case.

This paper represents the first steps in the theory of the proposed model. Possible extensions of this work are designing a receiver based on the regular perturbation on β_2, deriving higher-order perturbations of the model, and adding noise within the regular perturbation analysis. The derivations were conducted for a single-polarization system, and the equations for dual-polarization are still a subject of further investigation. Separating the contribution of individual pulses and finding a discrete model are also left as future work. Although the focus of this paper was on optical-fibre communications, we believe that our model can be applied to other fields where the nonlinear Schrödinger equation is applicable.

6.4 Methods

6.4.1 Simulation specifications

The simulations were conducted in Matlab® and considered 2^{15} symbols randomly chosen from different constellations during the paper. The constellations were generated with unitary energy. To generate the constellation figures and PDFs in Fig. 6.9c, 6.9d, and 6.9e, we used 2^{20} symbols for a smoother plot. The colour for each received symbol was attributed from a colormap according to the PDF values. The symbols were oversampled by 16 samples per symbol. After oversampling, the signal was shaped by an ideal RRC filter, with roll-off factor of 0.1, implemented in the frequency domain. After filtering, the signal was scaled to adjust to the desired input power. The resulting waveform was used as the input of either the SSFM or one of the models. For the SSFM case, we considered a symmetric SSFM implementation, with step-size 0.1 km. The step-size and the simulation bandwidth substantially impact the SSFM accuracy [39, 58]. Further reducing the step-size and increasing the simulated bandwidth by increasing the numbers of samples per symbol did not impact the displayed results, which indicates 0.1 km step-size and 16 samples per symbol are accurate enough for the systems in this paper. For the RP on γ model, the integral of equation (6.17) was evaluated numerically using an integration step of also 0.1 km. For the RP on β_2, the derivatives were obtained in the frequency domain. The dispersion operator was ideally implemented in the SSFM and in all simulated equations in the frequency domain. The chromatic dispersion compensation was implemented in the frequency domain with the dispersion operator applied with negative fibre length. Before the matched filter, the signal was scaled with the inverse scaling factor used in the transmission to adjust the input power. The matched filter was the same RRC filter as used in the transmission.

CHAPTER 7

Paper C: Logarithmic Perturbation Models in the Weak-Dispersion Regime with Applications to Passive Optical Networks

V. Oliari, E. Agrell and A. Alvarado, ”Logarithmic perturbation models in the weak-dispersion regime with applications to passive optical networks,” European Conference on Optical Communications (ECOC), Brussels, Belgium, Dec., 2020.
DOI: 10.1109/ECOC48923.2020.9333146,

Abstract

Three novel analytical models derived using logarithmic perturbation are presented. The best proposed model achieves a gain of 1.5 dB when comparing its normalised square deviation with other models in a passive optical network.

7.1 Introduction

Perturbation models have been proposed in the literature to approximate the optical fibre propagation, which is governed by the nonlinear Schrödinger equation (NLSE) [6, 7]. The NLSE can be described by attenuation, chromatic dispersion and the Kerr effect [1]. The Kerr effect is characterised by a nonlinear coefficient, while the chromatic dispersion by the group-velocity dispersion (GVD) parameter. Perturbative models based on the nonlinear coefficient have been widely used in the literature to predict system performance [27, 40] or design low-complexity receivers [5], for example. Recently, we proposed a perturbative model on the GVD parameter [15, 16].

The most studied perturbative methods in optical fibre communications are the regular perturbation (RP) and the logarithmic perturbation (LP) [7, 79]. RP has been presented in the literature for the nonlinear coefficient γ [6] and the GVD parameter β_2 [16], while LP has only been performed for γ [7, 80]. Therefore, in this paper, we present for the first time the LP on β_2 model. The performance of this model, however, can be improved by performing LP in the frequency domain, which is a new approach that we call frequency logarithmic perturbation (FLP). FLP should not be confused with the frequency resolved logarithmic perturbation (FRLP) proposed in [81, 82]. FRLP still applies the LP method in the time domain, whereas FLP applies this method in the frequency domain. To the best of our knowledge, this is the first time that FLP models are presented in the literature.

In total, six models arise from the mentioned perturbations. Three of them were already known in the literature: RP on γ, RP on β_2, and LP on γ. In this paper, we present three new other models: LP on β_2, FLP on γ, and FLP on β_2. We compare these six models in terms of normalised square deviation (NSD) in a passive optical network (PON). This system presents low accumulated dispersion due to its short distance, which makes it more suitable for perturbations on the GVD parameter. In addition, the system can operate in the highly nonlinear regime due to high input powers. The results show that FLP on β_2 yields the best performance in the highly nonlinear regime.

7.2 Channel Model and Performance Metric

The normalised NLSE for noiseless propagation of an optical field E for a retarded time frame t and distance z is [6]

$$\begin{aligned}\partial_z A(t,z) = &-(j\beta_2/2)\partial_{tt}A(t,z)\\ &+ j\gamma e^{-\alpha z}|A(t,z)|^2 A(t,z),\end{aligned} \tag{7.1}$$

where α is the attenuation coefficient. The first term on the right-hand side of (7.1) represents the chromatic dispersion and the last term represents the Kerr nonlinearity.

A numerically very accurate solution of (7.1) is obtained by the SSFM and denoted by A. We denote the output of a model M by A_M and compare it with A in the time domain. The metric used for this comparison is the NSD, defined as [6]

$$\text{NSD} \triangleq \frac{\int_{-\infty}^{\infty}|A_M(t,z) - A(t,z)|^2 dt}{\int_{-\infty}^{\infty}|A(t,z)|^2 dt}. \tag{7.2}$$

The NSD integrates the absolute error squared over the entire propagated time, and normalises it with the power of the signal A. The lower the NSD, the more accurate is the analytical model.

7.3 Regular Perturbation

The RP method consists of representing a signal by a power series of a certain coefficient. For the first order RP on γ, this series is truncated after the first two terms. The resulting first order RP on γ model is then given by

$$A(t,z) \approx A_{\text{RP}}^{(\gamma)}(t,z) = A_0^{(\gamma)}(t,z) + \gamma A_1^{(\gamma)}(t,z), \tag{7.3}$$

where $A_0^{(\gamma)}$ and $A_1^{(\gamma)}$ represent the zeroth and first order RP on γ terms [6, 7]. Analogously, the first order RP on β_2 is obtained by truncating the power series of the linear coefficient β_2 after the first two terms. The first order RP on β_2 is written as

$$A(t,z) \approx A_{\text{RP}}^{(\beta_2)}(t,z) = A_0^{(\beta_2)}(t,z) + \beta_2 A_1^{(\beta_2)}(t,z), \tag{7.4}$$

where $A_0^{(\beta_2)}$ and $A_1^{(\beta_2)}$ represent the zeroth and first order RP on β_2 terms [16].

7.4 Logarithmic Perturbation

LP is a mathematical technique similar to RP. LP on γ was first presented in [7, 80] and can be shown to have a higher convergence ratio than RP on γ. LP functions can be obtained

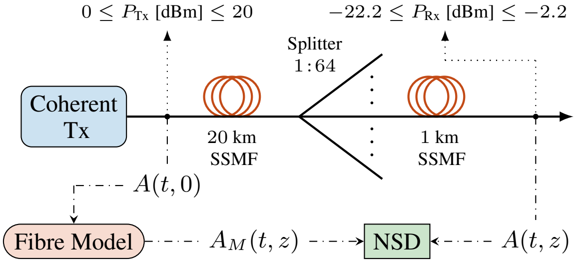

Figure 7.1: System setup based on PONs. Due to the short transmission distance, the system has low accumulated dispersion. The range of input powers allow the system to operate in a highly nonlinear regime.

directly by the RP functions $A_k^{(\gamma)}$ or $A_k^{(\beta_2)}$. Following an approach similar to [7], the first order LP on γ is written as

$$A_{\mathrm{LP}}^{(\gamma)}(t, z) = A_0^{(\gamma)}(t, z) \exp\left(\gamma \frac{A_1^{(\gamma)}(t, z)}{A_0^{(\gamma)}(t, z)}\right), \tag{7.5}$$

where the terms $A_0^{(\gamma)}$ and $A_1^{(\gamma)}$ are the RP terms in (7.3). Since the LP only depends on the RP terms, LP on β_2 can also be derived following the steps in [7], resulting in

$$A_{\mathrm{LP}}^{(\beta_2)}(t, z) = A_0^{(\beta_2)}(t, z) \exp\left(\beta_2 \frac{A_1^{(\beta_2)}(t, z)}{A_0^{(\beta_2)}(t, z)}\right), \tag{7.6}$$

where $A_0^{(\beta_2)}$ and $A_1^{(\beta_2)}$ are the RP terms in (7.4).

7.5 Frequency Logarithmic Perturbation

The linearity of (7.3) and (7.4) with respect to the functions $A_k^{(\gamma)}$ and $A_k^{(\beta_2)}$, respectively, suggests another approach to obtain a different LP solution. The new approach consists on performing the same steps on the LP derivation presented in [7] in the frequency domain, which we refer to as FLP. By using this approach, we can obtain two new models not yet presented in the literature, namely FLP on γ and FLP on β_2. The first order FLP on γ is given by

$$\tilde{A}_{\mathrm{FLP}}^{(\gamma)}(\omega, z) = \tilde{A}_0^{(\gamma)}(\omega, z) \exp\left(\gamma \frac{\tilde{A}_1^{(\gamma)}(\omega, z)}{\tilde{A}_0^{(\gamma)}(\omega, z)}\right), \tag{7.7}$$

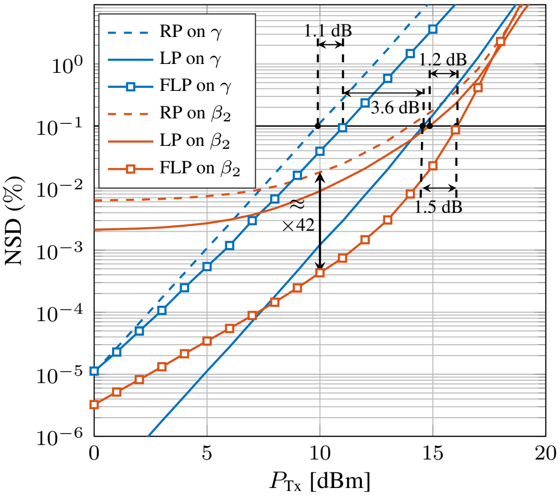

Figure 7.2: NSD versus input power P_{Tx} for the six analytical models presented in this paper. The transmission is performed in C-band. A schematic of the system is shown in Fig. 7.1.

where $\tilde{A}_0^{(\gamma)}$ and $\tilde{A}_1^{(\gamma)}$ are the Fourier transforms of $A_0^{(\gamma)}$ and $A_1^{(\gamma)}$ in (7.3), respectively. The first order FLP on β_2 is given by

$$\tilde{A}_{\text{FLP}}^{(\beta_2)}(\omega, z) = \tilde{A}_0^{(\beta_2)}(\omega, z) \exp\left(\beta_2 \frac{\tilde{A}_1^{(\beta_2)}(\omega, z)}{\tilde{A}_0^{(\beta_2)}(\omega, z)}\right), \tag{7.8}$$

where $\tilde{A}_0^{(\beta_2)}$ and $\tilde{A}_1^{(\beta_2)}$ are the Fourier transforms of $A_0^{(\beta_2)}$ and $A_1^{(\beta_2)}$ in (7.4), respectively.

7.6 Numerical Results

Fig. 7.1 shows the PON system setup under consideration. As depicted in the figure, we consider a standard single mode fibre (SSMF) of 20 km, followed by a splitter of ratio 1 : 64 and a final fibre segment of 1 km. With this split ratio, the power budget is 22.2 dB. The fibre input power P_{Tx} varies from 0 to 20 dBm, which leads to a received power P_{Rx} between -22.2 and -2.2 dBm. The range of powers was chosen to cover launch powers for PON systems according to [83, 84]. The SSFM has $\alpha = 0.2$ dB·km^{-1}, $\beta_2 = -21.67$ ps^{2}km^{-1}, $\gamma = 1.2$ W^{-1}km^{-1}, and operates at a wavelength of 1550 nm (C-band). The symbol rate for the single transmitted channel was 10 Gbaud and the modulation format quadrature phase shift keying (QPSK). The considered pulse shape was root-raised cosine (RRC), with a roll-off factor of 0.1. We do not specify any particular receiver, since the study compares the waveforms at the output of the fibre.

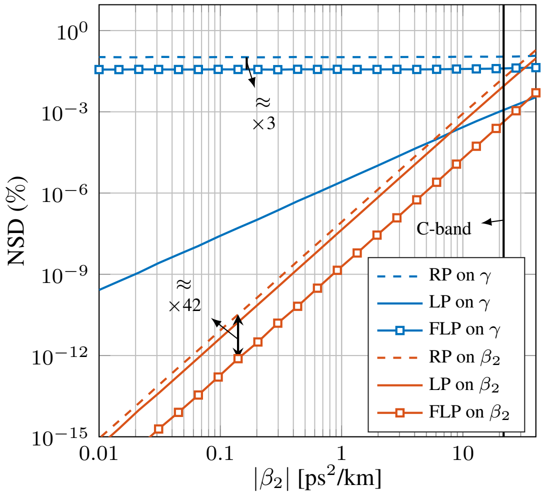

Figure 7.3: NSD versus $|\beta_2|$ for the six analytical models presented in this paper. The input power is fixed at 10 dBm for the system shown in Fig. 7.1 with negative β_2. The models present different rates of convergence when β_2 approachs to zero.

To evaluate the impact of the nonlinearities, the NSD was calculated for the powers in the highly nonlinear regime specified in Fig. 7.1. Fig. 7.2 shows the NSD versus P_{Tx} for the six analytical models analysed in this paper. As shown in Fig. 7.2, both LP and FLP on γ outperform RP on γ. The NSD of FLP on γ crosses the 0.1% NSD threshold at a P_{Tx} 1.1 dB higher than RP on γ. Analogously, both LP and FLP on β_2 outperform RP on β_2. These results support that, either in the time or in the frequency domain, an (F)LP approach converges faster to the true solution of (7.1) than the standard RP approach.

The results in Fig. 7.2 also show that LP on γ is more accurate than FLP on γ, while FLP on β_2 is more accurate than LP on β_2. For example, the NSD of LP on γ crosses the 0.1% NSD threshold at a P_{Tx} 3.6 dB higher than FLP on γ, while that of FLP on β_2 crosses the same threshold at a P_{Tx} 1.2 dB higher than LP on β_2. We believe that the difference between β_2 and γ when comparing LP and FLP could be explained by the solution of (7.1) for only the chromatic dispersion effect or only the Kerr effect [1]. The solution for the chromatic dispersion effect only is an exponential in the frequency domain, which resembles the FLP approach. Similarly, the solution for the Kerr effect only is an exponential in the time domain, which resembles the LP approach.

From the six models, FLP on β_2 is the one that presents best performance for P_{Tx} higher or equal 8 dBm. This result suggests that FLP on β_2 is more accurate for weak dispersion and high nonlinearity. For a constant NSD of 0.1 %, FLP on β_2 shows a gain of 1.5 dB in terms of input power when compared to LP on γ. Larger gains are observed at lower NSDs.

The effects of the dispersion on the models' performance was also investigated. When reducing the accumulated dispersion, the models LP on γ, RP on β_2, LP on β_2, and FLP on β_2 converge to the true solution of (7.1). This convergence can be analytically proved by letting $\beta_2 \to 0$ in (7.4), (7.5), (7.6), and (7.8). However, their rate of convergence is different. Fig. 7.3 shows the NSD versus $|\beta_2|$ for the six analysed models at $P_{\text{Tx}} = 10$ dBm and negative β_2. As depicted in Fig. 7.3, RP on β_2, LP on β_2, and FLP on β_2 present a rate of convergence higher than LP on γ. While the NSD of the three former models increases by approximately 10^4 per decade, that of NSD for LP on γ increases by only 10^2 per decade. The NSD for FLP on β_2 is approximately 42 times lower than for RP on β_2 (see also Fig. 7.2). This gain is kept approximately constant for other values of β_2. Only FLP on γ and RP on γ have approximately constant NSD over the shown range of β_2. The NSD for FLP on γ was roughly 3 times lower than the NSD for RP on γ.

7.7 Conclusions

Three novel models based on logarithmic perturbation theory were presented. The validity of the models was investigated in the C-band for a passive optical network. The frequency logarithmic perturbation on β_2 model demonstrated higher accuracy in the highly nonlinear regime than the other models analysed in the paper. Building a receiver based on the proposed model and finding higher order perturbations are possible extensions of this work.

CHAPTER 8

Paper D: Frequency Logarithmic Perturbation on the Group-Velocity Dispersion Parameter with Applications to Passive Optical Networks

V. Oliari, E. Agrell, G. Liga and A. Alvarado, “Frequency logarithmic perturbation on the group-velocity dispersion parameter with applications to passive optical networks,” in *Journal of Lightwave Technology*, vol. 39, no. 16, pp. 5287-5299, Aug., 2021.
DOI: 10.1109/JLT.2021.3101055,

Abstract

Signal propagation in an optical fiber can be described by the nonlinear Schrödinger equation (NLSE). The NLSE has no known closed-form solution when both dispersion and nonlinearities are considered simultaneously. In this paper, we present a novel integral-form approximate model for the nonlinear optical channel, with applications to passive optical networks. The proposed model is derived using logarithmic perturbation in the frequency domain on the group-velocity dispersion (GVD) parameter of the NLSE. The model can be seen as an improvement of the recently proposed regular perturbation (RP) on the GVD parameter. RP and logarithmic perturbation (LP) on the nonlinear coefficient have already been studied in the literature, and are hereby compared with RP on the GVD parameter and the proposed LP model. As an application of the model, we focus on passive optical networks. For a 20 km PON at 10 Gbaud, the proposed model improves the normalized square deviation by 1.5 dB with respect to LP on the nonlinear coefficient. For the same system, histogram-based detectors are developed using the received symbols from the models. The detector obtained from the proposed LP model reduces the uncoded bit-error-rate by up to 5.4 times at the same input power or reduces the input power by 0.4 dB at the same information rate compared to the detector obtained from LP on the nonlinear coefficient.

8.1 Introduction

ANALYTICAL models for optical fiber transmission have been widely studied in the literature. These models are based on the equations that govern the optical field propagation: the nonlinear Schrödinger equation (NLSE) [1, Ch. 2] and its variants. The NLSE has no known exact solution for an arbitrary input waveform. One of the most efficient alternatives for approximated numerical solutions is the split step Fourier method (SSFM) [58], which simulates the effects of fiber propagation. On the other hand, to analyse these effects and design novel transceivers, analytical models are highly desirable.

Some of the NLSE's most used analytical models are only valid under some restricted values of two fiber parameters: the (Kerr) nonlinear coefficient γ and the group-velocity dispersion (GVD) parameter β_2. The validity[1] of the models with respect to these parameters is shown in Fig. 8.1. When γ is equal to zero, the NLSE admits an analytical solution, given by the dispersion-only model [1, Ch. 3] and represented by the horizontal line at $\gamma = 0$ in Fig. 8.1. When β_2 is set to zero, the NLSE also admits an analytical solution, given by the nonlinear phase noise model (NLPN) [1, Ch. 4], [60], represented by the vertical line at $\beta_2 = 0$ in Fig. 8.1. If both parameters are nonzero, usually a perturbation approach is used [7].

A perturbation on the nonlinear coefficient γ considers the nonlinearities a minor effect [6, 7] and is accurate for high accumulated dispersion, where the accumulated dispersion can increase with the signal bandwidth and with the product of β_2 with the fiber length.

---

[1] The validity of a model is defined in this paper as the set of parameters values in which the model waveform is sufficiently close to the true waveform obtained from the NLSE. Details on the metric that measures the distance between the two waveforms are given in Sec. 8.3.

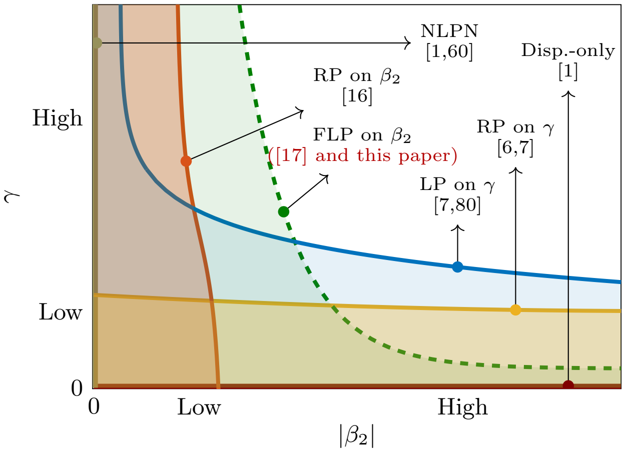

Figure 8.1: Illustration of the regions in the β_2 vs γ plane where different models are valid. This paper presents a new model for the region to the left of and under the green curve.

The development of a perturbation on γ, specifically the regular perturbation (RP) on γ, was an important mark in the literature since it has been used in many applications. For example, RP on γ is a key step in the derivation of the Gaussian noise [40] and enhanced Gaussian noise [41] models. These two latter models have been widely used to estimate system performance, even in the presence of effects such as stimulated Raman scattering [85]. RP on γ has also been used in the literature to build low-complexity receivers [5].

For the opposite regime, where the nonlinearities are the major effect and the accumulated dispersion is low but nonzero, a perturbation on the GVD parameter can be performed. The perturbation techniques usually considered for the optical fiber propagation are RP and logarithmic perturbation (LP) [7]. It was shown in [80] that LP converges faster to the true NLSE's solution than RP. RP and LP on γ cover the area under the yellow and blue curves in Fig. 8.1, respectively. Recently, we proposed RP on β_2 in [16] and compared with RP on γ. RP on β_2 provided more accuracy in the weakly dispersive and highly nonlinear regimes, represented by the area under the red curve in Fig. 8.1. A preliminary investigation of LP on β_2 was reported in our recent work [17], where LP methods on both γ and β_2 were compared on the waveform level. This paper is an extension of [17], to which we add two more contributions. Our first contribution is to derive the two perturbative models on β_2 presented in [17]. These models are obtained applying LP in either time or frequency. The latter approach, which we call frequency logarithmic perturbation (FLP), is the most accurate of the two for the β_2 expansion.

The FLP on β_2 covers the area under the green dashed curve in Fig. 8.1, which improves upon RP on β_2. FLP should not be confused with the frequency resolved logarithmic perturbation (FRLP) proposed in [81, 82, 86]. FRLP consists in applying LP on the frequency components of the time-domain signal individually and using the superposition principle to combine them. However, FRLP still applies the LP principle in the time domain, whereas FLP we study here applies this principle in the frequency domain. In this paper, the FLP on β_2 model is compared with the LP on γ, RP on γ, and RP on β_2 models.

The second contribution of this paper is to demonstrate the applicability of the proposed FLP on β_2 model. To this end, we consider passive optical networks (PONs), wherein the accumulated dispersion is typically low. PONs are usually short-reach fiber links where the transmitted signal is split to numerous users [87]. The input power can increase significantly when the split ratio is high, in order to compensate for the split loss [88, 89]. At a high input powers, the transmission can enter a highly-nonlinear regime, where even pre-distortion using digital backpropagation based on the SSFM has been proposed in the literature [90].

We use the models in a PON system to estimate optimum decision regions at the receiver. Simulations are carried out in the C- and O-band, where the latter has a close-to-zero GVD parameter β_2. At a waveform level (continuous-time), the proposed FLP on β_2 is shown to outperform the other three models at powers higher than 7 dBm for both C- and O-band systems. At a symbol level (discrete-time), decision regions obtained from LP on β_2 result in bit-error-rates (BER) more than five times lower than the ones obtained from LP on γ. Finally, these decision regions are analysed in a system with forward-error-correction (FEC).

This paper is organized as follows: Section 8.2 provides the mathematical background for the derivation of the models; Section 8.3 compares the models in both continuous- and discrete-time; and Section 8.4 concludes the paper.

8.2 Mathematical Background

The NLSE normalized by the attenuation factor for noiseless propagation of an optical field A at a retarded time frame t and distance z for a single-polarization can be approximated as [6]

$$\begin{aligned}\frac{\partial A(t,z)}{\partial z} = &-\frac{j\beta_2}{2}\frac{\partial^2 A(t,z)}{\partial t^2}\\ &+ j\gamma \mathrm{e}^{-\alpha z}|A(t,z)|^2 A(t,z),\end{aligned} \tag{8.1}$$

where α is the attenuation coefficient, β_2 the GVD parameter, and γ the nonlinear coefficient. The first term on the right-hand side of (8.1) represents the chromatic dispersion. This effect on the waveform A is larger when the bandwidth and/or the fiber length is increased. The last term represents the Kerr nonlinearity, which has a cubic dependence on the instantaneous signal power and also increases with the fiber length. The solution A of (8.1) can be numerically estimated by the SSFM [1, Ch. 2], [58]. Other effects, such as third-order dispersion (TOD) [1, Ch. 3], are not taken into account in (8.1). TOD becomes significant for large bandwidths or when β_2 is low. This effect will be taken into account for our simulations in the O-band, although it is not used in the derivation of the proposed model. For the C-band, we consider solely the effects in (8.1).

In what follows, we first review three models available in the literature. Sec. 8.2.1 and Sec. 8.2.2 describe the RP on γ and on β_2, respectively, while Sec. 8.2.3 presents the LP on γ. Finally, Sec. 8.2.4 introduces the FLP on β_2.

8.2.1 Regular Perturbation on the Nonlinear Coefficient

The RP on γ was first derived in [6, 7]. To approximate the solution of (8.1), the RP method represents the signal by a power series of a certain coefficient. For the RP on γ, the RP solution can be written as

$$A(t,z) = \sum_{k=0}^{\infty} \gamma^k A_k^{(\gamma)}(t,z). \tag{8.2}$$

To obtain the functions $A_k^{(\gamma)}$, (8.2) is substituted into (8.1) and the terms multiplied by the k-th power of γ are equated. An approximate solution for (8.1) can be obtained by considering only the functions $A_0^{(\gamma)}$ and $A_1^{(\gamma)}$. This approximation is the first-order RP on γ [6, Eqs. (7), (9)], [7, Eq. (12)]

$$A(t,z) \approx A_{\text{RP}}^{(\gamma)}(t,z) = A_0^{(\gamma)}(t,z) + \gamma A_1^{(\gamma)}(t,z), \tag{8.3}$$

where

$$A_0^{(\gamma)}(t,z) = \mathcal{D}_z\{A(\cdot,0)\}(t), \tag{8.4}$$

$$A_1^{(\gamma)}(t,z) = j\int_0^z \mathrm{e}^{-\alpha u}\mathcal{D}_{z-u}\left\{|A_0(\cdot,u)|^2 A_0(\cdot,u)\right\}(t)\mathrm{d}u, \tag{8.5}$$

and the dispersion operator $\mathcal{D}_z$ is

$$\mathcal{D}_z\{f\}(t) \triangleq (f * h(\cdot,z))(t), \tag{8.6}$$

$$h(t,z) = \frac{1}{\sqrt{j2\pi\beta_2 z}}\mathrm{e}^{-\frac{j}{2\beta_2 z}t^2}. \tag{8.7}$$

The function $A_0^{(\gamma)}$ in (8.4) is called the dispersion-only solution of (8.1). This solution can be seen as a model that is accurate only when the nonlinear effect is negligible. The first-order RP on γ in (8.3) is accurate for low nonlinear effects and is illustrated by the yellow curve in Fig. 8.1.

The RP on γ also benefits from a simple mathematical trick that yields an increased accuracy. This trick was developed in [6] and is based on modifying (8.1) by making

$$A(t,z) = A_P(t,z)e^{j\gamma P_0 G(z)}, \tag{8.8}$$

where $G(z) = (1 - \exp(-\alpha z))/\alpha$. Although P_0 was defined in [6] as the peak input power, we use P_0 as the average input power, which yields better accuracy in our simulations. After substituting (8.8) in (8.1), one can apply the RP on γ method over the function A_P instead of A and obtain the first order RP approximation for A_P. Multiplying the obtained approximation by $e^{j\gamma P_0 G(z)}$, as in (8.8), yields

$$\begin{aligned} A(t,z) &\approx A^{(\gamma)}_{\text{ERP}}(t,z) \\ &= \left[(1 - j\gamma P_0 G(z))A_0^{(\gamma)}(t,z) + \gamma A_1^{(\gamma)}(t,z)\right] e^{j\gamma P_0 G(z)}, \end{aligned} \tag{8.9}$$

where $A_0^{(\gamma)}$ and $A_1^{(\gamma)}$ are given by (8.4) and (8.5), respectively. Another benefit from RP on γ is that it can easily generate a solution that also accounts for TOD. This new solution is derived from (8.1) with an additional term accounting for TOD [1, Eq. (3.3.1)]

$$\begin{aligned} \frac{\partial A(t,z)}{\partial z} = &- \frac{j\beta_2}{2}\frac{\partial^2 A(t,z)}{\partial t^2} + \frac{\beta_3}{6}\frac{\partial^3 A(t,z)}{\partial t^3} \\ &+ j\gamma \mathrm{e}^{-\alpha z}|A(t,z)|^2 A(t,z). \end{aligned} \tag{8.10}$$

The RP on γ with TOD is then obtained by replacing the operator $\mathcal{D}_z$ in (8.4) and (8.5) by

$$\mathcal{T}_z\{f\}(t) \triangleq \mathcal{F}^{-1}\left\{\tilde{T}(\cdot,z)\cdot\tilde{f}\right\}(t), \tag{8.11}$$

$$\tilde{T}(\omega,z) = e^{\left(\frac{j\beta_2}{2}\omega^2 + \frac{j\beta_3}{6}\omega^3\right)z}, \tag{8.12}$$

where $\mathcal{F}^{-1}$ denotes the inverse Fourier transform[2], ω is the angular frequency, and $\tilde{f}$ is the Fourier transform of the function f.

8.2.2 Regular Perturbation on the GVD Parameter

We recently proposed the RP on β_2 in [16]. The same procedure as in (8.2) can be applied by considering A as a power series of β_2, i.e.,

$$A(t,z) = \sum_{k=0}^{\infty} \beta_2^k A_k^{(\beta_2)}(t,z). \tag{8.13}$$

In analogy to RP on γ, the functions $A_k^{(\beta_2)}$ are also obtained by replacing (8.13) in (8.1) and equating the terms related to the k-th power of β_2. For the first-order RP, involving the functions $A_0^{(\beta_2)}$ and $A_1^{(\beta_2)}$, an approximate solution for A can be obtained by

---

[2] We define the Fourier transform of a function $A(\cdot,z)$ as $\tilde{A}(\omega,z) \triangleq \int_{-\infty}^{\infty} A(t,z)\mathrm{e}^{+j\omega t}\mathrm{d}t$, which depends on the angular frequency ω and is evaluated at distance z. The inverse Fourier transform of $\tilde{A}(\cdot,z)$ is $A(t,z) = [1/(2\pi)]\int_{-\infty}^{\infty}\tilde{A}(\omega,z)\mathrm{e}^{-j\omega t}\mathrm{d}\omega$.

$$A(t,z) \approx A_{\mathrm{RP}}^{(\beta_2)}(t,z) = A_0^{(\beta_2)}(t,z) + \beta_2 A_1^{(\beta_2)}(t,z), \tag{8.14}$$

where

$$A_0^{(\beta_2)}(t,z) = A(t,0)\mathrm{e}^{j\gamma|A(t,0)|^2 G(z)}, \tag{8.15}$$

and

$$A_1^{(\beta_2)}(t,z) = B(t,z)\mathrm{e}^{j\gamma|A(t,0)|^2 G(z)}, \tag{8.16}$$

with B given by

$$\begin{aligned} B(t,z) &= -M(t)z + G_1(z)R(t) + G_2(z)P(t) \\ &\quad - 2j\gamma A(t,0)\Re\{A^*(t,0)V(t,z)\}, \qquad (8.17) \\ V(t,z) &= G(z)\left[M(t)z - G_1(z)R(t) - G_2(z)P(t)\right] \\ &\quad - G_1(z)M(t) + G_2(z)R(t) + G_3(z)P(t), \qquad (8.18) \\ M(t) &= \frac{j}{2}\frac{\partial^2 A(t,0)}{\partial t^2}, \qquad (8.19) \\ R(t) &= \frac{\gamma}{2}A(t,0)\frac{\partial^2|A(t,0)|^2}{\partial t^2} + \gamma\frac{\partial A(t,0)}{\partial t}\frac{\partial|A(t,0)|^2}{\partial t}, \qquad (8.20) \\ P(t) &= \frac{j\gamma^2}{2}A(t,0)\left(\frac{\partial|A(t,0)|^2}{\partial t}\right)^2, \qquad (8.21) \\ G_1(z) &= \frac{\alpha z + \mathrm{e}^{-\alpha z} - 1}{\alpha^2}, \qquad (8.22) \\ G_2(z) &= \frac{2\alpha z + 4\mathrm{e}^{-\alpha z} - \mathrm{e}^{-2\alpha z} - 3}{2\alpha^3}, \qquad (8.23) \\ G_3(z) &= \frac{6\alpha z + 18\mathrm{e}^{-\alpha z} - 9\mathrm{e}^{-2\alpha z} + 2\mathrm{e}^{-3\alpha z} - 11}{6\alpha^4}. \qquad (8.24) \end{aligned}$$

Analogously to RP on γ, the function $A_0^{(\beta_2)}$ in (8.15) for RP on β_2 is an accurate model when dispersion is negligible, and is called the NLPN model [16, 60]. The first-order RP on β_2 in (8.14) is accurate for low accumulated dispersion and is illustrated as the red curve in Fig. 8.1.

8.2.3 Logarithmic Perturbation

LP is a mathematical technique similar to RP. LP on γ was first presented in [7, 80] and can be shown to converge faster to the true NLSE's solution than RP on γ. LP functions can be obtained directly by the RP functions A_k. For example, following an approach similar to [7], consider that the signal A can be written as a power series of a coefficient θ (e.g., γ or β_2 as done in (8.2) and (8.13)) as

$$A(t,z) = \sum_{k=0}^{\infty} \theta^k A_k^{(\theta)}(t,z), \tag{8.25}$$

Table 8.1: Summary of the first-order perturbation methods discussed in this paper

Coeff. θ	Perturbation method					
	1st order RP $A(t,z)=A_0^{(\theta)}(t,z)+\theta A_1^{(\theta)}(t,z)$		1st order LP $A(t,z)=A_0^{(\theta)}(t,z)\exp\left(\theta\psi_1^{(\theta)}(t,z)\right)$		1st order FLP $\tilde{A}(\omega,z)=\tilde{A}_0^{(\theta)}(\omega,z)\exp\left(\theta\tilde{\zeta}_1^{(\theta)}(\omega,z)\right)$	
γ	$A_0^{(\gamma)}(t,z)$	$\mathcal{D}_z\{A(\cdot,0)\}(t)$	$\psi_1^{(\gamma)}(t,z)$	$\dfrac{A_1^{(\gamma)}(t,z)}{A_0^{(\gamma)}(t,z)}$	$\tilde{\zeta}_1^{(\gamma)}(\omega,z)$	$\dfrac{\tilde{A}_1^{(\gamma)}(\omega,z)}{\tilde{A}_0^{(\gamma)}(\omega,z)}$
	$A_1^{(\gamma)}(t,z)$	(8.5)				
β_2	$A_0^{(\beta_2)}(t,z)$	$A(t,0)\mathrm{e}^{j\gamma\lvert A(t,0)\rvert^2G(z)}$	$\psi_1^{(\beta_2)}(t,z)$	$\dfrac{A_1^{(\beta_2)}(t,z)}{A_0^{(\beta_2)}(t,z)}$	$\tilde{\zeta}_1^{(\beta_2)}(\omega,z)$	$\dfrac{\tilde{A}_1^{(\beta_2)}(\omega,z)}{\tilde{A}_0^{(\beta_2)}(\omega,z)}$
	$A_1^{(\beta_2)}(t,z)$	(8.16)				

where $A_k^{(\theta)}$ is the k-th RP function. We now want to express A in its LP version, which takes the form

$$A(t,z)=A_0^{(\theta)}(t,z)\exp\left(\sum_{k=1}^{\infty}\theta^k\psi_k^{(\theta)}(t,z)\right), \tag{8.26}$$

where the function $\psi_k^{(\theta)}$ is the k-th LP function and $A_0^{(\theta)}$ is the 0-th order RP function. Representing the exponential function in (8.26) by its Taylor expansion yields

$$A(t,z)=A_0^{(\theta)}(t,z)\sum_{m=0}^{\infty}\frac{1}{m!}\left(\sum_{k=1}^{\infty}\theta^k\psi_k^{(\theta)}(t,z)\right)^m. \tag{8.27}$$

The functions $\psi_k^{(\theta)}$ can now be obtained by equating (8.27) with (8.25), and further equating the terms that have the same power of θ. For example, equating the terms multiplied by θ^1, we obtain the first-order LP function as

$$\psi_1^{(\theta)}(t,z)=\frac{A_1^{(\theta)}(t,z)}{A_0^{(\theta)}(t,z)}. \tag{8.28}$$

Equating the terms multiplied by θ^2 we can also obtain the second-order LP function

$$\psi_2^{(\theta)}(t,z)=\frac{A_2^{(\theta)}(t,z)}{A_0^{(\theta)}(t,z)}-\frac{1}{2}\left(\frac{A_1^{(\theta)}(t,z)}{A_0^{(\theta)}(t,z)}\right)^2. \tag{8.29}$$

The function $\psi_2^{(\theta)}$ in (8.29) depends on the RP term $A_2^{(\theta)}$. For RP on γ, $A_2^{(\gamma)}$ is well defined [6, Eq. (11)], [7, Eq. (12)]. However, for RP on β_2, $A_2^{(\beta_2)}$ is not known in the literature at the time this paper is being written. Thus, we will restrict the analysis to first-order LP and RP only.

Setting $\theta=\gamma$ or $\theta=\beta_2$ in (8.26) and (8.28) and truncating the sum in (8.26) at $k=1$, we obtain the first-order LP on γ and on β_2, respectively. The first-order LP on γ is written as

$$A(t,z) \approx A_{\mathrm{LP}}^{(\gamma)}(t,z) = A_0^{(\gamma)}(t,z) \exp\left(\gamma \frac{A_1^{(\gamma)}(t,z)}{A_0^{(\gamma)}(t,z)}\right), \tag{8.30}$$

where $A_0^{(\gamma)}$ and $A_1^{(\gamma)}$ are given by (8.4) and (8.5), respectively. The accuracy of $A_{\mathrm{LP}}^{(\gamma)}$ is qualitatively illustrated by the blue curve in Fig. 8.1. The first-order LP on β_2 is similarly obtained as

$$A(t,z) \approx A_{\mathrm{LP}}^{(\beta_2)}(t,z) = A_0^{(\beta_2)}(t,z) \exp\left(\beta_2 \frac{A_1^{(\beta_2)}(t,z)}{A_0^{(\beta_2)}(t,z)}\right), \tag{8.31}$$

where $A_0^{(\beta_2)}$ and $A_1^{(\beta_2)}$ are given by (8.15) and (8.16), respectively.

8.2.4 Frequency Logarithmic Perturbation

The linearity of (8.25) with respect to the functions $A_k^{(\theta)}$ suggests another approach to obtain a different LP solution. The new approach consists of performing the same steps as in (8.25)–(8.28) in the frequency domain, which we refer to as FLP. To obtain the FLP solution, we first express (8.25) in the frequency domain, i.e.,

$$\tilde{A}(\omega,z) = \sum_{k=0}^{\infty} \theta^k \tilde{A}_k^{(\theta)}(\omega,z), \tag{8.32}$$

where $\tilde{A}$ represents the Fourier transform of A and ω is the angular frequency. Analogous to (8.26), now $\tilde{A}$ is expressed in its FLP version as

$$\tilde{A}(\omega,z) = \tilde{A}_0^{(\theta)}(\omega,z) \exp\left(\sum_{k=1}^{\infty} \theta^k \tilde{\zeta}_k^{(\theta)}(\omega,z)\right), \tag{8.33}$$

where the function $\tilde{\zeta}_k^{(\theta)}$ is the k-th FLP function and $\tilde{A}_0^{(\theta)}$ is the Fourier transform of the 0-th order RP function.

In complete analogy with the procedure used to obtain (8.28), the first-order FLP function is

$$\tilde{\zeta}_1^{(\theta)}(\omega,z) = \frac{\tilde{A}_1^{(\theta)}(\omega,z)}{\tilde{A}_0^{(\theta)}(\omega,z)}, \tag{8.34}$$

which is used to obtain the first-order FLP on γ and on β_2. The first-order FLP on γ is

$$\tilde{A}(\omega,z) \approx \tilde{A}_{\mathrm{FLP}}^{(\gamma)}(\omega,z) = \tilde{A}_0^{(\gamma)}(\omega,z) \exp\left(\gamma \frac{\tilde{A}_1^{(\gamma)}(\omega,z)}{\tilde{A}_0^{(\gamma)}(\omega,z)}\right), \tag{8.35}$$

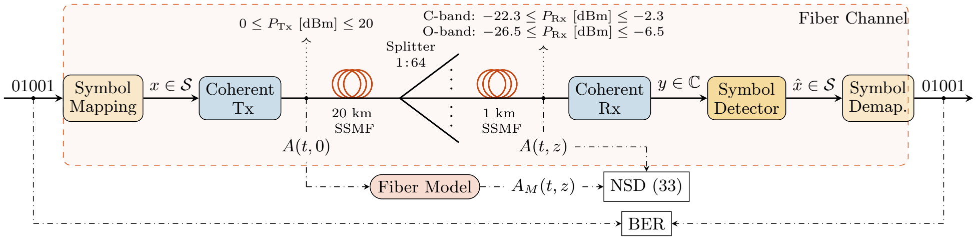

Figure 8.2: PON system setup used for the simulations in this paper. This system presents low accumulated dispersion and operates in the highly nonlinear regime for the used range of input powers. The NSD is calculated using the fiber output A, obtained via the SSFM, and a fiber model output A_M. The NSD exact formula given by (8.37). The BER is estimated using the bits corresponding to the input symbols x and the bits corresponding to the estimated input symbols $\hat{x}$, where $x, \hat{x} \in \mathcal{S}$ and $\mathcal{S}$ is the set of constellation points. Demap.: demapping.

where $\tilde{A}_0^{(\gamma)}$ and $\tilde{A}_1^{(\gamma)}$ are the Fourier transforms of (8.4) and (8.5), respectively. The first-order FLP on β_2 is given by

$$\tilde{A}(\omega, z) \approx \tilde{A}_{\mathrm{FLP}}^{(\beta_2)}(\omega, z) = \tilde{A}_0^{(\beta_2)}(\omega, z) \exp\left(\beta_2 \frac{\tilde{A}_1^{(\beta_2)}(\omega, z)}{\tilde{A}_0^{(\beta_2)}(\omega, z)}\right), \tag{8.36}$$

where $\tilde{A}_0^{(\beta_2)}$ and $\tilde{A}_1^{(\beta_2)}$ are the Fourier transforms of (8.15) and (8.16), respectively. The qualitative behaviour of the accuracy of $\tilde{A}_{\mathrm{FLP}}^{(\beta_2)}$ is illustrated as the green dashed curve in Fig. 8.1.

The functions $\tilde{\zeta}_k^{(\theta)}$ in (8.33) differ from the Fourier transform of $\psi_k^{(\theta)}$ in (8.26), since the exponential of the LP method was applied in the frequency domain. The expressions in (8.28) and (8.34) are the simplest example of this fact, since they do not form, in general, a Fourier transform pair. Therefore, we expect that these LP-based models result in a different accuracy for each perturbation coefficient (γ or β_2). As it will be seen later in Sec. 8.3, $A_{\mathrm{LP}}^{(\gamma)}$ is more accurate than $A_{\mathrm{FLP}}^{(\gamma)}$, while $A_{\mathrm{FLP}}^{(\beta_2)}$ is more accurate than $A_{\mathrm{LP}}^{(\beta_2)}$. We believe that the difference between β_2 and γ when comparing LP and FLP could be explained by the solution of (8.1) for only the chromatic dispersion effect or only the Kerr effect [1]. The solution for the chromatic dispersion effect only is an exponential in the frequency domain, which resembles the FLP approach. Similarly, the solution for the Kerr effect only is an exponential in the time domain, which resembles the LP approach.

Calculating the waveforms for both LP and FLP leads to a numerical issue related to the ratio in (8.28) and (8.34). When the denominator in one of those two equations tends to zero, the respective model becomes inaccurate. To address this problem in the LP case, [80] proposed to replace $A_{\mathrm{LP}}^{(\theta)}(t,z)$ by $A_{\mathrm{RP}}^{(\theta)}(t,z)$ whenever $|A_0(t,z)| < \epsilon$, where $\epsilon > 0$ is a fixed threshold. In our implementation, we chose to replace $A_{\mathrm{LP}}^{(\theta)}(t,z)$ by $A_{\mathrm{RP}}^{(\theta)}(t,z)$ whenever

Table 8.2: Fiber parameters for C- and O-band transmission

Parameter	C-band	O-band
Wavelength λ [nm]	1550	1310
α [dB/km]	0.2	0.4
β_2 [ps^2/km]	-21.67	-0.2
γ [1/W/km]	1.2	1.4
β_3 [ps^3/km]	–	0.0765

$|A_{\mathrm{LP}}^{(\theta)}(t,z)| > c\,|A_{\mathrm{RP}}^{(\theta)}(t,z)|$ for a certain fixed real $c > 0$. Similarly, we replace $\tilde{A}_{\mathrm{FLP}}^{(\theta)}(\omega,z)$ with $\tilde{A}_{\mathrm{RP}}^{(\theta)}(\omega,z)$ whenever $|\tilde{A}_{\mathrm{FLP}}^{(\theta)}(\omega,z)| > c|\tilde{A}_{\mathrm{RP}}^{(\theta)}(\omega,z)|$ or $|\tilde{A}_{\mathrm{FLP}}^{(\theta)}(\omega,z)| = 0$, where $\tilde{A}_{\mathrm{RP}}^{(\theta)}$ is the Fourier transform of $A_{\mathrm{RP}}^{(\theta)}$. The value of c for each model was heuristically found and is discussed in Sec. 8.3.4.

Together with the models in the previous sections, we obtained six perturbation models: two RPs in (8.3) and (8.14); two LPs in (8.30) and (8.31); and two FLPs in (8.35) and (8.36). Table 8.1 summarizes these six first-order perturbation methods. As shown in Table 8.1, LP and FLP can be obtained using the RP terms.

8.3 Simulation Setup and Results

The model presented in this work is validated in a PON transmission scenario where the accumulated dispersion is expected to be low. Fig. 8.2 shows the coherent PON system setup under consideration. The fiber parameters are given in Table 8.2. As depicted in the figure, we consider a standard single mode fiber (SSMF) of 20 km, followed by a splitter of ratio $1:64$ and a final fiber segment of 1 km. With this split ratio, the total link loss is 22.3 dB for the C-band and 26.5 dB for the O-band. The fiber input power P_{Tx} varies from 0 to 20 dBm, which leads to a received power P_{Rx} between -22.3 and -2.3 dBm in the C-band and between -26.5 and -6.5 dBm in the O-band. The range of powers was chosen to cover and go beyond launch powers for typical PON systems according to [83, 84]. All the results were obtained using randomly generated bits which were mapped into symbols drawn from a quadrature phase shift keying (QPSK) constellation $\mathcal{S} = (\pm 1 \pm j)/\sqrt{2}$. The coherent transmitter applies pulse shaping and scales the waveform such that the average transmitted power is P_{Tx}. The coherent receiver undo the waveform scaling, and then applies matched filtering and sampling, without chromatic-dispersion compensation. The symbol rate of the transmitted signal is 10 Gbaud for both C- and O-band systems. The considered pulse shape is a root-raised cosine (RRC), with a roll-off factor of 0.1. We consider a noiseless scenario since for the considered bandwidth and received powers, nonlinear distortions dominate over the shot noise [90, 91].

In the considered system setup, we want to evaluate the impact of nonlinearities and dispersion on the models. For evaluating the impact of the nonlinearities, the power was varied as specified before. The effect of the dispersion in the models is evaluated by comparing the C-band and the O-band scenarios, which have different β_2 values. We consider the effect of the TOD in the O-band since in that regime values of β_2 are low. Therefore, the equation used for the SSFM simulation in the presence of TOD is (8.10). In addition, our LP on γ results are also accounting for TOD by using (8.11).

We evaluate the model accuracy on two levels, comparing either the channel output waveforms or detected symbols. For the former, no receiver is considered. The accuracy is quantified using the normalized squared deviation (NSD) metric [6, 16]

$$\text{NSD} \triangleq \frac{\int_{-\infty}^{\infty} |A_M(t,z) - A(t,z)|^2 \mathrm{d}t}{\int_{-\infty}^{\infty} |A(t,z)|^2 \mathrm{d}t}, \tag{8.37}$$

where A_M is a model output (i.e., $A_{\text{LP}}^{(\gamma)}$ or $A_{\text{FLP}}^{(\beta_2)}$, for example) and A is the *true* fiber output obtained from the SSFM. The NSD integrates the absolute error squared over the entire signal duration, and normalizes it with the energy of the signal A. Therefore, the lower the NSD, the more accurate is the waveform predicted by the model. The inputs for the NSD calculation are illustrated in Fig. 8.2.

For the symbol-level evaluation, decision regions are optimized according to each model as described in Sec. 8.3.2. In that section, the accuracy is quantified in terms of BER (illustrated in Fig. 8.2), while in Sec. 8.3.3, the accuracy is quantified in terms of achievable information rate (AIR). Sec. 8.3.4 investigate numerical implementation aspects, such as time complexity and the choice of the threshold c.

8.3.1 Waveform Comparison

Fig. 8.3 shows the NSD for RP, LP, and FLP on γ and on β_2. As depicted in Fig. 8.3, FLP on β_2 (solid red line with squares) is the most accurate at powers higher than 7.5 dBm and NSD below 0.1%, while LP on γ (solid blue line) is the most accurate at powers lower than 7.5 dBm. FLP on γ (solid blue line with squares) and LP on β_2 (solid red line) have a slightly better performance than RP on γ (dashed blue line) and RP on β_2 (dashed red line), respectively. However, we do not consider FLP on γ and LP on β_2 further in this paper, since their performance is surpassed by LP on γ and FLP on β_2, respectively. RP on β_2 crosses the 0.1% NSD line at an input power approximately 4.2 dB higher than RP on γ, at 14 and 9.8 dBm, respectively. This gap in favor of RP on β_2 was expected since input powers greater than 10 dBm and small distances such as 20 km put the fiber in the highly nonlinear regime with low accumulated dispersion. The gap of 4.2 dB is reduced to 1.9 dB when comparing ERP on γ and RP on β_2. This reduction is justified by the change of variables made in (8.8), which improves the nonlinear tolerance of that model with respect to RP on γ. As discussed in [16], RP on β_2 is accurate on this regime, while RP on γ loses accuracy at high powers. If we change from RP on γ to LP on γ, the latter outperforms RP on β_2 for powers below

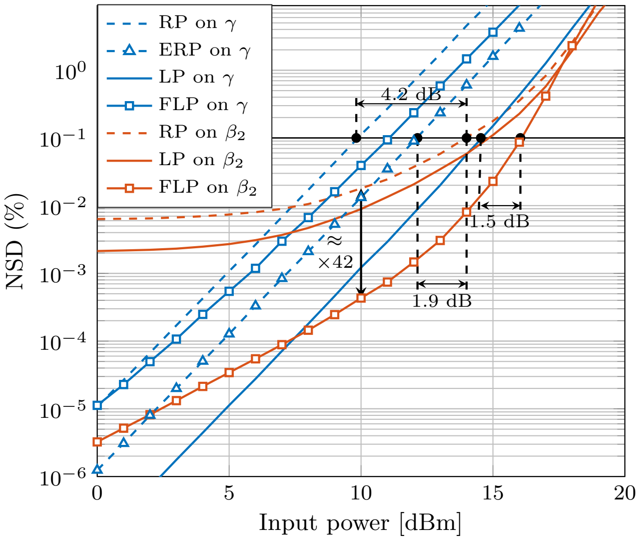

Figure 8.3: NSD for for RP, ERP, LP and FLP on γ and on β_2 in the C-band using the system in Fig. 8.2. The fiber parameters are given in Table 8.2.

16 dBm. This gain in accuracy by changing from the LP on γ to the RP on γ was previously shown in [80]. In addition, LP on γ has its performance increased due to low accumulated dispersion. By letting $\beta_2 \to 0$ in (8.30), LP on γ tends to the NLPN solution, which is accurate in very low dispersion scenarios [16].

The dependence of the models on $|\beta_2|$ can be seen in Fig. 8.4, where four models are compared at a fixed power of 10 dBm for different values of $|\beta_2|$ and the other parameters for C-band transmission (with no TOD). All the simulated β_2 values were negative. Among the four models, RP and ERP on γ are the only ones that are virtually invariant to changes in β_2 for $|\beta_2| < 30$ ps^2/km. Nevertheless, RP on γ has worse accuracy than LP on γ for all displayed values of β_2. When increasing $|\beta_2|$, LP on γ increases its NSD at a rate of approximately 10^2 per decade. Although LP on γ outperforms RP on β_2 at 10 dBm for the C-band, the latter has an increasing rate of approximately 10^4 per decade, and surpasses the accuracy of LP on γ for β_2 values lower than -6 ps^2/km. If we now also consider FLP on β_2, we can gain approximately 42 times in NSD accuracy with respect to RP on β_2 at 10 dBm. This gap can also be seen in Fig. 8.3 and remains approximately constant for different values of β_2, since both RP and FLP on β_2 have the same increasing rate of approximately 10^4 per decade. The higher increasing rate for RP and FLP on β_2 when compared with LP on γ shows that the two former models converge to the true solution of (8.1) faster than the latter model when decreasing the accumulated dispersion. For $\beta_2 = -21.67$ (C-band), FLP on β_2 already outperforms LP on γ. In addition, we see back in Fig. 8.3 that FLP on β_2 crosses the

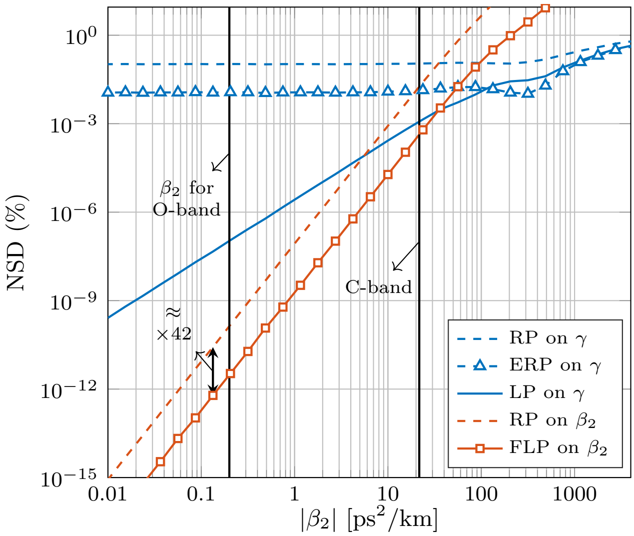

Figure 8.4: NSD versus $|\beta_2|$ (negative β_2) for five models at an input power of 10 dBm. The system is represented in Fig. 8.2. All considered models except RP on γ get higher accuracy as $|\beta_2|$ decreases.

line for an NSD of 0.1% at an input power 1.5 dB higher than LP on γ. For high values of $|\beta_2| > 30$ ps^2/km, the NSD for LP and for ERP on γ start to converge to a value closer to the NSD for RP on γ.

The results for LP on γ, RP on β_2, and FLP on β_2 using the O-band parameters in Table 8.2 are shown in Fig. 8.5, where the NSD is displayed as a function of the input power. First, we consider a system without TOD (dotted and dashed dotted lines). As shown in Fig. 8.5, the NSD for LP on γ and FLP on β_2 significantly decay when reducing the input power in the absence of TOD. On the other hand, RP on β_2 converges to an NSD of approximately $4.6 \cdot 10^{-11}\%$ for powers lower than 2 dBm. This convergence to a non-zero NSD value reflects the mismatch between (8.13) and (8.14) in the absence of nonlinearities. FLP on β_2 outperforms LP on γ for all the displayed input powers, while RP on β_2 outperforms LP on γ for input powers higher than 2.5 dBm. At 10 dBm, the difference in NSD between RP and FLP on β_2 is approximately 91 times, which is different from the 42 factor for the C-band results at the same input power (see Fig. 8.4). This discrepancy is due to the new set of γ and α values, which boost the difference between the two models at that input power.

The results for the O-band in Fig. 8.5 shows that when TOD is considered, RP and FLP on β_2 converge to a constant NSD of 10^{-9} for input powers lower than 3 dBm. This behavior can be explained by the absence of TOD in the model derivations. The error introduced by not accounting for TOD becomes approximately constant when input powers are lower than

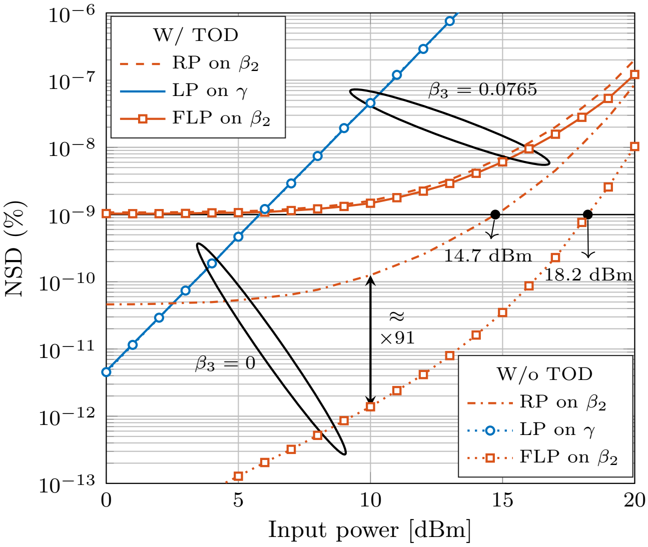

Figure 8.5: NSD for the four models in the O-band for the system in Fig. 8.2. Results without TOD are also shown.

3 dBm, and dominates the error introduced by incorrectly modeling the other fiber effects. From 0 to 20 dBm, the performance of RP and FLP on β_2 in the system with TOD is worse than without TOD. This behavior is expected, since for the system without TOD, RP and FLP on β_2 cross the constant NSD of 10^{-9} (TOD error floor for low powers) only at 14.7 dBm and 18.2 dBm, respectively. For LP on γ, the NSD for the system without TOD is virtually the same as for the system with TOD since we already account for TOD in the model derivation, as done in (8.11).

8.3.2 Decision Region Optimization

As discussed in [16], comparing models in discrete time can lead to slightly different conclusions than on a waveform level. For this reason, this section compares LP on γ, FLP on β_2, and SSFM results at the symbol level, measured by BER. The results are shown for the C-band system with parameters given in Table 8.2. To obtain the received symbols, the output waveform from these three models is filtered by a matched filter and sampled as done for the signal $A(\cdot, z)$ in Fig. 8.2. We do not include chromatic dispersion compensation (CDC) at the receiver due to the high amount of interaction between chromatic dispersion and nonlinearities which cannot be efficiently compensated by CDC. For example, the BER for this setup with a CDC block is virtually the same as the BER without CDC when using a minimum distance symbol detector. The resulting complex samples are used to optimize decision regions for each model, originating a symbol detector. Finally, SSFM simulations are performed to validate the accuracy of each symbol detector when receiving the *true* (SSFM) output waveform.

The decision region optimization for the symbol detector is based on the histogram of the received complex samples. This histogram-based (HB) detector follows the principle of choosing the most probable transmitted symbol, given that the corresponding received sample falls in certain area of the complex plane. This principle corresponds to the maximum a-posteriori (MAP) rule

$$\hat{x} = \operatorname*{argmax}_{s_m \in \mathcal{S}} \Pr\{X = s_m \mid Y = y\}. \tag{8.38}$$

where X and Y are random variables associated with the transmitted symbols and received samples (see Fig. 8.2), respectively, and $s_m \in \mathcal{S}$ where $\mathcal{S} = \{s_1, \cdots, s_M\}$ is the set of constellation points with cardinality M and $1 \leq m \leq M$. The MAP rule, as stated in (8.38), is optimal for a memoryless channel, and thus, suboptimal for the optical fiber channel, which includes memory.

To build the HB detector and numerically approximate the rule in (8.38), training symbols are transmitted through the fiber in order to obtain an estimation of the probability distribution. Their respective received samples will fall in a specific bin, which is an small area in the complex plane. For each bin, we count the number $n_{m,b}$ of received samples that fall inside the b-th bin and were drawn from the m-th constellation point, where $1 \leq b \leq B$, $1 \leq m \leq M$, and B is the total number of bins. The value of $m = \hat{m}_b$ that maximizes $n_{m,b}$ is considered to be the most probable transmitted constellation point for that bin. If $\max_m\{n_{m,b}\} = 0$, we replace b by the closest bin b' in Euclidean distance such that $\max_m\{n_{m,b'}\} > 0$, and decide $\hat{m}_b = \operatorname{argmax}_m\{n_{m,b'}\}$. After obtaining $\hat{m}_b$ for all possible b, the decision regions are defined and every time a received sample y is received in the b-th bin, we assume that received symbol $\hat{x} = s_{\hat{m}_b}$ was transmitted. For computational reasons, we only consider a subset $\mathcal{A} = \{z \in \mathbb{C} : |\Re\{z\}| < 2, |\Im\{z\}| < 2\}$ of the complex plane, divided into $B = 400 \times 400$ square bins of size 0.01. This region is sufficient to contain virtually all the received samples in the simulation. We simulate 2000 times the transmission of 2^{18} symbols, totalling approximately $5.2 \cdot 10^8$ symbols to obtain histograms that define $n_{m,b}$. Each sequence of 2^{18} symbols was randomly generated and the transmitted waveform had an oversampling factor of 16 samples per symbol. The decision regions were optimized for each transmitted power separately.

Fig. 8.6 depicts the decision regions obtained by using HB detectors for SSFM, FLP on β_2, and LP on γ at input powers $P_{\text{Tx}} \in \{15, 16, 17\}$ dBm. The transmitted constellation is illustrated with red crosses. Fig. 8.6 also includes contour plots of the histogram for the received samples when transmitting the constellation point $(1-j)/\sqrt{2}$. The decision regions associated to this constellation point are represented in yellow and contain most of the received samples shown by the contour plots. The samples that fall outside the yellow regions are not classified as $(1-j)/\sqrt{2}$ since there are more received samples originating from

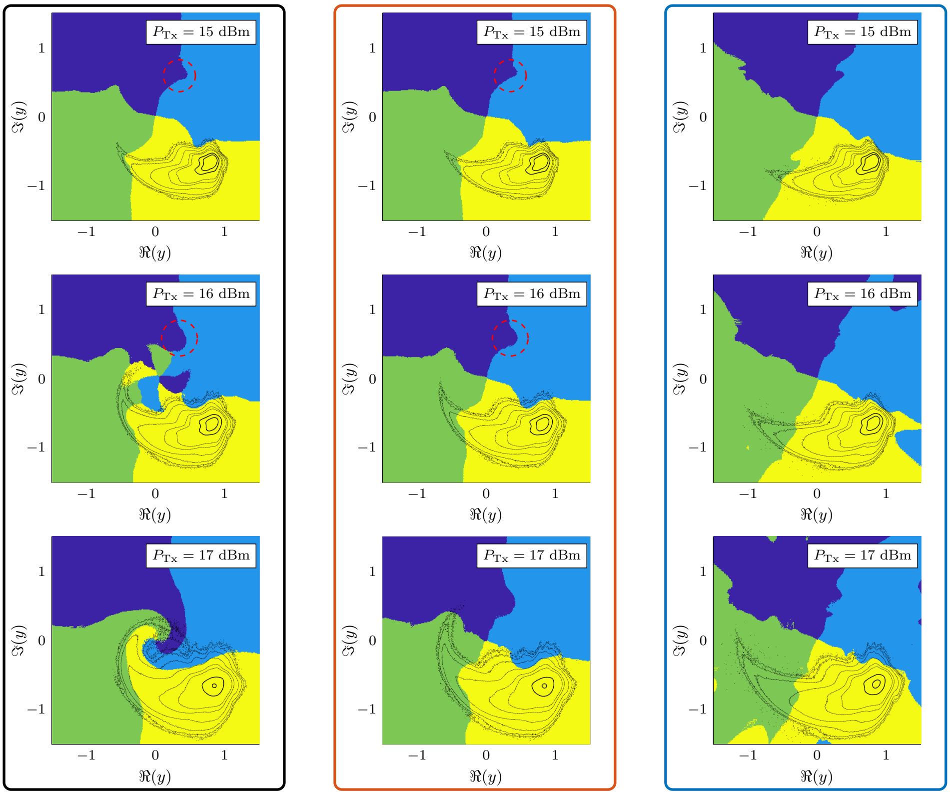

(a) SSFM. (b) FLP on β_2. (c) LP on γ.

Figure 8.6: Optimized decision regions obtained with HB detection after the propagation for $P_{\mathrm{Tx}} \in \{15, 16, 17\}$ dBm of a QPSK constellation based on: (a) SSFM; (b) FLP on β_2; (c) LP on γ. Each of the four differently colored areas represents the decision region for a specific constellation point. The respective constellation points are illustrated with red crosses. A contour plot of the histogram for the received samples for the transmitted symbol $(1-j)/\sqrt{2}$ is plotted on top of each subfigure.

another constellation point in those specific bins.

The optimum decision regions are considered as the ones obtained via SSFM in Fig. 8.6(a). At 15 dBm, the decision regions differ significantly from the four quadrants of the complex plane that represent the minimum distance decision regions. This difference originates from the nonlinearities, which creates a non-Gaussian distribution of the received samples. Due to the high nonlinear effect present at 17 dBm, the SSFM decision regions and the contour plots

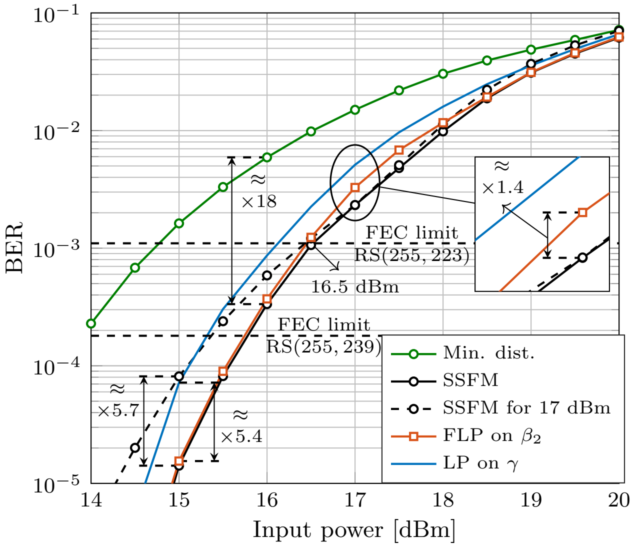

Figure 8.7: BER versus input power for receivers using HB detectors. The HB detectors were obtained via SSFM, LP on γ, and FLP on β_2. In all cases, the channel was simulated in the C-band using the SSFM. BER results for fixing the SSFM detector obtained for 17 dBm input power are also presented. Min. dist.: Minimum distance.

follow a spiral shape. The decision regions obtained by FLP on β_2 are shown in Fig. 8.6(b). At 15 dBm, these decision regions are similar to the SSFM ones for the same P_{Tx}. However, at 17 dBm, these regions do not present a spiral shape, as in Fig. 8.6(a). This new behavior can be explained by the contour plots. The curvature of the contour plots in Fig. 8.6(b) is lower than the curvature in Fig. 8.6(a), which results in the symbols from the tail of the contour plot falling in bins with a high number of points transmitted from another constellation point. The curvature for the contour plot of symbols obtained via LP on γ in Fig. 8.6(c) is even lower than for FLP on β_2 in Fig. 8.6(b). This fact results in decision regions with less accentuated curves in center of Fig. 8.6(c) for each P_{Tx}. At 15 dBm, the LP on γ decision regions already differ significantly from the SSFM ones. For example, at both 15 and 16 dBm, a small lobe (red dashed circle) present in both SSFM and FLP on β_2 decision regions is not present in the LP on γ ones. The shape of the contour plots indicate that the decision regions obtained with FLP on β_2 might perform closer to the SSFM decision regions than the ones obtained with LP on γ, as will be discussed next.

The HB detectors obtained using LP on γ, FLP on β_2, and SSFM are compared in a system whose fiber propagation is modeled by the SSFM. The results are shown in Fig. 8.7, where the BER is evaluated for different launch powers using the obtained HB detectors.

The latter are obtained using the SSFM for fiber propagation. The BER was estimated after averaging the results for 100 realizations of randomly generated sequences of 2^{17} symbols, totalling approximately $1.3 \cdot 10^7$ symbols. As shown in Fig. 8.7, the SSFM HB detector (black curve) shows the lowest BER for the displayed input powers. The minimum distance HB detector gives the worst performance since it assumes a Gaussian distribution of the received samples. This detector is obtained by minimum Euclidean distance from the received samples to the possible transmitted symbols. Replacing the minimum distance HB detector by the SSFM one at 16 dBm reduces the BER approximately 18 times (from $5.9 \cdot 10^{-3}$ to $3.3 \cdot 10^{-4}$). At 15 dBm, the BER for FLP on β_2 is 4.6 times lower than for LP on γ. As expected, results for FLP on β_2 are closer to the SSFM results than LP on γ. The highest gap between the SSFM and FLP on β_2 occurs at 17 dBm, where the BER for FLP on β_2 is 1.4 times higher than the BER for SSFM. The fact that a higher gap appears from 16.5 dBm could be related to the high NSD observed in Fig. 8.3 for FLP on β_2 at that range of input powers. Fig. 8.7 also shows the performance of the SSFM detector obtained at 17 dBm when used for other input powers. As the input power distance from 17 dBm increases, the performance of the SSFM detector for 17 dBm decreases with respect to the performance of other SSFM detectors obtained in those respective input powers. For example, at 15 dBm, the BER for the 17 dBm SSFM detector is 5.7 times higher than the 15 dBm SSFM one, matching the performance of LP on γ. Nevertheless, the BER of the 17 dBm SSFM detector is still lower than the BER for minimum distance detection.

8.3.3 Achievable Information Rates

FEC is present in modern PON systems to improve system performance [92]. In Fig. 8.7, pre-FEC BER thresholds are shown for two Reed-Solomon (RS) codes [93]. The considered codes in Fig. 8.7 are RS(n, k) with $k = 239, 223$ and $n = 255$, where k and n are the information and codeword lengths, resp. These two codes are typical low-complexity RS codes used in PONs [92, 94] and have a code rate of 0.93 and 0.87, respectively.

Along with RS codes, also stronger FEC codes such as low-density parity-check codes or staircase codes have been proposed for PONs in the literature [95–97]. In this section, we evaluate the models for PON systems with hard-decision (HD) FEC in terms of achievable information rates (AIRs) [35]. We consider the simple RS codes described above and a theoretical HD limit for the AIR. The latter is close to the performance of strong HD FEC codes [98, Fig. 8]. The AIRs are obtained by closed-form expressions based on pre-FEC BER.

We consider a family of RS codes RS(n, k) with multiple coding rates, where k is varied to obtain different code rates. We use a fixed codeword length ($n = 255$ symbols) in order to constrain the code complexity. For every launch power, k is determined by finding the highest k such that the post-FEC BER falls below a certain threshold. Following [83, Table

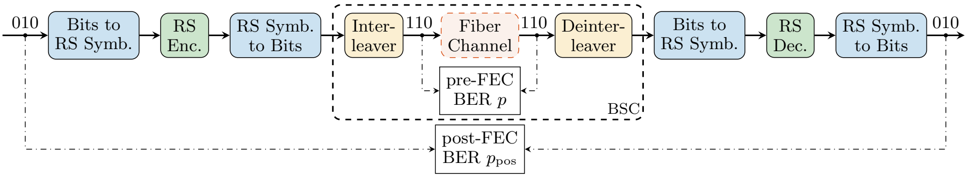

Figure 8.8: Encoding/decoding procedures used in this paper for RS codes. The fiber channel block include all components from Fig. 8.2. The post-FEC BER p_{pos} is estimated from the pre-FEC BER p using (8.39). Enc.: encoder; Dec.: decoder; Bsc:flp: binary symmetric channel.

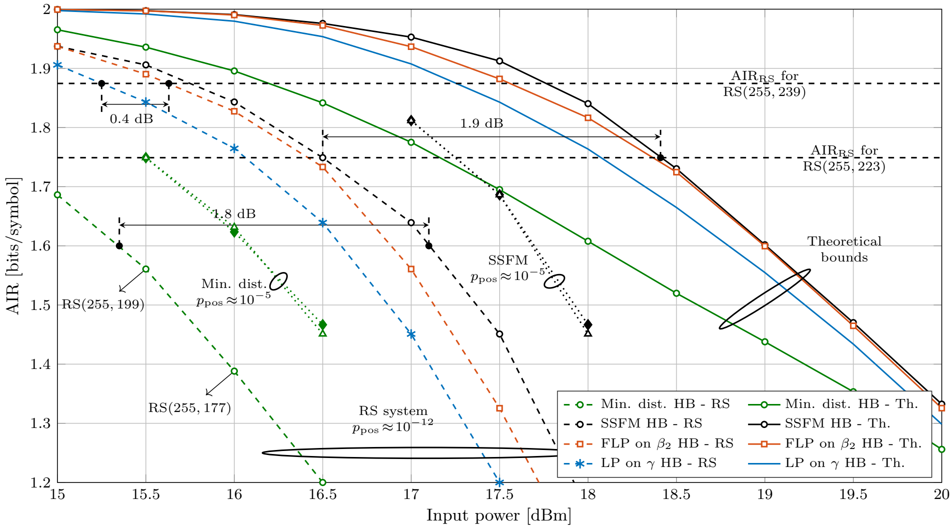

Figure 8.9: Comparison of AIRs when using the decision regions obtained in Sec. 8.3.2. The AIRs were obtained using (8.40) and (8.39) at $p_{\text{pos}} \approx 10^{-12}$ for the RS system and (8.41) for the theoretical bound. The dotted lines represent the comparison between AIR$_{\text{RS}}$ when approximating p_{pos} by (8.39) (white triangles) and AIR$_{\text{RS}}$ when simulating the system in Fig. 8.8 (filled diamonds), both for $p_{\text{pos}} \approx 10^{-5}$. Th.: theoretical.

IV.2], we use 10^{-12} as post-FEC BER threshold.

The post-FEC BER p_{pos} can be approximated by substituting the pre-FEC BER p from the system in Fig. 8.2 in the analytical expression for binary symmetric channels (BSCs) and bounded-distance decoders [99]

$$p_{\text{pos}} \approx \frac{1}{n}\sum_{r=t+1}^{n}\left(\frac{p}{p_s}r+\frac{1}{2(t-1)!}\right)\binom{n}{r}p_s^r(1-p_s)^{n-r}, \tag{8.39}$$

where $t = \lfloor (n-k)/2 \rfloor$ is the RS error-correction capability, $p_s = 1-(1-p)^m$ is the (RS) symbol error probability, and $m = \lceil \log_2(n+1) \rceil$ is the number of bits per symbol. To improve the total computation time, a binary search algorithm on k over all integers between 1 and 253 is performed. After finding k, the AIR for the RS system (AIR_{RS}) is determined by

$$\text{AIR}_{\text{RS}} = \log_2(M)\frac{k}{n} = \frac{2}{255}k, \tag{8.40}$$

since $M = 4$ for QPSK. We call (8.40) an achievable information rate since we assume that $p_{\text{pos}} < 10^{-12}$ can be considered virtually error-free for the system considered in this paper.

Since the expression in (8.39) is valid for BSCs, we need to modify the system in Fig. 8.2 to fulfill that property. The fiber channel in Fig. 8.2 presents memory due to the interaction of dispersion and nonlinearities. Therefore, in our simulations we included a bit interleaver and a bit deinterleaver so that the fiber channel in Fig. 8.2 is well-approximated by a BSC. The resulting system, together with the RS encoding and decoding blocks, can be seen in Fig. 8.8. The system in Fig. 8.8 was only simulated for $p_{\text{pos}} \approx 10^{-5}$ and was used to validate the results of (8.39). After this validation, (8.39) was used instead of simulating the system in Fig. 8.8.

Fig. 8.9 depicts the AIRs for the RS system using (8.39). Before analyzing the results for $p_{\text{pos}} \approx 10^{-12}$, we validate (8.39) at $p_{\text{pos}} \approx 10^{-5}$ to determine if the system in Fig. 8.8 can be well-approximated by a BSC. This validation is done assuming a minimum distance detector and is shown by the dotted lines in Fig. 8.9. The results for the RS simulations of the exact system in Fig. 8.8 at $p_{\text{pos}} \approx 10^{-5}$ are shown with diamonds. An almost perfect overlap with the results from (8.39) with the same p_{pos} (shown with triangles) is observed. The agreement between these curves suggest that the system in Fig. 8.8 can be approximated by a BSC. Therefore, from now on only (8.39) is used for the RS systems at $p_{\text{pos}} \approx 10^{-12}$.

We start by comparing the dashed lines in Fig. 8.9, which represent the AIR_{RS} results in (8.40). As shown in Fig. 8.9, using the decision regions obtained by SSFM in a RS system can provide a gain of approximately 1.8 dB for a rate of 1.6 bits/symbol in terms of nonlinear tolerance. The crossing point between the rate of $\text{RS}(255, 223)$ with AIR_{RS} for the SSFM decision regions is at 16.5 dBm, which closely matches with the crossing point with BER in Fig. 8.7. When comparing the models, the histogram-based detector obtained using FLP on β_2 outperforms the LP on γ one throughout the considered power range, analogously to Fig. 8.7. Specifically for $\text{RS}(255, 239)$, FLP on β_2 outperforms LP on γ by approximately 0.4 dB.

The AIR_{RS} is also compared with a theoretical bound on hard-decision bit-wise AIRs for independent, identically distributed bit errors. The theoretical AIR (AIR_{TH}) used in this paper is defined as [100]

$$\mathrm{AIR}_{\mathrm{TH}} = \log_2(M)\,(1 - \mathrm{H_b}(p))\,, \tag{8.41}$$

where $\mathrm{H_b}(p) = -p\log_2(p) - (1-p)\log_2(1-p)$ is the binary entropy function for the given pre-FEC BER p in the system of Fig. 8.2. The $\mathrm{AIR}_{\mathrm{TH}}$ from (8.41) can be approached by strong FEC codes such as staircase codes, as reported in [98, Fig. 8].

As shown in Fig. 8.9, the theoretical bounds (solid lines) from (8.41) show significant gains over the $\mathrm{AIR}_{\mathrm{RS}}$ results. These gains show that, by using codes more complex than $\mathrm{RS}(255, k)$, higher code rates can be achieved or the input power can be improved for a specific rate. For the same code rate as in $\mathrm{RS}(255, 223)$, the input power for the theoretical bound on the SSFM decision regions is approximately 1.9 dB higher than the one for the RS system. However, the complexity and latency of codes that perform close to the theoretical bound should be carefully analysed for a PON system design. The results for the theoretical bounds in in Fig. 8.9 also show that the histogram-based detector based on the FLP on β_2 outperforms the one based on LP on γ.

8.3.4 Numerical Analysis

As mentioned in Sec. 8.2.4, LP on γ and FLP on β_2 suffer from a numerical issue related to the ratio between the first and zeroth RP order. In this section, this issue is further investigated, more details on the models' implementation are presented, and the time–complexity tradeoff is discussed.

The time derivatives present in the β_2 perturbation models were calculated in the frequency domain by using fast Fourier transforms. Once the terms $A_0^{(\beta_2)}$ and $A_1^{(\beta_2)}$ were obtained, they were used to build both RP and FLP on β_2 models to avoid the recalculation of those terms for FLP. This last trick was analogously done for RP and LP on γ. To obtain the models RP and LP on γ, the integral in (8.5) was calculated using Gauss–Legendre quadrature [101, Ch. 5], [102]. The minimum number of necessary quadrature points to achieve the NSDs displayed for the C-band was only 2, while for the O-band this number increased to 4. The weights for the Gauss–Legendre quadrature were obtained from a look-up table. The SSFM calculations previously presented in the paper were performed using uniform (constant) spacial step sizes of 0.1 km. However, for the time complexity comparison in this section, we used logarithmic step sizes to increase the accuracy for a given number of steps [39]. A multiplicative correction factor of 0.6 was used to adjust α in the logarithmic step size calculation. This correction factor changes the distribution of the step sizes in order to improve the few-steps SSFM NSD. The simulations were performed on a NVIDIA® Tesla®-P100 GPU and the code written in MATLAB®. The code used for the models can be found in [103]. The simulation setup in this section differs slightly from the one considered in Sec. 8.3.1. We consider C-band simulations at a fixed 10 dBm input power. The splitter and the additional 1 km fiber are ignored in order to measure the time and accuracy of a single fiber segment for each method.

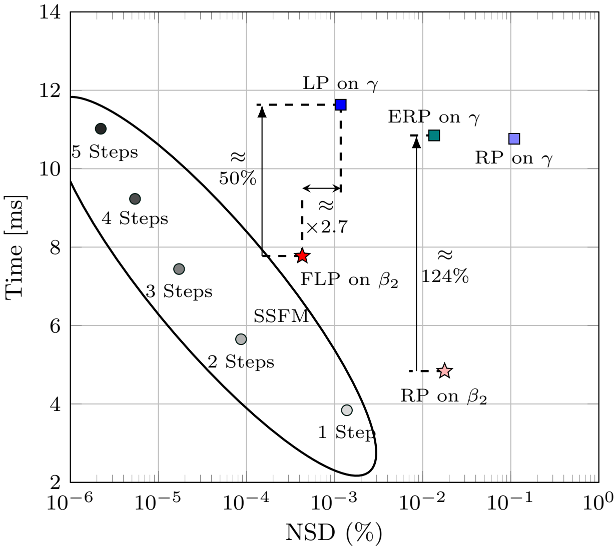

Figure 8.10: Average simulation time for most of the models considered in this paper. The simulated system is a 20 km fiber in C-band with input power 10 dBm. The code used to generate the models can be found on [103]. Few-steps SSFM simulations are also added to the figure (circles).

Fig. 8.10 shows the simulation time versus NSD for most of the models considered on this paper. The NSD values were averaged over 100 simulations, while the simulation time was averaged over 3000 realizations of the MATLAB® function *gputimeit*© for each model. In each simulation, 2^{17} symbols were transmitted, with an oversampling factor of 16. Random symbol sequences were generated when obtaining each NSD sample, while the input waveform for the simulation time measurements was fixed for all models. The NSD for the models and for SSFM simulations with a small number of spatial steps was calculated using as the reference waveform SSFM simulations with 70 logarithmically spaced steps. These steps were calculated using the symmetrized SSFM approach [1], where the nonlinear effect is included in the middle of each step. The few-steps SSFM simulations also used symmetrized logarithmically spaced steps. As depicted in Fig. 8.10, 2 symmetric steps SSFM simulations already yield higher accuracy in lower simulation time than all the other models in that figure for this system, except for RP on β_2 which has a slightly lower simulation time. Therefore, one might prefer using few-steps SSFM for numerical simulations instead of analytical models for this system.

However, our motivation for developing new integral-form models is to focus on better understanding fiber propagation instead of numerical aspects. Analogously to RP on γ, we

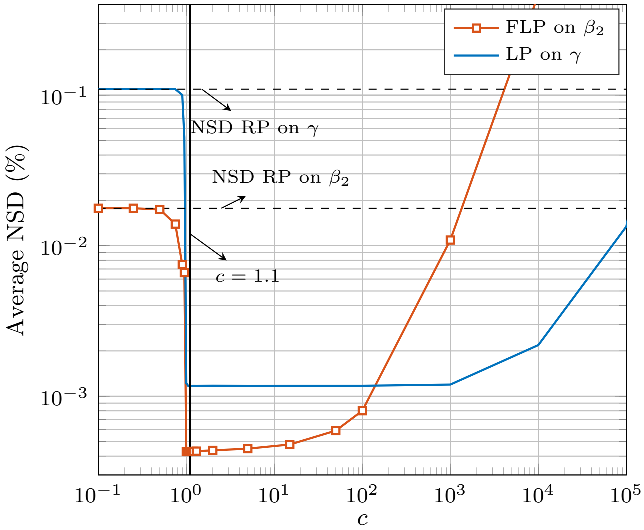

Figure 8.11: Average NSD versus threshold c over 500 simulations for LP on γ and FLP on β_2. For $c = 1.1$, the average NSD is approximately the minimum for both models.

believe that the β_2 perturbation models could also be used to build low-complexity receivers and performance prediction formulas. When comparing analytical models, Fig. 8.10 shows that changing from RP to ERP on γ requires virtually no increase in time, while yielding a lower NSD. The NSD of ERP on γ is comparable to the NSD of RP on β_2 at that input power. Nevertheless, ERP on γ requires approximately 124% more simulation time than RP on β_2. The gap in time between RP and FLP on β_2 is higher than the gap between RP and LP on γ. This difference might be explained by the additional fast Fourier transforms required in the FLP method and by the additional search $\tilde{A}_0^{(\beta_2)}(\omega, z) = 0$, as stated in Sec. 8.2.4. Although having a lower gap from RP on γ, the simulation time for LP on γ is 50% higher than for FLP on β_2. In addition, FLP on β_2 presents approximately 2.7 times lower NSD than LP on γ.

The choice of the threshold c used for both LP and FLP methods is also investigated. Fig. 8.11 illustrates the average NSD versus c over 500 simulations. As shown in Fig. 8.11, for $c < 0.02$, the NSD of LP on γ and FLP on β_2 converge to the NSD of their respective RP models. For $c > 10$, the NSD of FLP on β_2 starts to increase significantly. This increase is due to high energy isolated points where the value of the zeroth order perturbation term is significantly smaller than the first order one. The lower the value of c, the more these isolated points are filtered. The same behavior happens for LP on γ for $c > 10^3$. At $c = 1.1$, the NSD is virtually the minimum for both models and was the chosen threshold for simulations.

8.4 Conclusions

In this paper we presented a novel model for optical fiber transmission and evaluated its performance for a passive optical network system. The proposed model was derived as an improved version of the regular perturbation on the GVD parameter model. The improvement was obtained by applying frequency logarithmic perturbation on the GVD parameter. Both regular and frequency logarithmic perturbation on the GVD parameter models are suitable in the weakly dispersive and highly nonlinear regime, whereas the frequency logarithmic perturbation is able to surpass the limitations of the regular perturbation.

Apart from the regular perturbation on the GVD parameter, the proposed model was compared with two other models present in the literature: regular and logarithmic perturbation on the Kerr nonlinear coefficient. For a fixed normalized squared deviation of 0.1%, the proposed model was accurate at 1.5 dB higher input powers compared to logarithmic perturbation on the Kerr nonlinear coefficient. Both frequency logarithmic and regular perturbation on the GVD parameter exhibit the highest convergence rate to the split-step Fourier method results when reducing the dispersion effect. The proposed model also proved to be more suitable for symbol and bit detection, with and without FEC.

Possible extensions of this work are higher-order logarithmic perturbation models, perturbation on the GVD parameter for dual-polarization systems, and nonlinearity-compensation techniques based on the proposed model.

CHAPTER 9

Paper E: Revisiting Efficient Multi-Step Nonlinearity Compensation with Machine Learning: An Experimental Demonstration

V. Oliari et al., “Revisiting efficient multi-step nonlinearity compensation with machine learning: an experimental demonstration,” in *Journal of Lightwave Technology*, vol. 38, no. 12, pp. 3114-3124, June, 2020.
DOI: 10.1109/JLT.2020.2994220, *Copyright © 2020, IEEE.*

Abstract

Efficient nonlinearity compensation in fiber-optic communication systems is considered a key element to go beyond the “capacity crunch”. One guiding principle for previous work on the design of *practical* nonlinearity compensation schemes is that fewer steps lead to better systems. In this paper, we challenge this assumption and show how to carefully design multi-step approaches that provide better performance–complexity trade-offs than their few-step counterparts. We consider the recently proposed learned digital backpropagation (LDBP) approach, where the linear steps in the split-step method are re-interpreted as general linear functions, similar to the weight matrices in a deep neural network. Our main contribution lies in an experimental demonstration of this approach for a 25 Gbaud single-channel optical transmission system. It is shown how LDBP can be integrated into a coherent receiver DSP chain and successfully trained in the presence of various hardware impairments. Our results show that LDBP with limited complexity can achieve better performance than standard DBP by using very short, but jointly optimized, finite-impulse response filters in each step. This paper also provides an overview of recently proposed extensions of LDBP and we comment on potentially interesting avenues for future work.

9.1 Introduction

Mitigating fiber nonlinearity is a significant challenge in high-speed fiber-optic communication systems. As transmission power is increased, the nonlinear Kerr effect degrades the system performance, preventing operation at higher transmission rates, as would be expected in a linear system [25]. This performance gap motivates the development of nonlinear compensation techniques, whose design is usually based on analytical models for signal propagation in an optical fiber.

Digital backpropagation (DBP) based on the split-step Fourier method (SSFM) [1] theoretically offers ideal compensation of deterministic propagation impairments including nonlinear effects [28, 104–106]. The SSFM is arguably the most popular numerical method to solve the nonlinear Schrödinger equation (NLSE) and simulate fiber propagation, while DBP essentially reverses the SSFM operators. Other digital techniques for nonlinearity compensation include Volterra series approximations [73, 107–109] and recursive perturbation approaches [5, 110–112]. The main challenge for all these nonlinear compensation techniques is to obtain significant performance improvement and a reasonable computational complexity [113]. Indeed, several authors have highlighted the large computational burden associated with a real-time digital signal processing (DSP) implementation and proposed various techniques to reduce the complexity [3,4,8,28,112,114–118]. In many of these works, the number of steps (or compensation stages) is used not only to quantify complexity but also as a general measure of the quality for the proposed complexity-reduction method. The resulting message appears to be that fewer steps are better and provide more efficient solutions.

While previous work has indeed demonstrated that complexity savings are possible by reducing steps [3, 114, 117], the main purpose of this paper is to highlight the fact that fewer steps are not more efficient *per se*. In fact, recent progress in machine learning suggests that deep computation graphs with many steps (or layers) tend to be more parameter-efficient than shallow ones using fewer steps [119]. In this paper, we illustrate how this insight can be applied in the context of fiber-nonlinearity compensation in order to achieve low-complexity and hardware-efficient DBP. The main idea is to fully parameterize the linear steps in the SSFM by regarding them as general linear functions that can be approximated via finite impulse response (FIR) filters. All FIR filters can then be jointly optimized, similar to optimizing the weight matrices in a deep neural network (NN) [8, 120]. Complexity is reduced via pruning, i.e., progressively shortening the filters during the optimization procedure [121]. This can be seen as a form of model compression, which is commonly used in machine learning to reduce the size of NNs [122, 123]. We refer to the resulting approach as learned DBP (LDBP) [8]. The nonlinear steps in LDBP can also be parameterized and jointly optimized together with the linear steps [8]. In this paper, we assume for simplicity that the nonlinear steps remain fixed throughout the optimization procedure (similar to a conventional NN activation function).

This paper is an extension of [124], where we provided a tutorial-like introduction to LDBP. LDBP was originally introduced in [8] and the novel technical contribution in this paper lies in an experimental validation of this approach for a single-channel optical transmission system. In particular, it is demonstrated that LDBP with limited complexity can outperform standard DBP by using very short, but jointly optimized, FIR filters in each step. During the review process of this paper, another experimental demonstration of LDBP was published in [30]. Besides the different system parameters adopted for the experiments (such as fiber length, symbol rate, and transmitted constellation), our work differs from [30] in terms of the methodology followed in the LDBP pre-optimisation stage: whilst we used experimental data to optimize only the LDBP parameters, in [30] two MIMO filters are jointly optimized together with LDBP. In another recent work, the authors in [125] propose a new training method for LDBP in the presence of practical impairments such as laser phase noise. Their approach relies on extracting the relevant impairment estimates from a standard DSP chain based on chromatic dispersion (CD) compensation, which is similar to our approach discussed in Sec. 9.4.3.

This paper is organized as follows. In Sec. 9.2, we review the theoretical background behind optical fiber propagation and DBP. Sec. 9.3 introduces LDBP and shows how machine learning can be applied in the context of fiber nonlinearity compensation. Sec. 9.4 presents the experimental results and the comparison between DBP and LDBP. Sec. 9.5 provides a tutorial-style overview of related works and indicates possible avenues for future work. Finally, Sec. 9.6 concludes the paper.

9.2 Background

In this section, we review the mathematical foundation for LDBP. The optical field propagating in a fiber can be represented by a vector function of time t and distance z, $\mathbf{E}(t, z) = [E_{\mathrm{x}}(t, z), E_{\mathrm{y}}(t, z)]^\top$, which takes values in $\mathbb{C}^2$, where E_{x} and E_{y} are the components of the optical field over 2 arbitrary orthogonal polarization modes x and y. The evolution of $\mathbf{E}$ in a birefringent optical fiber in the presence of polarization-mode dispersion (PMD) is described by the Manakov-PMD equation [126] as

$$\begin{aligned}\frac{\partial \mathbf{E}(t,z)}{\partial z} = &\left(-\frac{\boldsymbol{\alpha}(z)}{2} - \frac{j\beta_2}{2}\frac{\partial^2}{\partial t^2} - \Delta\beta'(z)\overline{\boldsymbol{\sigma}}(z)\frac{\partial}{\partial t}\right)\mathbf{E}(t,z)\\ &+ j\gamma\frac{8}{9}|\mathbf{E}(t,z)|^2\mathbf{E}(t,z),\end{aligned} \tag{9.1}$$

where $\boldsymbol{\alpha} \in \mathbb{R}^{2\times 2}$ models the polarization-dependent attenuation and amplification effects in a fiber link [127], β_2 is the group-velocity dispersion coefficient, γ is the nonlinear coefficient, and $\Delta\beta'$ is the delay per unit length along the 2 local principal states of polarizations whose evolution is described by the matrix[1] $\overline{\boldsymbol{\sigma}}(z) \in \mathrm{SU}(2)$. When polarization dependent attenuation/amplification effects can be neglected, then $\boldsymbol{\alpha}(z) = \alpha\mathbf{I}$, where $\alpha \in \mathbb{R}$ is the fibre attenuation coefficient and $\mathbf{I}$ represents the identity matrix.

Although (9.1) does not have a known closed-form solution, an approximated solution can be obtained using the Baker–Campbell–Hausdorff formula [128] as

$$\begin{aligned}\mathbf{E}(t,z+h) \approx &\exp\left(\int_z^{z+h}\widehat{\mathbf{D}}(\xi)\mathrm{d}\xi\right)\\ &\exp\left(\int_z^{z+h}\widehat{\mathbf{N}}(\xi)\mathrm{d}\xi\right)\mathbf{E}(t,z),\end{aligned} \tag{9.2}$$

where $\widehat{\mathbf{D}}$ and $\widehat{\mathbf{N}}$ are the so-called linear and nonlinear operators, respectively, given by

$$\widehat{\mathbf{D}}(z) = -\frac{\boldsymbol{\alpha}(z)}{2} - \frac{j\beta_2}{2}\frac{\partial^2}{\partial t^2} - \Delta\beta'(z)\overline{\boldsymbol{\sigma}}(z)\frac{\partial}{\partial t}, \tag{9.3}$$

$$\widehat{\mathbf{N}}(z) = j\gamma\frac{8}{9}|\mathbf{E}(t,z)|^2. \tag{9.4}$$

The error incurred using (9.2) as a solution of (9.1) is vanishingly small as h decreases [58]. This approximation is the main idea behind the SSFM, which underpins DBP.

In the SSFM, the linear and nonlinear operators in (9.2) are recursively applied in frequency and time domain, respectively. The exponential of the nonlinear operator in (9.4) corresponds instead, in the time-domain, to a multiplication by the term

$$\exp\left(j\gamma\frac{8}{9}\int_z^{z+h}|\mathbf{E}(t,\xi)|^2 d\xi\right). \tag{9.5}$$

---

[1] $\mathrm{SU}(2)$ denotes the special unitary group of degree 2.

The exponential of the linear operator $\widehat{\mathbf{D}}(\xi)$ in (9.3) can be expressed in the Fourier domain as a (frequency-dependent) matrix multiplication by

$$\exp\left(-\int_{z}^{z+h} \frac{\boldsymbol{\alpha}(\xi)}{2} d\xi\right) \exp\left(j\omega^2 \frac{\beta_2}{2} h\right) \mathbf{J}(\omega, z), \tag{9.6}$$

where $\mathbf{J}(\omega, z) = \exp\left(-\int_{z}^{z+h} j\omega\Delta\beta'(\xi)\overline{\boldsymbol{\sigma}}(\xi) d\xi\right)$ is a unitary, frequency-dependent matrix, commonly referred to as (local) Jones matrix. For small enough h, the Jones matrix can be factorized as $\mathbf{J}(\omega, z) = \mathbf{R}(z)\mathbf{T}(\omega, z)$, where $\mathbf{R}$ is a unitary complex matrix which describes the evolution of the polarization state of the optical field, and where

$$\mathbf{T}(\omega, z) = \begin{bmatrix} \exp\left(-j\omega\frac{\tau(z)}{2}\right) & 0 \\ 0 & \exp\left(j\omega\frac{\tau(z)}{2}\right) \end{bmatrix} \tag{9.7}$$

with $\tau(z) = \Delta\beta'(z)h$ describes the delay over the two principal states of polarization at section z. Together, $\mathbf{R}(z)$ and $\mathbf{T}(\omega, z)$ contribute to define the evolution of PMD along the link.

The conventional DBP algorithm aims to reconstruct the transmitted field $\mathbf{E}(t, 0)$ from the received one $\mathbf{E}(t, z)$ using (9.2) recursively as[2]

$$\begin{aligned} \hat{\mathbf{E}}(t, 0) = \prod_{n=1}^{N_{\text{DBP}}} & \exp\left(-\int_{z_n}^{z_{n+1}} \widehat{\mathbf{D}}'(\xi) \mathrm{d}\xi\right) \\ & \exp\left(-\int_{z_n}^{z_{n+1}} \widehat{\mathbf{N}}(\xi) \mathrm{d}\xi\right) \mathbf{E}(t, z), \end{aligned} \tag{9.8}$$

where $\widehat{\mathbf{D}}' = -\frac{\alpha}{2} - \frac{j\beta_2}{2}\frac{\partial^2}{\partial t^2}$, z_n and $\Delta z_n = z_n - z_{n-1}$ for $n = 1, \ldots, N_{\text{DBP}}$ are the propagation section and so-called DBP *step size* at iteration n, and N_{DBP} is the number of DBP steps. Like in the SSFM implementation, the two operators in (9.8) are typically applied in frequency- and time-domain for the linear and nonlinear operators, respectively. This is performed numerically via two fast-Fourier transforms (FFTs).

Comparing (9.2) with (9.8), we note that in the conventional DBP implementation, the operator $\widehat{\mathbf{D}}'$ does not exactly invert $\widehat{\mathbf{D}}$ in (9.2), because $\widehat{\mathbf{D}}'$ does not account for the effects of $\mathbf{R}(z)$ and $\mathbf{T}(\omega, z)$. Including these two matrices in $\widehat{\mathbf{D}}'$ is challenging, since they are stochastically distributed over an ensemble of fibres and unknown to the receiver. Failing to invert $\mathbf{R}(z)$ and $\mathbf{T}(\omega, z)$ in a distributed fashion results in a performance penalty due to the uncompensated interaction between PMD and the Kerr effect [129, 130]. Combining DBP (and LDBP) with distributed PMD compensation is discussed in more detail in Sec. 9.5.2. However, distributed PMD compensation is not yet integrated into the experimental demonstration.

---

[2] Here, $\prod_{i=1}^{N} A_i = A_1 A_2 \cdots A_N$, in the operator product sense.

9.3 Efficient Multi-Step Nonlinearity Compensation using Deep Learning

For hardware-efficient and low-complexity DBP, the task is to approximate the solution of the NLSE using as few computational resources as possible. As described in the previous section, the SSFM computes a numerical solution by alternating between linear filtering steps (accounting for CD and attenuation) and nonlinear phase rotation steps (accounting for the optical Kerr effect). It was observed in [8] that this is indeed quite similar to the functional form of a deep NN, where linear (or affine) transformations are alternated with pointwise nonlinearities. In this section, we illustrate how this observation can be exploited by applying tools from machine learning, in particular deep learning.

9.3.1 Supervised Learning and Neural Networks

We start by reviewing the standard supervised learning setting for feed-forward neural networks (NNs). A feed-forward NN with M layers defines a mapping $\hat{\boldsymbol{y}} = \boldsymbol{f}_\theta(\boldsymbol{x})$ where the input vector $\boldsymbol{x} \in \mathcal{X}$ is mapped to the output vector $\hat{\boldsymbol{y}} \in \mathcal{Y}$ by alternating between affine transformations $\boldsymbol{z}^{(i)} = \boldsymbol{W}^{(i)}\boldsymbol{x}^{(i-1)} + \boldsymbol{b}^{(i)}$ and pointwise nonlinearities $\boldsymbol{x}^{(i)} = \phi(\boldsymbol{z}^{(i)})$ with $\boldsymbol{x}^{(0)} = \boldsymbol{x}$ and $\boldsymbol{x}^{(M)} = \hat{\boldsymbol{y}}$. The parameter vector θ comprises all elements of the weight matrices $\boldsymbol{W}^{(1)}, \dots, \boldsymbol{W}^{(M)}$ and vectors $\boldsymbol{b}^{(1)}, \dots, \boldsymbol{b}^{(M)}$. Given a training set $S \subset \mathcal{X} \times \mathcal{Y}$ that contains a list of desired input–output pairs, training proceeds by minimizing the empirical loss $\mathcal{L}_S(\theta) \triangleq \frac{1}{|S|}\sum_{(\boldsymbol{x},\boldsymbol{y})\in S} \ell\big(f_\theta(\boldsymbol{x}), \boldsymbol{y}\big)$, where $\ell(\hat{\boldsymbol{y}}, \boldsymbol{y})$ is a real number that, given a pair $(\boldsymbol{x}, \boldsymbol{y}) \in S$, determines the performance of the prediction $\hat{\boldsymbol{y}} = f_\theta(\boldsymbol{x})$ when $\boldsymbol{y}$ is the correct output target. We call ℓ the loss function. In our case, $\boldsymbol{x}$ is a vector of received samples after fiber propagation and some impairments compensations, $\boldsymbol{y}$ is the vector of transmitted symbols, $\hat{\boldsymbol{y}}$ is the estimated symbol vector, and ℓ is the mean-squared error (MSE) function $\ell(\hat{\boldsymbol{y}}, \boldsymbol{y}) = \|\hat{\boldsymbol{y}} - \boldsymbol{y}\|^2$, where $\|\cdot\|$ is the Euclidean norm. When the training set is large, one typically optimizes θ using a variant of stochastic gradient descent (SGD). In particular, mini-batch SGD uses the parameter update $\theta_{t+1} = \theta_t - \alpha\nabla_\theta\mathcal{L}_{B_t}(\theta_t)$, where α is the step size and $B_t \subseteq S$ is the mini-batch used in the t-th step.

Supervised machine learning is not restricted to NNs and learning algorithms such as SGD can be applied to other function classes as well. In this paper, we do not further consider NNs, but instead focus on approaches where the function $\boldsymbol{f}_\theta$ results from parameterizing a model-based algorithm, in particular the SSFM. In fact, prior to the current revolution in machine learning, communication engineers were quite aware that system parameters (such as filter coefficients) could be learned using SGD. It was not at all clear, however, that more complicated parts of the system architecture could be learned as well. For example, in the linear operating regime, PMD can be compensated by choosing the function $\boldsymbol{f}_\theta$ as the convolution of the received signal with the impulse response of a linear multiple-input multiple-output (MIMO) filter, where θ corresponds to the filter coefficients. For a suitable choice of the loss function ℓ, applying SGD then maps into the well-known constant modulus algorithm

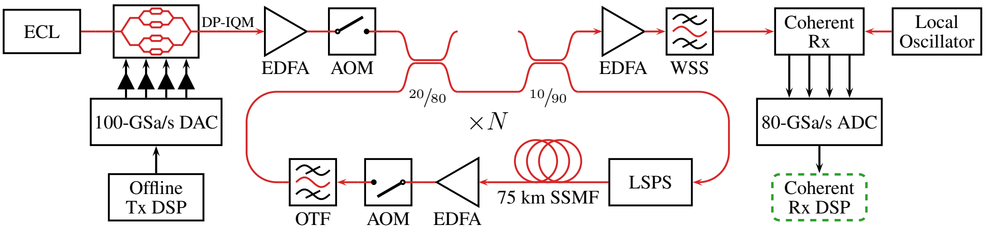

Figure 9.1: Experimental optical recirculating loop setup (ECL: external cavity laser, DP-IQ Mod: dual polarization IQ Modulator, EDFA: erbium-doped fiber amplifier, AOM: acousto-optic modulator, WSS: wavelength selective switch, DAC: digital-to-analog converter, ADC: analog-to-digital converter, DSP: digital signal processing, OTF: optical tunable filter, LSPS: loop-synchronized polarization scrambler, SSMF: standard single-mode fiber).

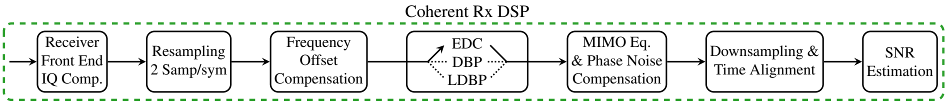

Figure 9.2: DSP chain applied to the digitized fiber output detected by the coherent receiver and analog-to-digital converter as shown in Fig. 9.1.

(CMA) [131]. For the experimental investigation in this paper, the CMA is used as part of our receiver DSP chain as an adaptive equalizer (see Sec. 9.4.1).

9.3.2 Learned Digital Backpropagation

Real-time DBP based on the SSFM is widely considered to be impractical due to the complexity of the FFTs commonly used to implement frequency-domain (FD) CD filtering. To address this issue, time-domain (TD) filtering with finite impulse response (FIR) filters has been suggested in, e.g., [28, 118, 132, 133]. In these works, either a single filter or filter pair is designed and then used repeatedly in each step. However, using the same filter multiple times is suboptimal in general and all the filter coefficients used by the DBP algorithm should be optimized jointly. To that end, it was proposed in [8] (see also [120]) to apply supervised learning based on SGD by letting the function $\boldsymbol{f}_\theta$ be the SSFM, where the linear steps are now implemented using FIR filters. In this case, θ corresponds to the filter coefficients used in *all* steps. The resulting method is referred to as LDBP.

The complexity of LDBP can be reduced by applying *model compression*, which is commonly used in ML to reduce the size of NNs [122, 123]. In this paper, we use a simple pruning approach where the FIR filters are progressively shortened during SGD [121]. Our main finding is that the filters can be pruned to remarkably short lengths without sacrificing performance. As an example, consider single-channel DBP of a 10.7-Gbaud signal over

25 × 80 km of standard single-mode fiber (SSMF) using the SSFM with one step per span (StPS). For this scenario, Ip and Kahn have shown that 70-tap filters are required to obtain acceptable accuracy [28]. This assumes that the filters are designed using FD sampling and that the same filter is used in each step. The resulting hardware complexity was estimated to be over 100 times larger than for linear equalization. On the other hand, with jointly optimized filters, it was previously demonstrated that one can achieve similar accuracy by alternating between filters that are as short as 5 and 3 taps [120]. This reduces the complexity by almost two orders of magnitude, making it comparable to linear equalization in this case.

At first glance, it may not be clear why multi-step DBP can benefit from joint optimization of the filters. After all, the standard SSFM applies *the same* CD filter many times in succession, without the need for any elaborate optimization. The explanation is that in the presence of practical imperfections such as finite-length filter truncation, applying the same *imperfect* filter multiple times can be detrimental because it magnifies any weakness. To achieve a good combined response of neighboring filters and a good overall response, the truncation of each filter needs to be delicately balanced. For a more detailed discussion, we refer readers to [120, 134].

9.4 Experimental Results

For the experimental results presented in this section, our focus is on single-channel DBP of a polarization-multiplexed (PM) 25 Gbaud signal over 1500 km of SSMF. To obtain the results, we proceed in three steps:

1. Pre-train LDBP using data from split-step simulations and apply filter pruning to obtain short FIR filters in each step.
2. Fine-tune the model using pre-processed experimental data traces.
3. Test the fully-trained model on raw experimental data traces, by integrating LDBP into the receiver DSP chain.

The pre-processed experimental data traces mentioned in step 2 are obtained using the procedures described in Sec. 9.4.3. This pre-processing is necessary in order to provide LDBP with an estimation of effects such as phase noise and state of polarization. The raw experimental data traces in step 3 are the digital domain samples of the fiber output. These raw traces are processed by a different DSP chain, described in Sec. 9.4.1. In the following, we discuss each step in more detail, starting with the experimental testbed and DSP algorithms used for the experimental validation. Effective SNR is used throughout this section as the main figure of merit. We also note that the training procedure described in Sec. 9.4.2 and Sec. 9.4.3 is performed only once, since we only consider static effects, i.e., chromatic dispersion and fiber nonlinearities. Moreover, the trained model is independent of the transmitted power, as described in more detail below.

9.4.1 Recirculating Loop Setup and DSP Chain

A schematic of the experimental recirculating loop setup is depicted in Fig. 9.1. A total of 851 traces were captured in the launch power range of -5 dBm to 6 dBm with steps of 0.5 dBm, accounting for 37 traces per launch power. For each trace, we generate offline a sequence of 2^{16} symbols, using the Permuted Congruential Generator XSL RR 128/64 random number generator [135]. A new random seed is used for each sequence. The sequences are pulse-shaped using a root-raised cosine (RRC) filter with 1% roll-off, digitally pre-compensated for transmitter bandwidth limitations and uploaded to a 100-GSa/s digital-to-analog converter (DAC). The 193.4 THz carrier is generated by an external cavity laser (ECL), modulated by a dual-polarization IQ-modulator (DP-IQM) and amplified using an erbium doped fiber amplifier (EDFA). Using acousto-optic modulators (AOMs), the optical signal is circulated in a recirculating loop consisting of a loop-synchronised polarization scrambler (LSPS), a 75-km span of SSMF, an EDFA and an optical tunable filter (OTF) for gain equalization.

At the receiver, the optical signal is amplified with an EDFA, filtered using a 50 GHz optical bandwidth wavelength selective switch (WSS) and detected using an intradyne coherent receiver consisting of a local oscillator (LO), 90-degree hybrid and 4 balanced photodiodes with 43 GHz electrical bandwidth. The resulting electrical signal is digitized by an 80-GSa/s real-time oscilloscope with an electrical bandwidth of 36 GHz.

The receiver DSP consists of seven blocks, which are applied sequentially as represented in Fig. 9.2. Orthonormalization using blind moment estimation is applied to the signal for receiver optical front-end IQ compensation (gain imbalance and offset angle between the in-phase and quadrature components). Rational resampling to 2 samples per symbol is then applied. The next step is frequency-offset estimation and compensation to correct effects such as frequency difference between the local oscillator and the signal laser and frequency offsets introduced by the AOMs. After frequency-offset compensation, we apply either electronic dispersion compensation (EDC), DBP, or LDBP. The signal is then adaptively equalized and phase noise compensated. Here we use a MIMO equalizer trained with MSE metric. The MIMO equalizer is used to recover the signal state of polarization and partially compensate for other impairments, such as PMD. Within the update loop of the equalizer, blind phase search using the known transmitted symbols removes phase noise. The equalized signal is then downsampled to 1 sample per symbol and aligned with the transmitted sequence. Finally, the effective SNR is estimated.

9.4.2 Pre-Training and Filter Pruning

Simulations are used for pre-training where the simulation parameters are closely matched to the experimental setup. In particular, we assume single-channel transmission of a 25 Gbaud signal (PM 16-QAM, 1% RRC) over 20×75.484 km of fiber ($\alpha = 0.2$ dB/km, $\beta_2 = -20.87$ ps^2/km, $\gamma = 1.3$ rad/W/km), where EDFAs (noise figure 5.0 dB) compensate for attenuation after each span. Forward propagation is simulated with 300 logarithmic StPS and 100 GHz simulation bandwidth. No PMD or other hardware impairments are included in the simulations. At the receiver, the signal is low-pass filtered (30 GHz bandwidth) and downsampled to 2 samples/symbol for further processing. LDBP is applied first, followed by a matched filter[3] (MF) and phase-offset correction. LDBP is based on the symmetric SSFM using 3 StPS and a logarithmic step size. When combining the adjacent linear half-steps, the overall model has 61 linear steps. MSE is the loss function employed for training all FIR filters, defined as $\sum_{p\in\{\mathrm{x},\mathrm{y}\}}\|\boldsymbol{y}_p - \hat{\boldsymbol{y}}_p\|^2/2$, where $\boldsymbol{y}_p$ and $\hat{\boldsymbol{y}}_p$ are the transmitted and estimated symbol vectors of the p-polarization after the phase-offset correction, respectively. We assume that the filters are symmetric and that different filters are used in each polarization. This is essentially the same methodology as described in earlier work [8, 120].

Compared to most prior work on complexity-reduced DBP, it should be stressed that our goal is not to reduce the number of steps, but instead to reduce the per-step complexity. This is accomplished by employing filter pruning. All FIR filters are initialized with constrained least-squares CD coefficients according to [2]. The approach in [2] minimizes the frequency-response error of the FIR filter with respect to an ideal CD compensation filter within the signal bandwidth, while constraining the out-of-band filter gain. The initial filter lengths are chosen large enough to ensure good performance. The filters are then progressively pruned to a given target length by forcing the outermost taps to zero at certain iterations during SGD [121]. The zero forcing is done using a masking operation in TensorFlow. The iterations where pruning occurs are predefined before the training begins. For the considered scenario, the targeted model consisted of 22 filters with 7 taps and 39 filters with 9 taps. Training is performed for 50000 iterations using the Adam optimizer [49], learning rate 0.0007, and batch size 50, which took around two hours on our machine. In principle, the number of iterations (and, hence, the training time) could be reduced, for example by setting a more aggressive learning rate. However, we observed that larger learning rates can sometimes lead to diverging MSE losses and numerical instabilities in our implementation. The filters are trained considering data from different launch powers, randomly chosen from the set $\mathcal{P} = \{1, 1.5, 2, 2.5, 3\}$ dBm, resulting in a single model that tolerates changes in the input power.

9.4.3 Fine-Tuning with Experimental Data

The next step is to fine-tune the pre-trained and pruned LDBP model using experimental data traces. The key challenge when training with experimental data is the presence of various hardware impairments and time-varying effects such as PMD and carrier phase noise. Our approach is to first estimate these impairments using the conventional DSP chain and then properly pre-process the data. The actual training is then performed with the resulting pre-processed data. In particular:

- The received data samples are pre-processed by applying receiver front-end compensation and frequency-offset compensation. The frequency offset is estimated from the

---

[3] For the experimental setup, matched filtering is implicitly performed by the MIMO equalizer.

standard DSP chain. DBP is then applied to the resulting signal to improve the estimation of phase noise and the SOP.

- The data symbols used for supervised learning are circular-shifted for alignment with the data samples.[4] These data symbols are pre-processed using the estimated phase noise process to de-rotate the symbols. More precisely, let $e^{\jmath\hat{\phi}_i}$ for $i = 1, \ldots, N$ be the estimated phase noise process, where N is the length of the data trace. Then, training is performed using the pre-processed symbols $e^{-\jmath\hat{\phi}_i} x_i$, $i = 1, \ldots, N$, where x_i are the true data symbols.

- Finally, the filter taps for the adaptive MIMO equalizer after the first 60000 symbols are extracted and saved for each data trace. The equalizer is then assumed to be static for the rest of the trace. During LDBP training, the MIMO equalizer is integrated as a static DSP component after the MF, where the saved filter coefficients are loaded and applied. Note that the MIMO filter taps are not updated during the fine tuning of LDBP.

Fine-tuning using the above approach is performed for an additional 5000 iterations using a learning rate 0.0007, and batch size 50. For training, we only consider 19 out of the 37 available traces for each launch power in the set $\mathcal{P}$, where the remaining traces are reserved for testing.

9.4.4 Testing

After fine-tuning is completed, the obtained model can then be used as a static nonlinear equalizer in the standard DSP chain described in Sec. 9.4.1 (see middle block in Fig. 9.2). During the testing phase, all DSP blocks are operated normally and the raw (i.e., not pre-processed) experimental data is used. The obtained performance is shown in Fig. 9.3 with circle and diamond markers for EDC, standard DBP (3 StPS), and LDBP (3 StPS). For DBP, a well-known issue is that the nonlinearity parameter γ is usually not known precisely and needs to be estimated [136]. We performed a simple grid search over γ, jointly with β_2, in order to optimize performance. For DBP with 3 StPS, the optimization was done at 2.5 dBm launch power, which led to an optimal value of $\gamma = 1.21$ rad/W/km and $\beta_2 = -20.90$ ps^2/km. The latter is close to the experimentally estimated $\beta_2 = -20.87$ ps^2/km. Similar to γ and β_2, the fiber length is also usually not precisely determined. We already had an estimated measure of 75.484 km for the span length, which was confirmed to be optimum after a grid search. The optimum attenuation coefficient for DBP was $\alpha = 0.19$ dB/km, the same as in the fiber specifications. DBP with 3 StPS achieves a peak-SNR gain of 2.1 dB over EDC. The peak-SNR gain obtained by DBP is similar to those reported in prior experimental studies on single-channel DBP [137, 138]. DBP also improves the optimum launch power with respect

---

[4] In principle, LDBP with asymmetric FIR filters could learn to recover a circular shift. However, due to the use of symmetric filters, a manual shift has to be applied. For the pre-training in Sec. 9.4.2, no circular shift is necessary since the sequences are already perfectly aligned.

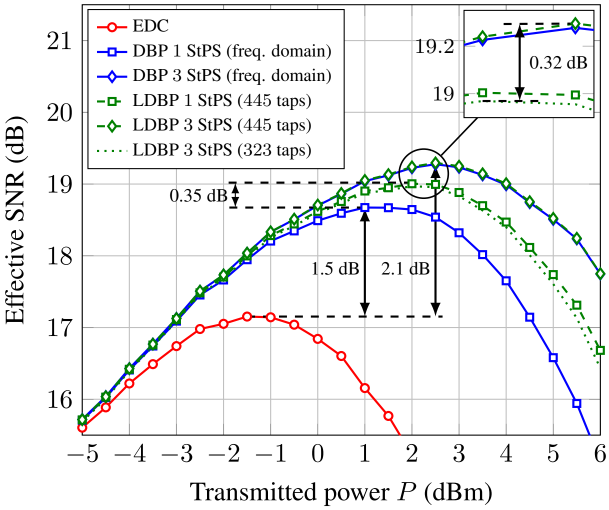

Figure 9.3: Experimental results for single-channel transmission of a 25 Gbaud signal with PM 16-QAM over 1500 km.

to EDC by 4 dB, from -1.5 dBm to 2.5 dBm. By using LDBP, the peak-SNR gain is slightly increased with respect to DBP. Further increasing the number of StPS or filter taps for LDBP did not improve performance. The optimum launch power for LDBP remains the same as the one for DBP. We also repeated the same procedure assuming 1 StPS for both DBP and LDBP, in which case the LDBP model uses 21 filters per polarization, where 12 filters are pruned to 23 taps and 9 filters to 21 taps. The results in Fig. 9.3 (square markers) show that in this case LDBP achieves a performance improvement of around 0.35 dB with respect to DBP. For DBP with 1 StPS, the optimum values for γ and β_2 were found to be $\gamma = 1.62$ rad/W/km and $\beta_2 = -21.41$ ps^2/km.

In terms of complexity, it has been shown that the power consumption and chip area for time-domain DBP [139] and LDBP [121] are dominated by the linear steps, whereas the nonlinear steps have efficient hardware implementations using a Taylor expansion. Therefore, we focus on the linear steps for simplicity. As a simple surrogate measure for complexity, we use the overall impulse response length of the entire LDBP model, which is defined as the length of the filter obtained by convolving all LDBP subfilters. Since the same filter lengths are used in both polarizations, one may focus on a single polarization. For the 3-StPS model, we have 22 filters of length 7 and 39 filters of length 9. Hence, the overall impulse response length is $2(22 \cdot (7-1)/2 + 39 \cdot (9-1)/2) + 1 = 445$ taps. For the 1-StPS model, the overall impulse response length is $2(12 \cdot (23-1)/2 + 9 \cdot (21-1)/2) + 1 = 445$, i.e., the same as the 3-StPS model. Thus, even though the number of steps is reduced by a factor of 3 and performance decreases by around 0.3 dB (see the inlet figure in Fig. 9.3), the expected hardware complexity of the two models is roughly comparable. Moreover, the overall impulse

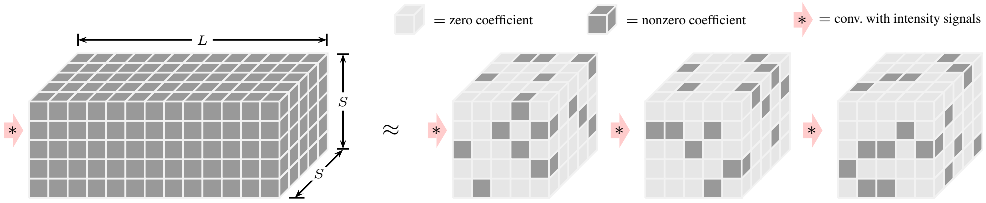

Figure 9.4: Tensor representation of an L-tap $S \times S$ MIMO filter for DBP based on subband processing, where S is the number of subbands (left); learned multi-step decomposition with sparse subfilters (right).

response lengths should be compared to the memory that is introduced by CD. To estimate the memory, one may use the fact that CD leads to a group delay difference of $2\pi|\beta_2|\Delta f L_{\text{tot}}$ over a bandwidth Δf and transmission distance L_{tot}. Normalizing by the sampling interval T, this confines the memory to roughly $(2\pi|\beta_2|\Delta f L_{\text{tot}})/T$ samples. For our scenario, we have $\beta_2 = -20.87$ ps^2/km, $L_{\text{tot}} \approx 1510$ km, and $1/T = 50$ GHz. The bandwidth Δf depends on the baud rate, the pulse shaping filter, and the spectral broadening during propagation. In order to obtain an estimate for Δf, we quantified the effect of spectral broadening in an ideal noiseless simulation environment for the same parameters as listed in Sec. 9.4.2. The bandwidth percentage (with respect to $1/T$) that contained 99.9% of the received signal power was found to vary between 51% for $P = -4$ dBm and 77% for $P = 6$ dBm. With these numbers, the CD memory varies between 253 and 381 taps, which is comparable to the impulse response length of LDBP. This is a major improvement compared to previous work where the filter lengths in DBP are significantly longer than the CD memory, sometimes by orders of magnitude [28, 140]. We also note that it is possible to further prune the filters at the expense of some performance loss. To illustrate this, we further pruned the 3-StPS model to 22 filters of length 5 and 39 filters of length 7. This gave a peak-SNR penalty of 0.32 dB (see Fig. 9.3), making the performance comparable to the 1-StPS model, while at the same time reducing the overall impulse response length to only 323 taps.

9.5 Outlook and Future Work

In this section, we give an overview of related work on LDBP that has previously appeared in the literature and also comment on potentially interesting avenues for future work.

9.5.1 Sparse MIMO Filters for Subband Processing

The complexity of DBP with TD filtering is largely dominated by the total number of required CD filter taps in all steps and this increases quadratically with bandwidth, see, e.g., [141, 142]. Thus, efficient TD-DBP of wideband signals is challenging. One possible solution is to em-

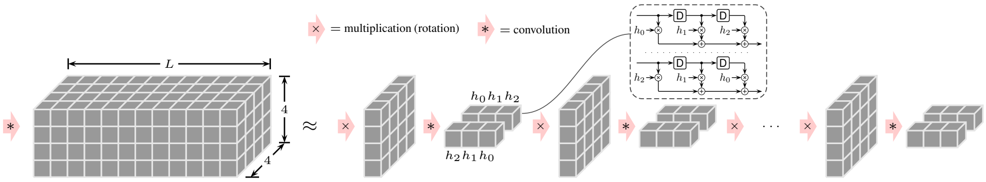

Figure 9.5: Tensor representation of an L-tap 4×4 MIMO filter for PMD compensation (left); multi-step decomposition where 4-D rotations are alternated with short fractional-delay (FD) filters accounting for DGD (right). Each FD filters is applied to both the real and imaginary part.

ploy subband processing and split the received signal into S parallel signals using a filter bank [141–148]. A theoretical foundation for DBP based on subband processing is obtained by inserting the split-signal assumption $u = \sum_{i=1}^{S} u_i$ into the NLSE. This leads to a set of coupled equations which can then be solved numerically. We focus on the modified SSFM proposed in [149] which is essentially equivalent to the standard SSFM for each subband, except that all sampled intensity waveforms $|u_1|^2, \dots, |u_S|^2$ are jointly processed with a MIMO filter prior to each nonlinear phase rotation step. This accounts for cross-phase modulation between subbands but not four-wave mixing because no phase information is exchanged.

The MIMO filters for subband processing can be relatively demanding in terms of hardware complexity. As an example, in [148] we considered a scenario where a 96-Gbaud signal is split into $S = 7$ subbands. For a filter length of 13, the MIMO filter in each SSFM step can be represented as a $7 \times 7 \times 13$ tensor with 637 real coefficients which is shown in Fig. 9.4 (left). The resulting complexity per step and subband would be almost 6 times larger than that of the CD filters used in [148]. The situation can be improved significantly by decomposing each MIMO filter into a cascade of sparse filters as shown in Fig. 9.4 (right). For a cascade of 3 filters, it was shown that a simple L_1-norm regularization applied to the filter coefficients during SGD leads to a sparsity level of round 8%, i.e., 92% of the filter coefficients can be set to zero with little performance penalty. Note that this filter decomposition happens *within* each SSFM step. In other words, complexity is reduced by further increasing the depth of the multi-step DBP computation graph.

9.5.2 Distributed PMD Compensation

Different techniques have been proposed in previous works to embed the distributed compensation of PMD in the DBP algorithm, when the knowledge of the PMD evolution in the link is missing [129, 130, 150]. In this section, we describe how distributed PMD compensation can be combined with LDBP in a hardware-efficient manner.

As discussed in Sec. 9.2, PMD can be modeled by dividing a fiber link of length L_{tot} into $M = L_{\text{tot}}/h$ sections, where for large enough M the link Jones matrix $\mathbf{J}_{\text{Link}}(\omega)$ can be factorized as

$$\mathbf{J}_{\text{Link}}(\omega) \triangleq \exp\left(-j\omega \int_0^{L_{\text{tot}}} \Delta\beta'(\xi)\overline{\boldsymbol{\sigma}}(\xi)d\xi\right) = \prod_{i=1}^{M} \mathbf{R}^{(i)}\mathbf{T}^{(i)}(\omega) \tag{9.9}$$

where $\mathbf{R}^{(i)} \triangleq \mathbf{R}(ih)$ and $\mathbf{T}^{(i)}(\omega) \triangleq \mathbf{T}(ih, \omega)$ for $i = 1, 2, \ldots, M$. PMD compensation (and polarization demultiplexing) then amounts to finding and applying the inverse $\mathbf{J}_{\text{Link}}^{-1}(\omega)$ to the received signal. This is typically performed after CD compensation, e.g., using an L-tap MIMO filter that tries to approximate $\mathbf{J}_{\text{Link}}^{-1}(\omega)$. Fig. 9.5 (left) shows the corresponding tensor representation assuming a real-valued 4×4 filter that is applied to the separated real and imaginary parts of both polarizations [151].

An efficient multi-step decomposition of this filter is depicted in Fig. 9.5 (right), which essentially mimics (9.9) in a reverse fashion. Here, the matrices $\mathbf{T}^{(i)}(\omega)$ are approximated with two real-valued fractional-delay (FD) filters employing symmetrically flipped filter coefficients for different polarizations. The FD filters can be very short provided that the expected DGD per step is sufficiently small (i.e., many steps are used). In [152], it was shown how to integrate the decomposed filter structure into LDBP. The resulting multi-step PMD architecture can be trained effectively using SGD. An important feature compared to previous work is the fact that the employed approach does not assume any knowledge about the particular PMD realizations along the link, nor any knowledge about the total accumulated PMD. However, more research is needed to fully characterize the training behavior, e.g., in terms of convergence speed for adaptive compensation.

9.5.3 Coefficient Quantization and ASIC Implementation

Fixed-point requirements and other DSP hardware implementation aspects for DBP have been investigated in [118, 121, 139, 140, 153]. A potential benefit of multi-step architectures is that they empirically tend to have many "good" parameter configurations that lie relatively close to each other. This implies that even if the optimized parameters are slightly perturbed (e.g., by quantizing them) there may exist a nearby parameter configuration that exhibits similarly good performance to mitigate the resulting performance loss due to the perturbation.

Numerical evidence for this phenomenon can be obtained by considering the joint optimization of CD filters in DBP including the effect of filter coefficient quantization. This has been studied in [121] and the approach relies on applying so-called "fake" quantizations to the filter coefficients, where the gradient computations and parameter updates during SGD are still performed in floating point. Compared to other quantization methods, this jointly optimizes the responses of quantized filters and can lead to significantly reduced fixed-point requirements. For the scenario in [121], it was shown for example that the bit resolution can be reduced from 8-9 coefficient bits to 5–6 bits without adversely affecting performance. Furthermore, hardware synthesis results in 28-nm CMOS show that multi-step DBP based on TD filtering with short FIR filters is well within the limits of current ASIC technology in terms of chip area and power consumption [121, 139].

9.6 Conclusions

We have illustrated how machine learning can be used to achieve efficient fiber-nonlinearity compensation. Rather than reducing the number of steps (or steps per span), it was highlighted that complexity can also be reduced by carefully designing and optimizing multi-step methods, or even by increasing the number of steps and decomposing complex operations into simpler ones, without losing performance. We also avoided the use of neural networks as universal (but sometimes poorly understood) function approximators. Instead, the considered learned digital backpropagation relied on parameterizing the split-step method, i.e., an existing model-based algorithm. We have performed an experimental demonstration of this approach, which was shown to outperform standard digital backropagation with limited complexity. Some extensions of the approach and steps towards possible future works were also presented, showing that there is a possibility for further performance improvements in these systems.

CHAPTER 10

Paper F: High-cardinality hybrid shaping for 4D modulation formats in optical communications optimized via end-to-end learning

V. Oliari, B. Karanov, S. Goossens, G. Liga, O. Vassilieva, I. Kim, P. Palacharla, C. Okonkwo, A. Alvarado, “High-cardinality hybrid shaping for 4D modulation formats in optical communications optimized via end-to-end learning,” in *arXiv:2112.10471*, Dec., 2021.

Abstract

In this paper we carry out a joint optimization of probabilistic (PS) and geometric shaping (GS) for four-dimensional (4D) modulation formats in long-haul coherent wavelength division multiplexed (WDM) optical fiber communications using an auto-encoder framework. We propose a 4D 10 bits/symbol constellation which we obtained via end-to-end deep learning over the split-step Fourier model of the fiber channel. The constellation achieved 13.6% reach increase at a data rate of approximately 400 Gbits/second in comparison to the ubiquitously employed polarization multiplexed 32-QAM format at a forward error correction overhead of 20%.

10.1 Introduction

JOINT optimization of transmitter and receiver digital signal processing (DSP) blocks, such as coding, modulation, and equalization, can be challenging in optical communications. One possible way of jointly optimizing these blocks is using an autoencoder structure, as first proposed for wireless communications in [154]. In the context of optical fiber communications, autoencoders were first introduced and experimentally demonstrated for highly-nonlinear dispersive short-reach links [155]. The concept was then also applied for long-haul coherent fiber systems, optimizing the modulation format using a simple approximated model of the nonlinear channel for 2D constellations [13, 156, 157]. Deep learning was also used for obtaining 4D modulation formats in [32], where optimization was performed in the linear regime and the performance was tested for the nonlinear optical fiber channel for 7 bits/symbol and constant modulus constellations. Beyond deep learning, many strategies for geometric shaping (GS) optimization have been proposed in the literature. In [31], 4D 7 bits/symbol modulation formats were also considered.

In addition to optimizing the modulation format, another technique for improving data rates is to optimize the symbol probabilities. In [33], symbol probabilities for polarization-multiplexed (PM) quadrature amplitude modulation (QAM) constellations were optimized on a simplified model and then tested on the nonlinear fiber channel. Finding the optimal modulation format geometry and symbol probabilities is a challenging task and an open problem in optical fiber communications [158]. On the other hand, as shown in [36, 159] for the wireless channels, deep learning and artificial neural networks (ANN) can provide viable alternatives to the conventional approaches and enable joint GS and probabilistic shaping (PS), which is called hybrid GS and PS.

In this paper, we perform hybrid GS and PS for optical fiber communications using the split-step Fourier method (SSFM) for dual polarization as our channel model. SSFM is one of the most accurate representations of the nonlinear propagation in optical fibers and has already been used in the autoencoder framework [34]. However, in [34], the waveform is optimized together with a 2D constellation format. The optimized constellations in this paper are in 4D and have no constraints in terms of energy or symmetries. This is the first time, to the best of our knowledge, that a 4D 10 bits/symbol constellation has been optimized for the nonlinear optical channel using SSFM data. The results are validated via generalized mutual

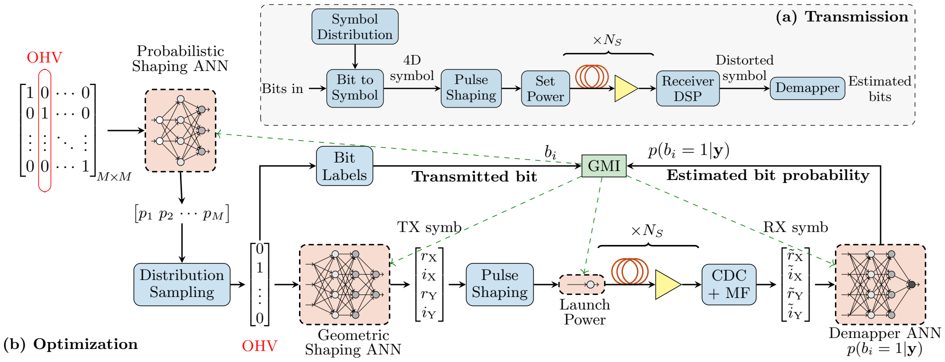

Figure 10.1: (A) Transmission system used to validated the performance of different modulation formats. (B) Autoencoder setup used to obtain optimal constellation and a priori symbol probabilities. The blocks for probabilistic shaping, geometric shaping, and demapper are built using dense neural networks.

information (GMI) [35]. The optimized constellation demonstrates gains in terms of GMI and transmission distance with respect to both PM-32QAM and PM-64QAM, which are 10 and 12 bits/symbol constellations, respectively.

10.2 End-to-end System and Performance Metric

The GS and PS optical fiber system considered in this paper is shown in Fig. 7.1 (a), where the input bits are associated with a transmitted symbols drawn from a certain symbol distribution. These symbols can use a different GS scheme for each transmission case. For example, regular QAM formats or deep learning optimized constellations can be used in the transmission. These symbols are upsampled at 16 samples per symbol and pulse-shaped by a root-raised cosine filter with 0.01 roll-off. The resulting filtered waveform is scaled to achieve a given launch power and propagated in the fiber. The fiber is modeled by the Manakov equation for dual polarization [38]

$$\frac{\partial \mathbf{A}(t,z)}{\partial z} = -\frac{j\beta_2}{2}\frac{\partial^2 \mathbf{A}(t,z)}{\partial t^2} + j\frac{8}{9}\gamma e^{-\alpha z}\left\|\mathbf{A}(t,z)\right\|^2 \mathbf{A}(t,z), \tag{10.1}$$

where $\mathbf{A}(t,z)$ is the dual-polarization transmitted signal, β_2 is the group-velocity dispersion parameter, γ is the nonlinear Kerr coefficient and α the attenuation coefficient. For the simulations carried on this paper, we transmitted 5 channels, each of them at 50 Gbaud and channel spacing of 51.5 GHz. We have chosen a small difference between symbol rate and channel spacing in order to obtain high spectral efficiency. We considered $\beta_2 = -21.67$ ps^2/km, $\gamma = 1.2$ 1/W/km, and $\alpha = 0.2$ dB/km. The transmission is performed over N_S spans

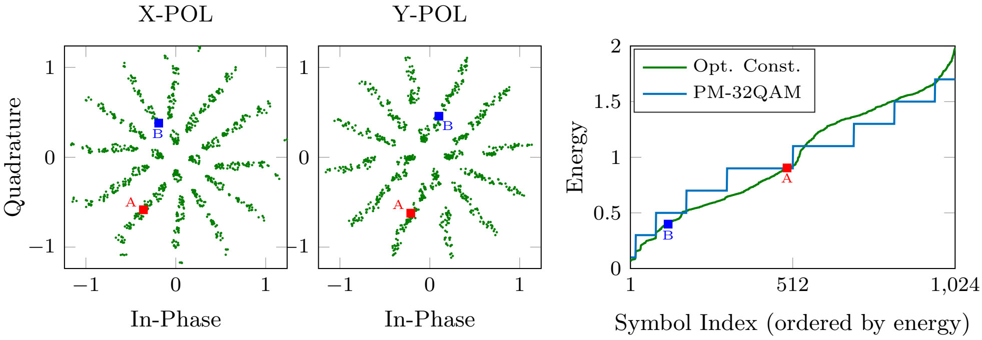

Figure 10.2: Optimized 4D constellation via the autoencoder structure of Fig. 7.1 (A) for X and Y polarizations (left). Energy per symbol index (right) for the optimized constellation and PM-32QAM at optimum launch power and 4000 km.

of 80 km each, where an EDFA with noise figure of 5 dB is used at the end of each span. After propagation, the receiver applies chromatic dispersion compensation, matched filter, and sampling to the received signal, resulting in the received symbols. The received symbols are given to a demapper, which estimates the transmitted bits. In the system of Fig. 7.1 (a), we compare the different modulation formats in terms of the generalized mutual information (GMI) [35]. The equation for the GMI was obtained by adapting [35, Eq. (36)] for different a priori probabilities and 4D formats.

Fig. 7.1 (b) shows the autoencoder system used to optimize the constellation geometry and symbol probabilities. The joint optimization of PS and GS follows the same idea described in [36]. The optimization system has the same fiber link as the transmission system described for Fig. 7.1 (a). The symbol probabilities are obtained from an ANN, whose input are one-hot vectors (OHVs) representing each possible symbol. The ANN output is the logits of the respective symbol probability $[p_1, p_2, \cdots, p_M]$ and each of the five channels has its respective ANN. After obtaining all symbol probabilities, a distribution sampling based on the straight-through Gumbel-Softmax estimator [54] outputs OHVs sampled according to the previously obtained symbol probabilities. These OHVs are the input of another ANN, labeled as Geometric Shaping in Fig. 7.1 (b). For each possible OHV, this ANN outputs a transmitted 4D symbol represented by $[r_\mathrm{X}, i_\mathrm{X}, r_\mathrm{Y}, i_\mathrm{Y}]$, where r_X and i_X are the in-phase and quadrature components of the X polarization, and r_Y and i_Y are the respective components of the Y polarization. Each of the five channels has its respective ANN for the 4D symbol mapping. The transmitted symbols are pulse-shaped by the same filter as in Fig. 7.1 (a) and the transmitted power for each channel is individually learned. For the training procedure, we used the SSFM with a fixed number of spans $N_S = 50$. The received signal is processed by the DSP, resulting in the received symbols $\mathbf{y} = [\tilde{r}_\mathrm{X}, \tilde{i}_\mathrm{X}, \tilde{r}_\mathrm{Y}, \tilde{i}_\mathrm{Y}]$. These symbols are the input of a set of ANNs, labeled as Demapper, where each of them estimates the bit probabilities

$p(b_i = 1|\mathbf{y})$ for a specific bit i. Each channel has its own set of Demapper ANNs. This bit probability estimation is similar to the procedure described in [13], in which $p(b_i = 1|\mathbf{y})$ is used to estimate the GMI via [13, Eq. (2)]

$$\text{GMI} \approx H(\mathbf{X}) + \frac{1}{K}\sum_{k=1}^{K}\sum_{i=1}^{m} h_b(b_{i,k}, r_{i,k}), \tag{10.2}$$

where $H(\mathbf{X})$ is the entropy of the random vector $\mathbf{X}$ of the transmitted symbols, $b_{i,k}$ is the i-th bit of the k-th transmitted symbol, $r_{i,k}$ is the estimated probability $p(b_{i,k} = 1|\mathbf{y}_k)$ given the received symbol $\mathbf{y}_k$, m is the number of bits per symbol, and K is the number of transmitted symbols. In (10.2), we use the function h_b given by

$$h_b(b_{i,k}, r_{i,k}) = b_{i,k}\log(r_{i,k}) + (1 - b_{i,k})\log(1 - r_{i,k}). \tag{10.3}$$

The GMI estimation in (10.2) is different from the one used in [35, Eq. (36)], for example. Computing the expression in [35, Eq. (36)] for 4D modulation formats with 10 bits/symbol is more computational demanding than (10.2), which is why we used (10.2) for the optimization process. On the other hand, since (10.2) demands an ANN to compute the bit probabilities, the adaptation of [35, Eq. (36)] for different a priori probabilities is used to compare the performance of the different modulation formats.

In our system, the geometric shaping ANN has 3 layers with ReLU activation and a final layer with linear activation, all densely connected and with 256 nodes. The probabilistic shaping ANN has a similar structure, but with 2 layers with ReLU activation instead of 3, and also an output layer with linear activation function. We use a linear activation function for the output layer since first we obtain the logits and then the symbol probabilities. The m demapper ANNs are composed by 4 densely connected layers with 256 nodes each, where the first three activation functions are ReLU and the last one is a sigmoid, since their outputs are bit probabilities. We sum the GMI estimation of each channel and use the result as the loss function for the system. The training was performed using an ADAM optimizer as in [155] with learning rate 0.0005, and exponential decays for first- and second-order moments given by 0.9 and 0.999, respectively. The batch size was 2 and the number of symbols for each channel per mini-batch was 2^{13}. The simulations were run in single precision for approximately 300000 optimization iterations. The low batch size, number of symbols per channel, and the choice of single precision was due to memory limitations in the simulation.

We used two different systems, one for transmission and one for optimization. This is to emphasize that the ANNs present in the optimization are only used to obtain the symbol probabilities and constellation points. Therefore, the system complexity is the same as a standard 4D transmission[1].

---

[1] The demapper, which could be a burden for 4D modulation formats, could be implemented with a computationally efficient ANN [32]. However, the tested transmission system was simulated without an ANN.

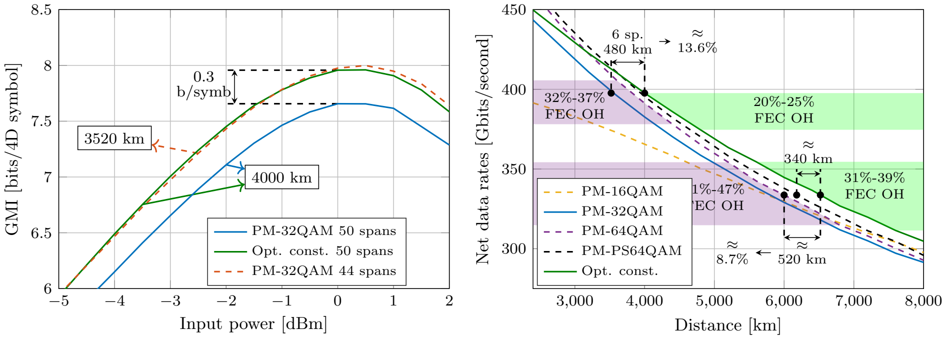

Figure 10.3: GMI results versus input power (left) and net rates versus distance (right).

10.3 Results

Fig. 10.2 shows the normalized constellations in X and Y polarizations obtained via the autoencoder structure of Fig. 7.1 (b). The illustrated constellation is respective to one of the outer channels. Although these constellations suggest symmetries in each polarization, these patterns were all learned by the system without any constraint applied. Interestingly, the probabilities for the learned constellations of all channels converged to uniform probabilities. This uniform distribution might indicate that the geometry of the constellation is more important than its probability distribution at optimum launch power for this relatively large number of constellation points in 4D. Fig. 10.2 also depicts the energy of each symbol for the learned constellation and for PM-32QAM, which also has 10 bits/4D-symbol. As shown in Fig. 10.2, the symbols have a wide energy variation, indicating that an energy constrain might not be necessary when optimizing for the nonlinear optical channel. The learned constellation is not polarization-multiplexed as in the case of PM-32QAM. The energy of two specific symbols (A and B) is also highlighted.

Fig. 10.3 depicts the average GMI over the 5 channels for the optimized constellation and traditional QAM constellations. For these results, all channels were propagated with same launch power since using the different learned launch powers per channel by the autoencoder did not provide additional gains. The left part of Fig. 10.3 shows the GMI versus distance at 4000 km ($N_S = 50$ spans). At this distance, the proposed constellation achieves an average of approximately 400 Gbits/symbol or 8 bits/symbol, which yields a spectral efficiency of approximately 7.76 bits/s/Hz. The proposed constellation also outperforms PM-32QAM by 0.3 bits/symbol at optimum launch power. In addition, this constellation shows better performance than PM-32QAM in the linear regime. The performance of the optimized constellation is close to the performance of PM-32QAM for $N_S = 44$ spans (3520 km), which indicates a 13.6% reach increase.

Fig. 10.3 (right) shows the net rate per channel versus distance for the optimized constellation, PM-32QAM, PM-64QAM, and PM-PS64QAM. The latter modulation format corresponds to probabilistic-shaped PM-64QAM using a Maxwell–Boltzmann distribution. These results show that the optimized constellation outperforms both PM-16QAM and PM-32QAM for all the displayed distances, and outperforms PM-64QAM for distances higher than 3500 km. Between 4000 and 4800 km, the forward error correction (FEC) overhead (OH) to obtain the data rate given by the optimized constellation is between 20% and 25%, while for PM-64QAM, a FEC OH between 32% and 37% is necessary to obtain similar data rates. At 6000 km, PM-64QAM can achieve approximately 334 Gbits/symbol with a respective FEC OH of 44%. For the same net rate, the optimized constellation has a reach increase of approximately 520 km (8.7%) with respect to PM-64QAM and 340 km (5.5%) with respect to PM-PS64QAM, while demanding a FEC OH of 33%. The increased distance indicates a better nonlinear tolerance for the optimized constellation, while also keeping a lower FEC complexity than PM-64QAM.

Other 4D modulation formats can be found on the literature, for example in [160]. However , as reported in [161], these constellations perform suboptimally in terms of GMI when compared to PM-MQAM formats with the same number of bits/symbol. In addition, finding a binary labeling for those 4D constellations is challenging [161].

10.4 Conclusions

We have presented a 4D 10 bits/symbol modulation format which outperforms standard PM-32QAM and PM-64QAM at distances greater than 3500 km. The proposed constellation was obtained via an autoencoder structure, where the split-step Fourier method was used as the channel model. The gains were mainly driven by geometric shaping, since the symbol probabilities converged to a uniform distribution. The resulting symbols had a wide energy variation, contradicting forced constant energy approaches used in the literature. Future works include developing 4D modulation formats with even more than 10 bits/symbol and to include additional fiber impairments.

CHAPTER 11

Conclusions

In this thesis, we studied analytical models for fiber propagation and how machine learning can be used in some optical system applications. The goal of the study was to answer research questions related to the modeling of the nonlinear fiber propagation and to the optimization of receivers and constellation geometry.

The first research question was

> **RQ-1** How to obtain an analytical fiber model that is accurate in the very high nonlinear regime without increasing the perturbation order of RP on the Kerr coefficient?

This research question was answered in Chapters 5 and 6, which represent papers [15] and [16], respectively. In these papers, RP on β_2 was proposed for the modeling of fiber propagation on the highly-nonlinear regime. The performance of the model was analyzed using the NSD metric, in which the model waveform is compared with the SSFM output waveform.

When deriving RP on β_2, the zero-th order solution resulted in the NLPN model, which consists of the NLSE solution when only nonlinear effect is considered. This term allows RP on β_2 to maintain its accuracy almost constant until high input powers. The dispersion effect is only considered in the first order term, in which the interaction of both linear and nonlinear effects is modeled. However, the amount of accumulated dispersion that RP on β_2 can accurately model is limited. When increasing the fiber length or signal bandwidth, the model starts to significantly decrease its accuracy.

The main conclusions of these works are

- RP on β_2 is a first-order model capable of modeling the highly nonlinear regime;
- This model also requires low accumulated dispersion.

> **RQ-2** How to improve the accuracy of the proposed model to tolerate more accumulated dispersion and higher input powers?

This research question was answered in Chapters 7 and 8, which represent papers [17] and [18], respectively. In these papers, instead of applying RP theory, we used the FLP approach on the β_2 coefficient, which consists of applying LP on the frequency domain. In RP models, the solution of the NLSE is expressed as a power series of a certain coefficient. For the LP and FLP methods, the power series is considered inside an exponential function. The terms of this series are functions of the RP terms.

FLP on β_2 showed more tolerance to accumulated dispersion and nonlinear effects than RP on β_2. The performance of FLP on β_2 was analyzed in a PON system and the proposed model outperformed RP, LP, and ERP on γ models when considering a 0.1% NSD threshold. The proposed model was also used to heuristically generate decision regions. These regions were obtained by approximating the probability density function of the received symbols when the channel was modeled by FLP on β_2. The performance of these decision regions was analyzed in terms of BER and AIR. From the compared models, the results for FLP on β_2 in this last analysis were the closest to the SSFM results.

The main conclusions of these works are

- FLP on β_2 has higher dispersion and nonlinear tolerance than RP on β_2;
- FLP on β_2 is also accurate when analyzing the performance in the discrete-time domain.

RQ-3 How does LDBP perform in experiments, where other sources of impairments are present?

This research question was answered in Chapter 9, which consists of paper [19]. In [19], LDBP managed to achieve a slightly better performance than DBP. The performance metric was the SNR and the system consisted of a single channel transmitted over multiple spans.

In simulation results, DBP is capable of increasing its accuracy as the number of steps per spans increase. However, when used with experimental data, the DBP performance saturated at 3 steps per spans. This behavior might be justified by the presence of other effects present in the experimental setup, such as transceiver noise. The performance of LDBP also saturated slightly above DBP's performance. Even for LDBP, increasing the number of steps per span or the number of filter taps did not result in additional gains. Although the performance of LDBP saturated, it was still able to achieve 2.1 dB gain in SNR over EDC by using only 445 filter taps. Additional increases in SNR might still be possible if the compensation of other effects, such as PMD, are included in the LDBP structure.

The main conclusions of this work are

- LDBP can provide gains over EDC which are comparable to DBP;
- These gains can be achieved using a low number of filter taps;
- Experimental effects not modeled in LDBP might saturate its performance.

RQ-4 Which are the best 4D symbol constellations and a priori probabilities when transmitting a signal in the nonlinear fiber?

This research question was investigated in Chapter 10, which consists of paper [20]. In [20], a system based on machine learning was built to optimize the symbol constellations and a-priori probabilities. The results showed gains over regular QAM constellations.

The machine learning system was built using an autoencoder structure. The system generated its own input symbols with respective a priori probabilities. These symbols were compared with the received ones after fiber propagation. Each transmitted channel had its own constellation and a priori probabilities. The optimum a priori probabilities converged to a uniform distribution, which might indicate that GS only is sufficient at optimum launch power. The optimum constellation showed a large variation in terms of symbol energy, which contradicted some results in the literature where the symbol energy is required to be constant.

The main conclusions of this work are

- The proposed autoencoder system was able to obtain state-of-the-art constellations which performed better than standard QAM constellations;
- Since the optimization is machine learning based, we cannot guarantee this is the optimal constellation for the system.

Appendix: Derivation of RP models

A.1 Proof of Theorem 1 from Paper B and Sec. 3.4.1

Proof. Substituting (6.14) in (6.3) yields

$$\sum_{k=0}^{\infty}\gamma^{k}\frac{\partial A_k(t,z)}{\partial z}+\frac{j\beta_2}{2}\sum_{k=0}^{\infty}\gamma^{k}\frac{\partial^2 A_k(t,z)}{\partial t^2}= \\ j\gamma \mathrm{e}^{-\alpha z}\sum_{m=0}^{\infty}\sum_{n=0}^{\infty}\sum_{p=0}^{\infty}\gamma^{m+n+p}A_m(t,z)A_n^*(t,z)A_p(t,z). \tag{A.1}$$

Every term in (A.1) is multiplied by a term γ^l with $l = 0, 1, \ldots$. We will solve (A.1) by equating the terms with same power of γ for increasing values of l.

For γ^0 $(l = 0)$, we obtain

$$\frac{\partial A_0(t,z)}{\partial z}=-\frac{j\beta_2}{2}\frac{\partial^2 A_0(t,z)}{\partial t^2}, \tag{A.2}$$

whose solution (with initial condition $A_0(t,0) = A(t,0)$) is

$$A_0(t,z)=\mathcal{D}_z\{A(\cdot,0)\}(t). \tag{A.3}$$

For γ^1 $(l = 1)$, we obtain

$$\frac{\partial A_1(t,z)}{\partial z}=-\frac{j\beta_2}{2}\frac{\partial^2 A_1(t,z)}{\partial t^2}+j\mathrm{e}^{-\alpha z}S(t,z), \tag{A.4}$$

where

$$S(t,z)=|A_0(t,z)|^2A_0(t,z). \tag{A.5}$$

We solve (A.4) in the Fourier domain as

$$\frac{\partial\tilde{A}_1(\omega,z)}{\partial z}=\frac{j\beta_2\omega^2}{2}\tilde{A}_1(\omega,z)+j\mathrm{e}^{-\alpha z}\tilde{S}(\omega,z). \tag{A.6}$$

Grouping the terms related to A_1, (A.6) is expressed as

$$\frac{\partial\left[\tilde{A}_1(\omega,z)\mathrm{e}^{-\frac{j\beta_2}{2}\omega^2 z}\right]}{\partial z}=j\mathrm{e}^{-\alpha z}\mathrm{e}^{-\frac{j\beta_2}{2}\omega^2 z}\tilde{S}(\omega,z). \tag{A.7}$$

By using the initial condition $A_1(t,0)=0$, (A.7) is solved as

$$\tilde{A}_1(\omega,z)=j\int_0^z \mathrm{e}^{-\alpha u}\mathrm{e}^{\frac{j\beta_2}{2}\omega^2(z-u)}\tilde{S}(\omega,u)\mathrm{d}u. \tag{A.8}$$

The last step in the proof is to take the inverse Fourier transform of (A.8). To do this, we use the fact that the operator $\mathcal{D}_z$ in (6.10) can be represented in the frequency domain as

$$\tilde{\mathcal{D}}_z\{\tilde{f}\}(\omega)=\tilde{f}(\omega)\mathrm{e}^{\frac{j\beta_2}{2}\omega^2 z}. \tag{A.9}$$

Replacing $\tilde{f}$ by $\tilde{S}(\cdot,u)$ in (A.9) gives

$$\tilde{\mathcal{D}}_z\{\tilde{S}(\cdot,u)\}(\omega)=\tilde{S}(\omega,u)\mathrm{e}^{\frac{j\beta_2}{2}\omega^2 z}. \tag{A.10}$$

Now, instead of applying the operator $\tilde{D}_z$ at distance z, we use it at distance $z-u$, obtaining

$$\tilde{\mathcal{D}}_{z-u}\{\tilde{S}(\cdot,u)\}(\omega)=\tilde{S}(\omega,u)\mathrm{e}^{\frac{j\beta_2}{2}\omega^2(z-u)}. \tag{A.11}$$

The time-frequency dual representation of the operator $\mathcal{D}_z$ is

$$\mathcal{F}^{-1}\{\tilde{\mathcal{D}}_{z-u}\{\tilde{f}\}\}(t)=\mathcal{D}_{z-u}\{f\}(t), \tag{A.12}$$

and thus, the inverse Fourier transform of the left-hand side of (A.11) is

$$\mathcal{F}^{-1}\{\tilde{\mathcal{D}}_{z-u}\{\tilde{S}(\cdot,u)\}\}(t)=\mathcal{D}_{z-u}\left\{S(\cdot,u)\right\}(t). \tag{A.13}$$

Using (A.13) together with (A.8), we have

$$\begin{aligned}
A_1(t,z)&=\mathcal{F}^{-1}\{\tilde{A}_1(\cdot,z)\}(t)\\
&=\mathcal{F}^{-1}\left\{j\int_0^z \mathrm{e}^{-\alpha u}\mathrm{e}^{\frac{j\beta_2}{2}(\cdot)^2(z-u)}\tilde{S}(\cdot,u)\mathrm{d}u\right\}(t)\\
&=j\int_0^z \mathrm{e}^{-\alpha u}\mathcal{F}^{-1}\left\{\mathrm{e}^{\frac{j\beta_2}{2}(\cdot)^2(z-u)}\tilde{S}(\cdot,u)\right\}(t)\mathrm{d}u\\
&=j\int_0^z \mathrm{e}^{-\alpha u}\mathcal{F}^{-1}\left\{\tilde{\mathcal{D}}_{z-u}\{\tilde{S}(\cdot,u)\}\right\}(t)\mathrm{d}u\\
&=j\int_0^z \mathrm{e}^{-\alpha u}\mathcal{D}_{z-u}\left\{|A_0(\cdot,u)|^2A_0(\cdot,u)\right\}(t)\mathrm{d}u,
\end{aligned} \tag{A.14}$$

where in the last step we used (A.5).

□

A.2 Proof of Theorem 2 from Paper B and Sec. 3.4.4

Proof. To obtain A_0 and A_1 in (6.20) and (6.21), we substitute (6.18) in (6.3), resulting in

$$\begin{aligned}\sum_{k=0}^{\infty}\beta_2^k\frac{\partial A_k(t,z)}{\partial z}+\frac{j\beta_2}{2}\sum_{k=0}^{\infty}\beta_2^k\frac{\partial^2 A_k(t,z)}{\partial t^2}=\\ j\gamma\mathrm{e}^{-\alpha z}\sum_{m=0}^{\infty}\sum_{n=0}^{\infty}\sum_{p=0}^{\infty}\beta_2^{m+n+p}A_m(t,z)A_n^*(t,z)A_p(t,z).\end{aligned}\tag{A.15}$$

We now follow a procedure analogous to that in Sec. A.1 of the Appendix. First, we equate the terms that depend on the 0-th power of β_2. This gives

$$\frac{\partial A_0(t,z)}{\partial z}=j\gamma\mathrm{e}^{-\alpha z}|A_0(t,z)|^2A_0(t,z),\tag{A.16}$$

which has the same solution as the NLPN model in (6.12). The solution of (A.16) is (6.20), with G given by (6.13) and using the input field as initial condition, i.e., $A_0(t,0)=A(t,0)$.

The next step is to obtain A_1 by equating the terms that depend on β_2^1. This gives

$$\begin{aligned}\frac{\partial A_1(t,z)}{\partial z}+\frac{j}{2}\frac{\partial^2 A_0(t,z)}{\partial t^2}=\\ j\gamma\mathrm{e}^{-\alpha z}(2|A_0(t,z)|^2A_1(t,z)+A_1^*(t,z)A_0^2(t,z)).\end{aligned}\tag{A.17}$$

We now claim that (A.17) with the boundary condition $A_1(t,0)=0$ is solved by

$$A_1(t,z)=B(t,z)\mathrm{e}^{j\gamma|A(t,0)|^2G(z)},\tag{A.18}$$

where

$$\begin{aligned}B(t,z)=&-\int_0^z F(t,u)\mathrm{d}u\\ &-2j\gamma A(t,0)\Re\left\{A^*(t,0)\int_0^z(G(z)-G(u))F(t,u)\mathrm{d}u\right\},\end{aligned}\tag{A.19}$$

$$F(t,z)=\frac{j}{2}\frac{\partial^2 A_0(t,z)}{\partial t^2}\mathrm{e}^{-j\gamma|A(t,0)|^2G(z)}.\tag{A.20}$$

To prove that (A.18)–(A.20) solve (A.17), let

$$L(t,z)=\mathrm{e}^{j\gamma|A(t,0)|^2G(z)}.\tag{A.21}$$

Then, we can rewrite the first term in (A.17) using (A.18), (A.21) and (A.19) as

$$\begin{aligned} T_1 = \frac{\partial A_1(t,z)}{\partial z} &= B(t,z)\frac{\partial L(t,z)}{\partial z} + L(t,z)\frac{\partial B(t,z)}{\partial z} \\ &= j\gamma \mathrm{e}^{-\alpha z}|A(t,0)|^2 B(t,z)L(t,z) - L(t,z)F(t,z) \\ &- 2j\gamma \mathrm{e}^{-\alpha z} A(t,0)L(t,z)\Re\left\{A^*(t,0)\int_0^z F(t,u)\mathrm{d}u\right\}. \end{aligned} \tag{A.22}$$

The second term in (A.17) follows from (A.20) and (A.21) as

$$T_2 = \frac{j}{2}\frac{\partial^2 A_0(t,z)}{\partial t^2} = L(t,z)F(t,z). \tag{A.23}$$

For the other two remaining terms, (6.21), (A.18), and (A.21) yield

$$\begin{aligned} T_3 &= 2j\gamma|A_0(t,z)|^2 A_1(t,z)\mathrm{e}^{-\alpha z} \\ &= 2j\gamma|A(t,0)|^2 B(t,z)L(t,z)\mathrm{e}^{-\alpha z}, \end{aligned} \tag{A.24}$$

$$\begin{aligned} T_4 &= j\gamma A_0^2(t,z)A_1^*(t,z)\mathrm{e}^{-\alpha z} \\ &= j\gamma A^2(t,0)L(t,z)B^*(t,z)\mathrm{e}^{-\alpha z}. \end{aligned} \tag{A.25}$$

Now, combining the four terms to form (A.17), we obtain

$$\begin{aligned} &-T_1 - T_2 + T_3 + T_4 \\ &= j\gamma \mathrm{e}^{-\alpha z}|A(t,0)|^2 B(t,z)L(t,z) \\ &\quad + 2j\gamma \mathrm{e}^{-\alpha z}A(t,0)L(t,z)\Re\left\{A^*(t,0)\int_0^z F(t,u)\mathrm{d}u\right\} \\ &\quad + j\gamma A^2(t,0)L(t,z)B^*(t,z)\mathrm{e}^{-\alpha z} \\ &= j\gamma \mathrm{e}^{-\alpha z}L(t,z)A(t,0)\Bigg[2\Re\left\{A^*(t,0)\int_0^z F(t,u)\mathrm{d}u\right\} \\ &\quad + A^*(t,0)B(t,z) + A(t,0)B^*(t,z)\Bigg] \\ &= j\gamma \mathrm{e}^{-\alpha z}L(t,z)A(t,0) \\ &\quad \cdot \left[2\Re\left\{A^*(t,0)\left(\int_0^z F(t,u)\mathrm{d}u + B(t,z)\right)\right\}\right] \\ &= 0, \end{aligned} \tag{A.26}$$

where the last equation comes from the fact that $A^*(t,0)(\int_0^z F(t,u)\mathrm{d}u + B(t,z))$ is purely imaginary, which follows from using the definition of B in (A.19). This shows that (A.18)–(A.21) are a solution of (A.17).

Now, we will show that the integrals in (A.19) can be evaluated analytically. By substituting A_0 from (6.20) in the expression for F in (A.20), we obtain

$$\begin{aligned}F(t,z) = {} & \frac{j}{2}\frac{\partial^2 A(t,0)}{\partial t^2} - G(z)\left[\frac{\gamma}{2}A(t,0)\frac{\partial^2|A(t,0)|^2}{\partial t^2}\right. \\ & \left. + \gamma\frac{\partial A(t,0)}{\partial t}\frac{\partial |A(t,0)|^2}{\partial t}\right] \\ & - G^2(z)\left[\frac{j\gamma^2}{2}A(t,0)\left(\frac{\partial|A(t,0)|^2}{\partial t}\right)^2\right] \\ = {} & M(t) - G(z)R(t) - G^2(z)P(t),\end{aligned} \tag{A.27}$$

where M, R and P only depend on $A(\cdot,0)$ and are respectively given by (6.24), (6.25), and (6.26). Now, by denoting

$$G_1(z) = \int_0^z G(u)\mathrm{d}u = \frac{\alpha z + \mathrm{e}^{-\alpha z} - 1}{\alpha^2}, \tag{A.28}$$

$$G_2(z) = \int_0^z G^2(u)\mathrm{d}u = \frac{2\alpha z + 4\mathrm{e}^{-\alpha z} - \mathrm{e}^{-2\alpha z} - 3}{2\alpha^3}, \tag{A.29}$$

$$\begin{aligned}G_3(z) &= \int_0^z G^3(u)\mathrm{d}u \\ &= \frac{6\alpha z + 18\mathrm{e}^{-\alpha z} - 9\mathrm{e}^{-2\alpha z} + 2\mathrm{e}^{-3\alpha z} - 11}{6\alpha^4},\end{aligned} \tag{A.30}$$

the function B in (A.19) can be written as

$$\begin{aligned}B(t,z) = {} & -M(t)z + G_1(z)R(t) + G_2(z)P(t) \\ & - 2j\gamma A(t,0)\Re\{A^*(t,0)V(t,z)\},\end{aligned} \tag{A.31}$$

$$\begin{aligned}V(t,z) = {} & G(z)\left[M(t)z - G_1(z)R(t) - G_2(z)P(t)\right] \\ & - G_1(z)M(t) + G_2(z)R(t) + G_3(z)P(t),\end{aligned} \tag{A.32}$$

which completes the proof.

□

A.3 Proof of Theorem 3 from Paper B

Proof. For $\alpha = 0$, the effective length G in (6.13) degenerates to

$$\lim_{\alpha\to 0} G(z) = z \tag{A.33}$$

and similarly G_1, G_2, and G_3 are given by

$$G_1(z) = \frac{z^2}{2}, \quad G_2(z) = \frac{z^3}{3}, \quad G_3(z) = \frac{z^4}{4}. \tag{A.34}$$

Therefore, $A_0(t, z)$ in (6.20) and $A_1(t, z)$ in (6.21) are given by

$$A_0(t, z) = A(t, 0)\mathrm{e}^{j\gamma|A(t,0)|^2 z} \tag{A.35}$$

$$A_1(t, z) = B(t, z)\mathrm{e}^{j\gamma|A(t,0)|^2 z}. \tag{A.36}$$

The proof is completed by using (A.33) and (A.34) in (6.21) and (6.22), which yields (6.32).

□

References

[1] G. Agrawal, *Nonlinear Fiber Optics*, 5th ed., ser. Optics and Photonics. Boston: Academic Press, 2013.

[2] A. Sheikh, C. Fougstedt, A. Graell i Amat, P. Johannisson, P. Larsson-Edefors, and M. Karlsson, "Dispersion compensation FIR filter with improved robustness to coefficient quantization errors," *Journal of Lightwave Technology*, vol. 34, no. 22, pp. 5110–5117, Nov. 2016.

[3] D. Rafique, M. Mussolin, M. Forzati, J. Mårtensson, M. N. Chugtai, and A. D. Ellis, "Compensation of intra-channel nonlinear fibre impairments using simplified digital back-propagation algorithm." *Opt. Express*, vol. 19, no. 10, pp. 9453–9460, Apr. 2011.

[4] A. Napoli, Z. Maalej, V. A. J. M. Sleiffer, M. Kuschnerov, D. Rafique, E. Timmers, B. Spinnler, T. Rahman, L. D. Coelho, and N. Hanik, "Reduced complexity digital back-propagation methods for optical communication systems," *Journal of Lightwave Technology*, vol. 32, no. 7, pp. 1351–1362, Apr. 2014.

[5] W. Yan, Z. Tao, L. Dou, L. Li, S. Oda, T. Tanimura, T. Hoshida, and J. C. Rasmussen, "Low complexity digital perturbation back-propagation," in *European Conference and Exhibition on Optical Communication (ECOC)*, Sep. 2011.

[6] A. Vannucci, P. Serena, and A. Bononi, "The RP method: a new tool for the iterative solution of the nonlinear Schödinger equation," *Journal of Lightwave Technology*, vol. 20, no. 7, pp. 1102–1112, July 2002.

[7] E. Forestieri and M. Secondini, "Solving the nonlinear Schrödinger equation," in *Optical Communication Theory and Techniques*, 1st ed., E. Forestieri, Ed. Boston: Springer US, 2005, pp. 3–11.

[8] C. Häger and H. D. Pfister, "Nonlinear interference mitigation via deep neural networks," in *Proc. Optical Fiber Communication Conf. (OFC)*, San Diego, CA, Mar. 2018.

[9] R. M. Bütler, C. Häger, H. D. Pfister, G. Liga, and A. Alvarado, "Model-based machine learning for joint digital backpropagation and pmd compensation," *J. Lightwave Technol.*, vol. 39, no. 4, pp. 949–959, Oct. 2021.

[10] B. I. Bitachon, A. Ghazisaeidi, M. Eppenberger, B. Baeuerle, M. Ayata, and J. Leuthold, "Deep learning based digital backpropagation demonstrating SNR gain at low complexity in a 1200 km transmission link," *Opt. Express*, vol. 28, no. 20, pp. 29 318–29 334, Sep. 2020.

[11] E. Sillekens, W. Yi, D. Semrau, A. Ottino, B. Karanov, D. Lavery, L. Galdino, P. Bayvel, R. I. Killey, S. Zhou, K. Law, and J. Chen, "Time-domain learned digital back-propagation," in *IEEE Workshop on Signal Processing Systems (SiPS)*, Coimbra, Portugal, Sep. 2020.

[12] B. Chen, C. Okonkwo, H. Hafermann, and A. Alvarado, "Eight-dimensional polarization-ring-switching modulation formats," *IEEE Photonics Technology Letters*, vol. 31, no. 21, pp. 1717–1720, Sep. 2019.

[13] R. T. Jones, M. P. Yankov, and D. Zibar, "End-to-end learning for GMI optimized geometric constellation shape," in *45th European Conference on Optical Communication (ECOC)*, Dublin, Ireland, Sep. 2019.

[14] A. Amari, L. Lampe, S. K. O. Soman, Y. C. Gültekin, and A. Alvarado, "Comparison of short block-length sphere shaping and nonlinearity compensation in WDM systems," *IEEE Photonics Technology Letters*, vol. 32, no. 22, pp. 1435–1438, Oct. 2020.

[15] V. Oliari, E. Agrell, and A. Alvarado, "Regular perturbation for the weak-dispersion regime," in *21st International Conference on Transparent Optical Networks (ICTON)*, Angers, France, July 2019.

[16] V. Oliari, E. Agrell, and A. Alvarado, "Regular perturbation on the group-velocity dispersion parameter for nonlinear fibre-optical communications," *Nature Communications*, vol. 11, no. 933, pp. 1–11, Feb. 2020.

[17] V. Oliari, E. Agrell, and A. Alvarado, "Logarithmic perturbation models in the weak-dispersion regime with applications to passive optical networks," in *Proc. European Conf. Optical Communication (ECOC)*, Brussels, Belgium, Dec. 2020.

[18] V. Oliari, E. Agrell, G. Liga, and A. Alvarado, "Frequency logarithmic perturbation on the group-velocity dispersion parameter with applications to passive optical networks," *J. Lightwave Technol.*, vol. 39, no. 16, pp. 5287–5299, Aug. 2021.

[19] V. Oliari, S. Goossens, C. Häger, G. Liga, R. M. Bütler, M. van den Hout, S. van der Heide, H. D. Pfister, C. Okonkwo, and A. Alvarado, "Revisiting efficient multi-step nonlinearity compensation with machine learning: an experimental demonstration," *J. Lightwave Technol.*, vol. 38, no. 12, pp. 3114–3124, May 2020.

[20] V. Oliari, B. Karanov, S. Goossens, G. Liga, O. Vassilieva, I. Kim, P. Palacharla, C. Okonkwo, and A. Alvarado, "High-cardinality hybrid shaping for 4D modulation formats in optical communications optimized via end-to-end learning," *arXiv:2112.10471*, Dec. 2021.

[21] B. Karanov, V. Oliari, M. Chagnon, G. Liga, A. Alvarado, V. Aref, D. Lavery, P. Bayvel, and L. Schmalen, "End-to-end learning in optical fiber communications: experimental demonstration and future trends," in *Proc. European Conf. Optical Communications (ECOC)*, Brussels, Belgium, Dec. 2020.

[22] "World's first remote operation using 5G surgery," Feb. 2019 (accessed on October 10, 2021). [Online]. Available: https://www.huawei.com/en/technology-insights/industry-insights/outlook/mobile-broadband/wireless-for-sustainability/cases/worlds-first-remote-operation-using-5g-surgery

[23] D. Swinhoe, "What is a submarine cable? subsea fiber explained," Aug. 2021 (accessed on October 10, 2021). [Online]. Available: https://www.datacenterdynamics.com/en/analysis/what-is-a-submarine-cable-subsea-fiber-explained/

[24] A. D. Ellis, N. M. Suibhne, D. Saad, and D. N. Payne, "Communication networks beyond the capacity crunch," *Philosophical Transactions of the Royal Society A: Mathematical, Physical and Engineering Sciences*, vol. 374, Mar. 2016.

[25] E. Agrell, A. Alvarado, and F. R. Kschischang, "Implications of information theory in optical fibre communications," *Philosophical Transactions of the Royal Society A: Mathematical, Physical and Engineering Sciences*, vol. 374, Mar. 2016.

[26] D. Semrau, R. I. Killey, and P. Bayvel, "A closed-form approximation of the Gaussian noise model in the presence of inter-channel stimulated raman scattering," *Journal of Lightwave Technology*, vol. 37, no. 9, pp. 1924–1936, May 2019.

[27] A. Ghazisaeidi, "A theory of nonlinear interactions between signal and amplified spontaneous emission noise in coherent wavelength division multiplexed systems," *Journal of Lightwave Technology*, vol. 35, no. 23, pp. 5150–5175, Dec. 2017.

[28] E. Ip and J. M. Kahn, "Compensation of dispersion and nonlinear impairments using digital backpropagation," *Journal of Lightwave Technology*, vol. 26, no. 20, pp. 3416–3425, Oct. 2008.

[29] M. Secondini, S. Rommel, F. Fresi, E. Forestieri, G. Meloni, and L. Poti, "Coherent 100G nonlinear compensation with single-step digital backpropagation," in *International Conference on Optical Network Design and Modeling (ONDM)*, Pisa, Italy, May 2015, pp. 63–67.

[30] E. Sillekens, W. Yi, D. Semrau, A. Ottino, B. Karanov, S. Zhou, K. Law, J. Chen, D. Lavery, L. Galdino, P. Bayvel, and R. I. Killey, "Experimental demonstration of learned time-domain digital back-propagation," *arXiv:1912.12197*, Dec. 2019.

[31] B. Chen, A. Alvarado, S. van der Heide, M. van den Hout, H. Hafermann, and C. Okonkwo, "Analysis and experimental demonstration of orthant-symmetric four-dimensional 7 bit/4d-sym modulation for optical fiber communication," *Journal of Lightwave Technology*, vol. 39, no. 9, pp. 2737–2753, May 2021.

[32] R.-J. Essiambre, R. Ryf, M. Kodialam, B. Chen, M. Mazur, J. I. Bonetti, R. Veronese, H. Huang, A. Gupta, F. A. Aoudia, E. C. Burrows, D. F. Grosz, L. Palmieri, M. Sellathurai, X. Chen, N. K. Fontaine, and H. Chen, "Increased reach of long-haul transmission using a constant-power 4D format designed using neural networks," in *European Conference on Optical Communications (ECOC)*, Brussels, Belgium, Dec. 2020.

[33] E. Sillekens, D. Semrau, G. Liga, N. A. Shevchenko, Z. Li, A. Alvarado, P. Bayvel, R. I. Killey, and D. Lavery, "A simple nonlinearity-tailored probabilistic shaping distribution for square QAM," in *Optical Fiber Communications Conference and Exposition (OFC)*, San Diego, CA, Mar. 2018.

[34] T. Uhlemann, S. Cammerer, A. Span, S. Doerner, and S. ten Brink, "Deep-learning autoencoder for coherent and nonlinear optical communication," in *Photonic Networks; 21th ITG-Symposium*, Nov. 2020.

[35] A. Alvarado, T. Fehenberger, B. Chen, and F. M. J. Willems, "Achievable information rates for fiber optics: applications and computations," *J. Lightwave Technol.*, vol. 36, no. 2, pp. 424–439, Jan. 2018.

[36] M. Stark, F. Ait Aoudia, and J. Hoydis, "Joint learning of geometric and probabilistic constellation shaping," in *IEEE Globecom Workshops*, Waikoloa, USA, Dec. 2019.

[37] D. McClatchie, "Attenuation of standard coaxial cable," Dec. 2018 (accessed on June 24, 2021). [Online]. Available: https://www.fmsystems-inc.com/attenuation-standard-coaxial-cable/.

[38] P. K. A. Wai, C. R. Menyuk, and H. H. Chen, "Stability of solitons in randomly varying birefringent fibers," *Opt. Lett.*, vol. 16, no. 16, pp. 1231–1233, Aug. 1991.

[39] G. Bosco, A. Carena, V. Curri, R. Gaudino, P. Poggiolini, and S. Benedetto, "Suppression of spurious tones induced by the split-step method in fiber systems simulation," *IEEE Photonics Technology Letters*, vol. 12, no. 5, pp. 489–491, May 2000.

[40] P. Poggiolini, G. Bosco, A. Carena, V. Curri, Y. Jiang, and F. Forghieri, "The GN-model of fiber non-linear propagation and its applications," *Journal of Lightwave Technology*, vol. 32, no. 4, pp. 694–721, Dec. 2014.

[41] A. Carena, G. Bosco, V. Curri, Y. Jiang, P. Poggiolini, and F. Forghieri, "EGN model of non-linear fiber propagation," *Optics Express*, vol. 22, no. 13, p. 16335, June 2014.

[42] K. Hornik, M. Stinchcombe, and H. White, "Multilayer feedforward networks are universal approximators," *Neural Networks*, vol. 2, no. 5, pp. 359–366, Mar. 1989.

[43] A. Katharopoulos and F. Fleuret, "Not all samples are created equal: deep learning with importance sampling," in *Thirty-eighth International Conference on Machine Learning (ICML)*, Stockholm, Sweden, July 2018.

[44] I. Goodfellow, Y. Bengio, and A. Courville, *Deep Learning*. MIT Press, 2016, http://www.deeplearningbook.org.

[45] S. Sharma, "Activation functions in neural networks," Sep. 2017 (accessed on October 12, 2021). [Online]. Available: https://towardsdatascience.com/activation-functions-neural-networks-1cbd9f8d91d6.

[46] I. Goodfellow, D. Warde-Farley, M. Mirza, A. Courville, and Y. Bengio, "Maxout networks," in *International Conference on Machine Learning (ICML)*, Atlanta, USA, June 2013.

[47] K. Mahendru, "A detailed guide to 7 loss functions for machine learning algorithms with Python code," Aug. 2019 (accessed on October 13, 2021). [Online]. Available: https://www.analyticsvidhya.com/blog/2019/08/detailed-guide-7-loss-functions-machine-learning-python-code/.

[48] K. Katanforoosh and D. Kunin, "Initializing neural networks," 2019 (accessed on October 13, 2021). [Online]. Available: https://www.deeplearning.ai/ai-notes/initialization/.

[49] D. P. Kingma and J. Ba, “Adam: a method for stochastic optimization,” in *Proc. Int. Conf. Learning Representations (ICLR)*, San Diego, CA, May 2015.

[50] H. Louchet, K. Kuzmin, and A. Richter, “Improved dsp algorithms for coherent 16-QAM transmission,” in *34th European Conference on Optical Communication*, Brussels, Sep. 2008.

[51] E. J. Gumbel, “Statistical theory of extreme values and some practical applications,” *The Journal of the Royal Aeronautical Society*, vol. 58, no. 527, p. 792–793, Nov. 1954.

[52] C. J. Maddison, D. Tarlow, and T. Minka, “A* sampling,” *Advances in Neural Information Processing Systems,*, p. 3086–3094, Dec. 2014.

[53] E. J. Gumbel, “The return period of flood flows,” *The Annals of Mathematical Statistics*, vol. 12, no. 2, pp. 163 – 190, June 1941.

[54] E. Jang, S. Gu, and B. Poole, “Categorical reparameterization with gumbel-softmax,” in *5th International Conference on Learning Representations*, Toulon, France, Apr. 2017.

[55] R.-J. Essiambre, G. Kramer, P. J. Winzer, G. J. Foschini, and B. Goebel, “Capacity limits of optical fiber networks,” *Journal of Lightwave Technology*, vol. 28, no. 4, pp. 662–701, Feb. 2010.

[56] H. Bulow, F. Buchali, and A. Klekamp, “Electronic dispersion compensation,” *Journal of Lightwave Technology*, vol. 26, no. 1, pp. 158–167, Feb. 2008.

[57] S. T. Le, V. Aref, and H. Buelow, “Nonlinear signal multiplexing for communication beyond the Kerr nonlinearity limit,” *Nature Photonics*, vol. 11, no. 11, p. 570–576, July 2017.

[58] O. V. Sinkin, R. Holzlohner, J. Zweck, and C. R. Menyuk, “Optimization of the split-step Fourier method in modeling optical-fiber communications systems,” *Journal of Lightwave Technology*, vol. 21, no. 1, pp. 61–68, Jan. 2003.

[59] R.-J. Essiambre and P. Winzer, “Fibre nonlinearities in electronically pre-distorted transmission,” in *2005 31st European Conference on Optical Communication, ECOC 2005*, vol. 2, Glasgow, Scotland, Sep. 2005, pp. 191–192, vol. 2.

[60] L. Beygi, E. Agrell, M. Karlsson, and P. Johannisson, “Signal statistics in fiber-optical channels with polarization multiplexing and self-phase modulation,” *J. Lightwave Technol.*, vol. 29, no. 16, pp. 2379–2386, Aug. 2011.

[61] J. K. Shaw, *Mathematical Principles of Optical Fiber Communications*. Philadelphia: Society for Industrial and Applied Mathematics, 2004.

[62] K. Keykhosravi, M. Tavana, E. Agrell, and G. Durisi, “Demodulation and detection schemes for a memoryless optical WDM channel,” *IEEE Transactions on Communications*, vol. 66, no. 7, pp. 2994–3005, July 2018.

[63] A. Amari, P. Ciblat, and Y. Jaouën, “Fifth-order Volterra series based nonlinear equalizer for long-haul high data rate optical fiber communications,” in *Asilomar Conference on Signals, Systems and Computers*, Pacific Grove, USA, Nov. 2014, pp. 1367–1371.

[64] X. Liu, A. R. Chraplyvy, P. J. Winzer, R. W. Tkach, and S. Chandrasekhar, “Phase-conjugated twin waves for communication beyond the Kerr nonlinearity limit,” *Nature Photonics*, vol. 7, no. 7, pp. 560–568, May 2013.

[65] E. Forestieri and G. Prati, “Novel optical line codes tolerant to fiber chromatic dispersion,” *Journal of Lightwave Technology*, vol. 19, no. 11, pp. 1675–1684, Nov. 2001.

[66] H. Ghozlan and G. Kramer, “Models and information rates for multiuser optical fiber channels with nonlinearity and dispersion,” *IEEE Transactions on Information Theory*, vol. 63, no. 10, pp. 6440–6456, Oct. 2017.

[67] K. S. Turitsyn, S. A. Derevyanko, I. V. Yurkevich, and S. K. Turitsyn, “Information capacity of optical fiber channels with zero average dispersion,” *Phys. Rev. Lett.*, vol. 91, pp. 203 901–1–203 901–4, Nov. 2003.

[68] K. Keykhosravi, G. Durisi, and E. Agrell, “A tighter upper bound on the capacity of the nondispersive optical fiber channel,” in *European Conference on Optical Communication (ECOC)*, Sep. 2017.

[69] E. E. Narimanov and P. Mitra, “The channel capacity of a fiber optics communication system: perturbation theory,” *Journal of Lightwave Technology*, vol. 20, no. 3, pp. 530–537, Mar. 2002.

[70] L. Xiang and X. P. Zhang, “The study of information capacity in multispan nonlinear optical fiber communication systems using a developed perturbation technique,” *Journal of Lightwave Technology*, vol. 29, no. 3, pp. 260–264, Feb. 2011.

[71] H. Ghozlan and G. Kramer, “Interference focusing for mitigating cross-phase modulation in a simplified optical fiber model,” in *IEEE International Symposium on Information Theory*, June 2010, pp. 2033–2037.

[72] K. Keykhosravi, G. Durisi, and E. Agrell, “Bounds on the per-sample capacity of zero-dispersion simplified fiber-optical channel models,” *arXiv:1708.03102v2*, Sep. 2018.

[73] K. V. Peddanarappagari and M. Brandt-Pearce, “Volterra series transfer function of single-mode fibers,” *Journal of Lightwave Technology*, vol. 15, no. 12, pp. 2232–2241, Dec. 1997.

[74] X. Chen, C. Antonelli, S. Chandrasekhar, G. Raybon, J. Sinsky, A. Mecozzi, M. Shtaif, and P. Winzer, “218-Gb/s single-wavelength, single-polarization, single-photodiode transmission over 125-km of standard single-mode fiber using Kramers-Kronig detection,” in *Optical Fiber Communications Conference and Exhibition (OFC)*, Los Angeles, USA, Mar. 2017.

[75] S. J. Savory, “Digital filters for coherent optical receivers,” *Opt. Express*, vol. 16, no. 2, pp. 804–817, Jan 2008.

[76] M. Vasilyev, “Raman-assisted transmission: toward ideal distributed amplification,” in *Optical Fiber Communications Conference (OFC)*, Atlanta, USA, Mar. 2003.

[77] L. Xue, L. Yi, P. Li, and W. Hu, “50-Gb/s TDM-PON based on 10G-class devices by optics-simplified DSP,” in *Optical Fiber Communications Conference and Exposition (OFC)*, San Diego, USA, Mar. 2018, pp. 1–3.

[78] J. Wang, Z. Jia, L. A. Campos, L. Cheng, C. Knittle, and G.-K. Chang, “Delta-sigma digitization and optical coherent transmission of DOCSIS 3.1 signals in hybrid fiber coax networks,” *Journal of Lightwave Technology*, vol. 36, no. 2, pp. 568–579, Nov. 2018.

[79] M. Secondini, E. Forestieri, and C. R. Menyuk, “A combined regular-logarithmic perturbation method for signal-noise interaction in amplified optical systems,” *Journal of Lightwave Technology*, vol. 27, no. 16, pp. 3358–3369, 2009.

[80] E. Ciaramella and E. Forestieri, “Analytical approximation of nonlinear distortions,” *IEEE Photonics Technology Letters*, vol. 17, no. 1, pp. 91–93, 2005.

[81] M. Secondini and E. Forestieri, “Analytical fiber-optic channel model in the presence of cross-phase modulation,” *IEEE Photonics Technol. Lett.*, vol. 24, no. 22, pp. 2016–2019, Sep. 2012.

[82] M. Secondini, E. Forestieri, and G. Prati, “Achievable information rate in nonlinear WDM fiber-optic systems with arbitrary modulation formats and dispersion maps,” *J. Lightwave Technol.*, vol. 31, no. 23, pp. 3839–3852, Nov. 2013.

[83] *10-Gigabit-capable passive optical networks (XG-PON): physical media dependent (PMD) layer specification*, ITU-T G.987.2, Feb. 2016.

[84] *PON transmission technologies above 10 Gb/s per wavelength*, ITU-T G.Sup64, Feb. 2018.

[85] D. Semrau, R. I. Killey, and P. Bayvel, “The gaussian noise model in the presence of inter-channel stimulated raman scattering,” *Journal of Lightwave Technology*, vol. 36, no. 14, pp. 3046–3055, July 2018.

[86] M. Secondini, E. Agrell, E. Forestieri, D. Marsella, and M. R. Camara, “Nonlinearity mitigation in WDM systems: models, strategies, and achievable rates,” *J. Lightwave Technol.*, vol. 37, no. 10, pp. 2270–2283, Feb. 2019.

[87] T. Koonen, “Fiber to the home/fiber to the premises: what, where, and when?” *Proceedings of the IEEE*, vol. 94, no. 5, pp. 911–934, May 2006.

[88] B. De Vos, F. Duthilleul, F. Fredricx, P. Vetter, P. Ossieur, J. Bauwelinck, X.-Z. Qiu, J. Vandewege, and J. Watte, “Demonstration of extended split APON,” in *Optical Fiber Communication Conference and Exhibit*, Mar. 2002, pp. 437–439.

[89] D. Piehler, “Implementing high [$>$ 2048] split ratios in any PON,” in *Optical Fiber Communication Conference and Exposition and the National Fiber Optic Engineers Conference*, Los Angeles, USA, Mar. 2011.

[90] D. Lavery, M. Paskov, R. Maher, B. C. Thomsen, S. J. Savory, and P. Bayvel, “Low complexity multichannel nonlinear predistortion for passive optical networks,” in *Advanced Photonics 2015*. Optical Society of America, Jun. 2015.

[91] D. Lavery, R. Maher, D. Millar, A. Alvarado, S. J. Savory, and P. Bayvel, “Why compensating fibre nonlinearity will never meet capacity demands,” *arXiv:1512.03426*, Dec. 2019.

[92] *10-Gigabit-capable passive optical networks (XG-PON): transmission convergence (TC) layer specification*, ITU-T G.987.3, 2014.

[93] I. Reed and G. Solomon, “Polynomial codes over certain finite fields,” *J. Soc. Indust. Appl. Math.*, vol. 8, no. 2, pp. 300–304, June 1960.

[94] L. Schmalen, A. J. de Lind van Wijngaarden, and S. Ten Brink, “Forward error correction in optical core and optical access networks,” *Bell Labs Technical Journal*, vol. 18, no. 3, pp. 39–66, Dec. 2013.

[95] B. Powell and K. Droskiewicz, “Latency & complexity for various 25/50/100G EPON FEC code proposals,” Sep. 2017 (accessed on August 20, 2020). [Online]. Available: https://www.ieee802.org/3/ca/public/meeting_archive/2017/09/powell_3ca_1a_0917.pdf

[96] D. van Veen, V. Houtsma, A. de Lind van Wijngaarden, B. Powell, and E. Harstead, “FEC code for 25/50/100G EPON,” Mar. 2017 (accessed on August 20, 2020). [Online]. Available: https://www.ieee802.org/3/ca/email/pdfUGjlG0uq7U.pdf

[97] A. Teixeira, D. Lavery, E. Ciaramella, L. Schmalen, N. Iiyama, R. M. Ferreira, and S. Randel, “DSP enabled optical detection techniques for PON,” *J. Lightwave Technol.*, vol. 38, no. 3, pp. 684–695, Feb. 2020.

[98] B. P. Smith, A. Farhood, A. Hunt, F. R. Kschischang, and J. Lodge, “Staircase codes: FEC for 100 Gb/s OTN,” *J. Lightwave Technol.*, vol. 30, no. 1, pp. 110–117, Jan. 2012.

[99] *Forward error correction for high bit-rate DWDM submarine systems*, ITU-T G.975.1, 2004.

[100] T. Fehenberger, A. Alvarado, P. Bayvel, and N. Hanik, “On achievable rates for long-haul fiber-optic communications,” *Opt. Express*, vol. 23, no. 7, pp. 9183–9191, Apr. 2015.

[101] K. Atkinson, *An introduction to numerical analysis*, 2nd ed. New York: John Wiley & Sons, 1989.

[102] M. Kamermans, “Gaussian quadrature weights and abscissae,” June 2011 (accessed on June 23, 2021). [Online]. Available: https://pomax.github.io/bezierinfo/legendre-gauss.html

[103] V. Oliari. (2021) Frequency logarithmic perturbation on β_2. [Online]. Available: https://github.com/TUe-ICTLab/Frequency-logarithmic-perturbation-on-beta2

[104] X. Li, X. Chen, G. Goldfarb, E. Mateo, I. Kim, F. Yaman, and G. Li, “Electronic post-compensation of WDM transmission impairments using coherent detection and digital signal processing,” *Opt. Express*, vol. 16, no. 2, pp. 880–888, Jan. 2008.

[105] E. Mateo, L. Zhu, and G. Li, “Impact of XPM and FWM on the digital implementation of impairment compensation for WDM transmission using backward propagation,” *Opt. Express*, vol. 16, no. 20, pp. 16 124–16 137, Sep. 2008.

[106] D. S. Millar, S. Makovejs, C. Behrens, S. Hellerbrand, R. I. Killey, P. Bayvel, and S. J. Savory, “Mitigation of fiber nonlinearity using a digital coherent receiver,” *IEEE J. Sel. Topics. Quantum Electron.*, vol. 16, no. 5, pp. 1217–1226, Sep. 2010.

[107] Y. Gao, F. Zhang, L. Dou, Z. Chen, and A. Xu, “Intra-channel nonlinearities mitigation in pseudo-linear coherent QPSK transmission systems via nonlinear electrical equalizer,” *Opt. Communications*, vol. 282, no. 12, pp. 2421–2425, June 2009.

[108] L. Liu, L. Li, Y. Huang, K. Cui, Q. Xiong, F. N. Hauske, C. Xie, and Y. Cai, "Intrachannel nonlinearity compensation by inverse Volterra series transfer function," *Journal of Lightwave Technology*, vol. 30, no. 3, pp. 310–316, Dec. 2012.

[109] F. P. Guiomar, J. D. Reis, A. L. Teixeira, and A. N. Pinto, "Mitigation of intra-channel nonlinearities using a frequency-domain Volterra series equalizer," *Opt. Express*, vol. 20, no. 2, pp. 1360–1369, Jan. 2012.

[110] Z. Tao, L. Dou, W. Yan, L. Li, T. Hoshida, and J. C. Rasmussen, "Multiplier-free intrachannel nonlinearity compensating algorithm operating at symbol rate," *Journal of Lightwave Technology*, vol. 29, no. 17, pp. 2570–2576, Sep. 2011.

[111] X. Liang and S. Kumar, "Multi-stage perturbation theory for compensating intra-channel nonlinear impairments in fiber-optic links," *Optics Express*, vol. 22, no. 24, p. 29733, Nov. 2014.

[112] H. Nakashima, T. Oyama, C. Ohshima, Y. Akiyama, Z. Tao, and T. Hoshida, "Digital nonlinear compensation technologies in coherent optical communication systems," in *Proc. Optical Fiber Communication Conf. (OFC)*, Los Angeles, CA, 2017.

[113] J. C. Cartledge, F. P. Guiomar, F. R. Kschischang, G. Liga, and M. P. Yankov, "Digital signal processing for fiber nonlinearities," *Opt. Express*, vol. 25, no. 3, pp. 1916–1936, Feb. 2017.

[114] L. B. Du and A. J. Lowery, "Improved single channel backpropagation for intra-channel fiber nonlinearity compensation in long-haul optical communication systems." *Opt. Express*, vol. 18, no. 16, pp. 17 075–17 088, July 2010.

[115] A. M. Jarajreh, E. Giacoumidis, I. Aldaya, S. T. Le, A. Tsokanos, Z. Ghassemlooy, and N. J. Doran, "Artificial neural network nonlinear equalizer for coherent optical OFDM," *IEEE Photon. Technol. Lett.*, vol. 27, no. 4, pp. 387–390, Feb. 2015.

[116] E. Giacoumidis, S. T. Le, M. Ghanbarisabagh, M. McCarthy, I. Aldaya, S. Mhatli, M. A. Jarajreh, P. A. Haigh, N. J. Doran, A. D. Ellis, and B. J. Eggleton, "Fiber nonlinearity-induced penalty reduction in CO-OFDM by ANN-based nonlinear equalization," *Opt. Lett.*, vol. 40, no. 21, pp. 5113–5116, Nov. 2015.

[117] M. Secondini, S. Rommel, G. Meloni, F. Fresi, E. Forestieri, and L. Poti, "Single-step digital backpropagation for nonlinearity mitigation," *Photon. Netw. Commun.*, vol. 31, no. 3, pp. 493–502, June 2016.

[118] C. Fougstedt, M. Mazur, L. Svensson, H. Eliasson, M. Karlsson, and P. Larsson-Edefors, "Time-domain digital back propagation: algorithm and finite-precision implementation aspects," in *Proc. Optical Fiber Communication Conf. (OFC)*, Los Angeles, CA, Mar. 2017.

[119] H. W. Lin, M. Tegmark, and D. Rolnick, "Why does deep and cheap learning work so well?" *J. Stat. Phys.*, vol. 168, no. 6, pp. 1223–1247, Sep. 2017.

[120] C. Häger and H. D. Pfister, "Deep learning of the nonlinear Schrödinger equation in fiber-optic communications," in *Proc. IEEE Int. Symp. Information Theory (ISIT)*, Vail, CO, June 2018.

[121] C. Fougstedt, C. Häger, L. Svensson, H. D. Pfister, and P. Larsson-Edefors, "ASIC implementation of time-domain digital backpropagation with deep-learned chromatic dispersion filters," in *Proc. European Conf. Optical Communication (ECOC)*, Rome, Italy, Nov. 2018.

[122] Y. Lecun, J. S. Denker, and S. A. Solla, "Optimal Brain Damage," in *Proc. Advances in Neural Information Processing Systems (NIPS)*, Denver, CO, Nov. 1989.

[123] S. Han, H. Mao, and W. J. Dally, "Deep compression: compressing deep neural networks with pruning, trained quantization and Huffman coding," in *Proc. Int. Conf. Learning Representations (ICLR)*, San Juan, Puerto Rico, May 2016.

[124] C. Häger, H. D. Pfister, R. M. Bütler, G. Liga, and A. Alvarado, "Revisiting multi-step nonlinearity compensation with machine learning," in *Proc. European Conf. Optical Communication (ECOC)*, Dublin, Ireland, Sep. 2019.

[125] B. I. Bitachon, A. Ghazisaeidi, B. Baeuerle, M. Eppenberger, and J. Leuthold, "Deep learning based digital back propagation with polarization state rotation & phase noise invariance," in *Proc. Optical Fiber Communication Conf. (OFC)*, San Diego, CA, Mar. 2020.

[126] D. Marcuse, C. R. Menyuk, and P. K. A. Wai, “Application of the Manakov-PMD equation to studies of signal propagation in optical fibers with randomly varying birefringence,” *Journal of Lightwave Technology*, vol. 15, no. 9, pp. 1735–1745, Sep. 1997.

[127] E. Ip, “Nonlinear compensation using backpropagation for polarization-multiplexed transmission,” *Journal of Lightwave Technology*, vol. 28, no. 6, pp. 939–951, Mar. 2010.

[128] R. Gilmore, “Baker-Campbell-Hausdorff formulas,” *J. Mathematical Physics*, vol. 15, no. 12, pp. 2090–2092, Dec. 1974.

[129] C. B. Czegledi, G. Liga, D. Lavery, M. Karlsson, E. Agrell, S. J. Savory, and P. Bayvel, “Digital backpropagation accounting for polarization-mode dispersion,” *Opt. Express*, vol. 25, no. 3, pp. 1903–1915, Feb. 2017.

[130] G. Liga, C. Czegledi, and P. Bayvel, “A PMD-adaptive DBP receiver based on SNR optimization,” in *Proc. Optical Fiber Communication Conf. (OFC)*, San Diego, CA, Mar. 2018.

[131] S. J. Savory, “Digital filters for coherent optical receivers,” *Opt. Express*, vol. 16, no. 2, pp. 804–817, Jan. 2008.

[132] L. Zhu, X. Li, E. Mateo, and G. Li, “Complementary FIR filter pair for distributed impairment compensation of WDM fiber transmission,” *IEEE Photon. Technol. Lett.*, vol. 21, no. 5, pp. 292–294, Mar. 2009.

[133] G. Goldfarb and G. Li, “Efficient backward-propagation using wavelet- based filtering for fiber backward-propagation,” *Opt. Express*, vol. 17, no. 11, pp. 814–816, May 2009.

[134] M. Lian, C. Häger, and H. D. Pfister, “What can machine learning teach us about communications?” in *Proc. IEEE Information Theory Workshop (ITW)*, Guangzhou, China, 2018.

[135] M. E. O’Neill, “Pcg: A family of simple fast space-efficient statistically good algorithms for random number generation,” Harvey Mudd College, Claremont, CA, Tech. Rep. HMC-CS-2014-0905, Sep. 2014.

[136] C.-Y. Lin, A. Napoli, B. Spinnler, V. Sleiffer, D. Rafique, M. Kuschnerov, M. Bohn, and B. Schmauss, “Adaptive digital back-propagation for optical communication systems,” in *Proc. Optical Fiber Communication Conf. (OFC)*, San Franscisco, CA, 2014.

[137] C. Lin, S. Chandrasekhar, and P. J. Winzer, “Experimental study of the limits of digital nonlinearity compensation in DWDM systems,” in *Proc. Optical Fiber Communication Conf. (OFC)*, Los Angeles, CA, 2015.

[138] L. Galdino, D. Semrau, D. Lavery, G. Saavedra, C. B. Czegledi, E. Agrell, R. I. Killey, and P. Bayvel, “On the limits of digital back-propagation in the presence of transceiver noise,” *Opt. Express*, vol. 25, no. 4, pp. 4564–4578, Feb. 2017.

[139] C. Fougstedt, L. Svensson, M. Mazur, M. Karlsson, and P. Larsson-Edefors, “ASIC implementation of time-domain digital back propagation for coherent receivers,” *IEEE Photon. Technol. Lett.*, vol. 30, no. 13, pp. 1179–1182, July 2018.

[140] C. S. Martins, L. Bertignono, A. Nespola, A. Carena, F. P. Guiomar, and A. N. Pinto, “Efficient time-domain DBP using random step-size and multi-band quantization,” in *Proc. Optical Fiber Communication Conf. (OFC)*, San Diego, CA, 2018.

[141] M. G. Taylor, “Compact digital dispersion compensation algorithms,” in *Proc. Optical Fiber Communication Conf. (OFC)*, San Diego, CA, 2008.

[142] K.-P. Ho, “Subband equaliser for chromatic dispersion of optical fibre,” *Electronics Lett.*, vol. 45, no. 24, pp. 1224–1226, Nov. 2009.

[143] I. Slim, A. Mezghani, L. G. Baltar, J. Qi, F. N. Hauske, and J. A. Nossek, “Delayed single-tap frequency-domain chromatic-dispersion compensation,” *IEEE Photon. Technol. Lett.*, vol. 25, no. 2, pp. 167–170, Jan. 2013.

[144] M. Nazarathy and A. Tolmachev, “Subbanded DSP architectures based on underdecimated filter banks for coherent OFDM receivers: Overview and recent advances,” *IEEE Signal Processing Mag.*, vol. 31, no. 2, pp. 70–81, Mar. 2014.

[145] E. F. Mateo, F. Yaman, and G. Li, “Efficient compensation of inter-channel nonlinear effects via digital backward propagation in WDM optical transmission,” *Opt. Express*, vol. 18, no. 14, pp. 15 144–15 154, July 2010.

[146] E. Ip, N. Bai, and T. Wang, “Complexity versus performance tradeoff for fiber nonlinearity compensation using frequency-shaped, multi-subband backpropagation,” in *Proc. Optical Fiber Communication Conf. (OFC)*, Los Angeles, CA, 2011.

[147] T. Oyama, H. Nakashima, T. Hoshida, T. Tanimura, Y. Akiyama, Z. Tao, and J. C. Rasmussen, “Complexity reduction of perturbation-based nonlinear compensator by sub-band processing,” in *Proc. Optical Fiber Communication Conf. (OFC)*, Los Angeles, CA, 2015.

[148] C. Häger and H. D. Pfister, “Wideband time-domain digital backpropagation via subband processing and deep learning,” in *Proc. European Conf. Optical Communication (ECOC)*, Rome, Italy, 2018.

[149] J. Leibrich and W. Rosenkranz, “Efficient numerical simulation of multichannel WDM transmission systems limited by XPM,” *IEEE Photon. Technol. Lett.*, vol. 15, no. 3, pp. 395–397, Mar. 2003.

[150] K. Goroshko, H. Louchet, and A. Richter, “Overcoming performance limitations of digital back propagation due to polarization mode dispersion,” in *Proc. Int. Conf. Transparent Optical Networks (ICTON)*, Trento, Italy, 2016.

[151] D. E. Crivelli, M. R. Hueda, H. S. Carrer, M. Del Barco, R. R. López, P. Gianni, J. Finochietto, N. Swenson, P. Voois, and O. E. Agazzi, “Architecture of a single-chip 50 Gb/s DP-QPSK/BPSK transceiver with electronic dispersion compensation for coherent optical channels,” *IEEE Trans. Circuits Syst. I: Reg. Papers*, vol. 61, no. 4, pp. 1012–1025, Apr. 2014.

[152] C. Häger, H. D. Pfister, R. M. Bütler, G. Liga, and A. Alvarado, “Model-based machine learning for joint digital backpropagation and PMD compensation,” in *Invited paper at the Optical Fiber Communication Conf. (OFC)*, San Diego, CA, 2020.

[153] T. Sherborne, B. Banks, D. Semrau, R. I. Killey, P. Bayvel, and D. Lavery, “On the impact of fixed point hardware for optical fiber nonlinearity compensation algorithms,” *Journal of Lightwave Technology*, vol. 36, no. 20, pp. 5016–5022, Oct. 2018.

[154] T. O’Shea and J. Hoydis, “An introduction to deep learning for the physical layer,” *IEEE Transactions on Cognitive Communications and Networking*, vol. 3, no. 4, pp. 563–575, Dec. 2017.

[155] B. Karanov, M. Chagnon, F. Thouin, T. A. Eriksson, H. Bülow, D. Lavery, P. Bayvel, and L. Schmalen, “End-to-end deep learning of optical fiber communications,” *Journal of Lightwave Technology*, vol. 36, no. 20, pp. 4843–4855, Oct. 2018.

[156] K. Gümüş, A. Alvarado, B. Chen, C. Häger, and E. Agrell, “End-to-end learning of geometrical shaping maximizing generalized mutual information,” in *2020 Optical Fiber Communications Conference and Exhibition (OFC)*, Mar. 2020, pp. 1–3.

[157] V. Neskorniuk, A. Carnio, V. Bajaj, D. Marsella, S. K. Turitsyn, J. E. Prilepsky, and V. Aref, “End-to-end deep learning of long-haul coherent optical fiber communications via regular perturbation model,” in *2021 European Conference on Optical Communication (ECOC)*, Sep. 2021, pp. 1–4.

[158] R. Dar, M. Feder, A. Mecozzi, and M. Shtaif, “On shaping gain in the nonlinear fiber-optic channel,” in *2014 IEEE International Symposium on Information Theory*, July 2014, pp. 2794–2798.

[159] V. Aref and M. Chagnon, “End-to-end learning of joint geometric and probabilistic constellation shaping,” *arXiv:2112.05050v1*, Dec. 2021.

[160] E. Agrell, “Database of sphere packings,” 2014 (accessed on October 18, 2021). [Online]. Available: http://codes.se/packings

[161] A. Alvarado and E. Agrell, “Four-dimensional coded modulation with bit-wise decoders for future optical communications,” *Journal of Lightwave Technology*, vol. 33, no. 10, pp. 1993–2003, May 2015.

Acknowledgements

The beginning of my PhD journey started in Brazil, when my BSc. supervisor showed me an open position for a PhD in the Netherlands. I already had missed an opportunity to come to the Netherlands for an exchange program, so I thought this might be my chance. After applying for the position and an Skype interview, I was invited for a face-to-face interview in April. For the first time, I visited this amazing country. I confess that the temperatures could have been a bit higher and there could be less raining days, but that did not discouraged me. I was then accepted and started my PhD in September, 2017.

During all these years of PhD, I have met many people and visited many places, some of them I would never imagine visiting. Every experience–the bad and the good ones–contributed for my growth during this period. Of course, the people that have being part of my life, even before my PhD, were the most important factor that led me to where I am today. I would like to first thank my supervisor Alex for giving me this unique opportunity and for the guidance during my studies. When I look back at how I was when I started my PhD, I see how I have improved in both quality and organization in my research. This improvement would never be possible without his detailed feedback and support. I would also like to thank Erik for the collaboration in many of my papers during my PhD. His detailed feedback and contributions to my work were crucial. I would like to thank my BSc. supervisor Jair, who presented me this opportunity and also supported me to reach this position.

I would like to thank all my colleagues. With them, I had many interesting and insightful discussions on both technical and life subjects. Not only they became my friends, but also I was able to share with them many experiences, such as going to musical concerts, canoeing, going to the cinema, etc. I would also like to thank my friends and all the people who were part of my life here and made me feel at home. I arrived to the Netherlands without knowing anyone. Little by little, I have met people who helped me adapting to this new country. After a while, living here did not feel strange or odd, since I knew I had people to count on. As an example, in the beginning, every time I was coming back to the Netherlands from vacations in Brazil I had a feeling that I was again parting from home to a strange place. In the last

time I came back from vacations, that feeling changed. I finally felt like I was coming to my home in the Netherlands because the people I met here made me feel that way.

I would also like to thank my parents, Ana and Jason, whose support was essential for me. They were the ones responsible for my education, for sustaining and teaching me, such that I could success in my life. Since I was a child, I was already incentivized by them to study, specially math, and that made me take pleasure in solving problems and challenging myself to learn new things. I would also like to thank all my other relatives, which were also part of my life and shared experiences with me.

Vinícius Oliari Couto Dias
Eindhoven, December 2021

Biography

Vinícius Oliari Couto Dias was born on May 08, 1993, in Vila Velha, Brazil. He received his B.Sc. in Electrical Engineering and his M.Sc. in Mathematics from the Federal University of Espírito Santo (UFES), Brazil, in 2016 and 2017, respectively. During his Bachelor, he worked on optical communications in the UFES Telecommunications Laboratory (LabTel). On his Master's, he studied wavelets theory and collaborated with the Laboratory of Research and Development of Petroleum Analysis Methodology (LabPetro).

In September 2017, he started a Ph.D. in the Information and Communication Theory (ICT) Lab, Eindhoven University of Technology (TU/e), Netherlands, under the supervision of Alex Alvarado. His research focused on the derivation of novel analytical fiber models for the weak-dispersion highly-nonlinear regime. In addition, he also worked with machine learning techniques applied to receiver design and constellation shaping. This thesis include some of the main results of his Ph.D. research.